1986

Search for gluonic bound states in high energy proton-proton collisions

Larry Donald Isenhower
Iowa State University

Isenhower, Larry Donald

SEARCH FOR GLUONIC BOUND STATES IN HIGH ENERGY PROTON-PROTON COLLISIONS

Iowa State University PH.D. 1986

Search for gluonic bound states in high energy proton-proton collisions

by

Larry Donald Isenhower

A Dissertation Submitted to the
Graduate Faculty in Partial Fulfillment of the
Requirements for the Degree of
DOCTOR OF PHILOSOPHY

Department: Physics
Major: High Energy Physics

Approved:

Members of the Committee:

Signature was redacted for privacy.

In Charge of Major Work

Signature was redacted for privacy.

Signature was redacted for privacy.

For the Major Department

Signature was redacted for privacy.

For the Graduate College

Iowa State University
Ames, Iowa

1986

TABLE OF CONTENTS

ACKNOWLEDGMENTS

I would especially like to thank my wife, Cindy Kay Isenhower, for her support and encouragement while I worked on my Ph.D. at Iowa State University. She has endured many nights alone and done a marvelous job of taking care of our children without as much help as I wish I could have given. I would also like to thank my parents, John Davis Isenhower and Roberta Nell Isenhower for their early encouragement and stimulation that got me interested in science in the first place.

I would like to thank Dr. Alexander Firestone for his guidance and quick response during the preparation of this dissertation. Thanks also goes to Dr. Henry Bert Crawley for his many suggestions and hard work on helping to figure out all the many problems that had to be overcome in order to analyze the data presented here. I would also like to thank the other members of my committee, Dr. Bing-Lin Young, Dr. Dean Isaacson, Dr. John Clem, and Dr. Robert Shelton who graciously filled in during the absence of Dr. Clem for my final oral examination.

A special thanks goes to Dr. Jerry Lamsa, who has worked very hard on this experiment. The acceptance corrections used in this thesis are the result of a great deal of effort on his part, and I certainly would be a long ways from finishing my degree without his help.

I would also like to thank those people who have contributed to this experiment during the many phases it took to complete. In particular, I would like to thank the other Ames Laboratory collaborators who have helped me at various stages of my work, Dr. Alan Breakstone, Dr. Mark Gorbics, and Dr. Tom Meyer.

1. INTRODUCTION

1.1. Motivation for Experiment

A good theory to describe strong interactions of particles has been difficult to obtain. Quantum chromodynamics (QCD) is presently the leading candidate for such a theory and has been successful at making correct predictions, where calculations in the theory have been possible. QCD is very nontractable mathematically, and most predictions have required large amounts of computer time utilizing lattice gauge theory combined with Monte Carlo methods [Billoire 1986]. Results on this level look promising, but it is difficult to separate where the disagreements are real from where the calculations are just insufficient. One of the basic reasons that calculations are difficult is that for many cases in QCD perturbation theory is not valid. This is because the QCD coupling constant is large (i.e., on the order of unity). Thus, the method of making an expansion in terms of the coupling constant and using renormalization to cancel infinities in the expansion does not always work because the expansion series converges slowly, if at all.

The quantitative as well as qualitative predictions of QCD must be examined to see if they are born out by experiment. One unique prediction of QCD is the existence of bound states of gluons, which are described in the following sections. The attempted confirmation of these states is one of the major thrusts of the analysis in this paper. In this analysis, an interaction is studied that has a good possibility of producing gluonic bound states, the discovery of which would be a big victory for QCD.

1.1.1. Quantum chromodynamics

A theory of strong interactions has several difficult tasks, and a few of the major ones described here show why a theory of strong interactions is difficult to obtain. It must explain the parton nature of hadrons, but not allow the partons to exist free in nature since these partons (quarks) have never been detected individually. While the theory must not allow the partons to escape confinement, it must permit them to behave in an essentially free manner in regard to scattering (asymptotic freedom). From deep inelastic scattering experiments, it is known that these partons only carry about half of a proton's momentum. Thus, the rest of the momentum is attributed to the field quanta which mediate the strong force (gluons). To explain these properties of strongly interacting particles, in addition to many properties not mentioned, is obviously not an easy task.

With the excellent success of quantum electrodynamics (QED) in describing electromagnetic interactions, it is believed that a gauged field theory is the correct approach to the formulation of a strong interaction theory. Present experimental results reveal that there are five different types of quark "flavors". These five quarks have been given the names "up" (u), "down" (d), "strange" (s), "charm" (c), and "bottom" (b). They are usually arranged in three weak isospin doublets (i.e., the two quarks in a doublet are identical as far as the weak force is concerned), so a sixth quark is expected, which has been given the name "top" (t):

$$\begin{pmatrix} u \\ d \end{pmatrix} \quad \begin{pmatrix} c \\ s \end{pmatrix} \quad \begin{pmatrix} t \\ b \end{pmatrix}$$

The u, c, and t quarks have an electrical charge of +2/3 and the d, s, and b quarks have a charge of -1/3. All of them are spin 1/2 fermions. In order to save the Pauli Exclusion Principle (n.b., the Δ^{++} is made of three u quarks in relative S-wave states) and explain why these quarks have not been found free in nature, the idea that each of these quarks come in three "colors" was invented. This idea requires all free particles in nature to be color singlets. Thus, single quarks as members of a color triplet cannot exist freely in nature. The most direct experimental evidence for color comes from measurements of the total cross section for annihilation of electron-positron pairs in colliding beam experiments [Huang 1982].

These quarks are represented by four-component spinor fields denoted by $q_\alpha^{fi}(x)$, where f is the flavor index, i is the color index, and α is the spinor index. QCD involves gauging the symmetry group $SU(3)_{color}$. It is convenient that its eight generators be represented by the Gell-Mann matrices $\lambda_a/2$ (a = 1,..,8). The gauge fields are referred to as gluon fields in QCD and are represented by $G_a{}^\mu$, where μ is the spatial index, and a is the index referring to the eight different gluons needed for $SU(3)_{color}$, each of which carry a color and an anticolor.

Suppressing the indices on the quark fields, one can write down the interaction Lagrangian density [Huang 1982]:

$$L = L_{gluon} + L_{quark} + L_{ghost}$$

$$L_{gluon} = (1/2)g_o f_{abc}(\partial^\mu G_a{}^\nu - \partial^\nu G_a{}^\mu)G_{b\mu}G_{c\nu} - (1/4)g_o^2 f_{abc}f_{ade}G_b{}^\mu G_c{}^\nu G_{d\mu}G_{e\nu}$$

$$L_{quark} = -(1/2)g_o(\bar{q}\gamma_\mu\lambda_a q)G_a{}^\mu$$

$$L_{ghost} = (1/2)g_o f_{abc}(\eta_a^* \partial_\mu \eta_b)G_c{}^\mu$$

where g_o is the unrenormalized gauge coupling constant, f_{abc} are the SU(3) coupling constants, and $\eta_{a,b}$ are the c-number anticommuting ghost fields (the "ghost" fields are fictitious fields that get introduced during the canonical quantization of the non-abelian theory of QCD due to the non-linear nature of the gauge transformation [Huang 1982]). The term L_{gluon} allows for a three-gluon interaction (first term) as well as a four-gluon interaction (second term), i.e., two gluons in and two out. Thus, the gluons in QCD can interact with each other. This situation is quite different from the case of the field quanta in QED (photons), where the only possible coupling is an $e^+e^-\gamma$ vertex. The four QCD allowed vertices are shown in Figure 1.1, which can be contrasted to the single type of vertex allowed in QED (this vertex is the same as Figure 1.1(c), except that the gluon is replaced by a photon in QED). In QED, it can be thought that photons do not interact with each other because they do not carry an electric charge. In QCD, the gluons carry a color and an anticolor, which can be thought of as a type of strong charge (the analogy with electric charge should not be carried too far), so they not only mediate the strong force, but carry it as well. This is related to the nonabelian nature of QCD and adds greatly to the mathematical difficulties of the theory.

Once one draws a three or four gluon vertex as permitted in QCD (Figures 1.1(a) and (b)), one immediately sees that one could consider the possibility of two or three gluons interacting to form some type of state

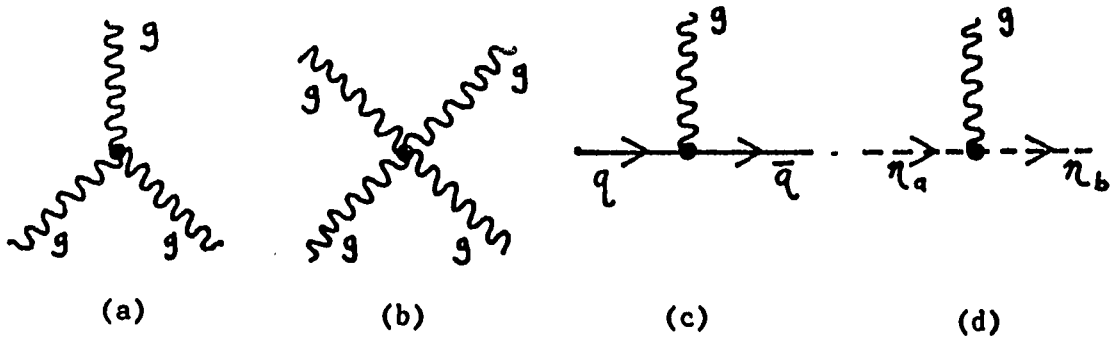

Figure 1.1. Allowed vertices in QCD (a) three gluon, (b) four gluon, (c) quark-gluon, and (d) gluon-ghost

and then decaying into one or two gluons (Figure 1.2). Thus one is led to ask, "Can bound states of gluons exist?". The apparent answer of QCD is "yes", and many calculations seem to demand that these bound states exist for QCD to be correct [Robson 1977, Bjorken 1979]. This is a unique prediction of QCD, and it is important for this prediction to be verified if one is to believe that QCD is the correct theory of strong interactions.

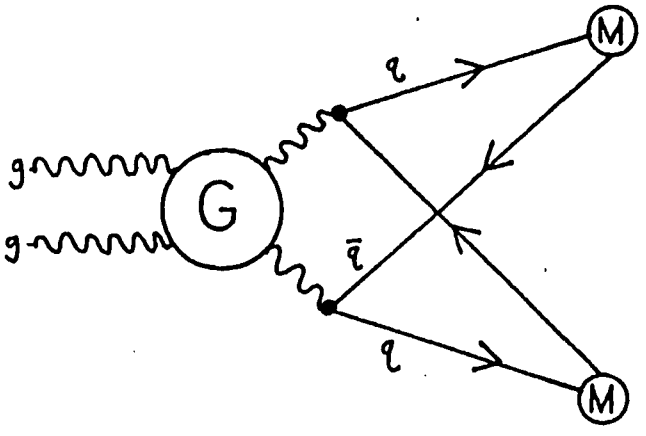

Figure 1.2. Diagram for the decay of a gluonic bound state into ordinary mesons

1.1.2. Characteristics of gluonic states

The expected characteristics of gluonic bound states or "glueballs", has been summarized in several articles and reports [Robson 1977, Bjorken 1979, Chanowitz 1981, Heusch 1985]. One of the first things one needs to know is what quantum numbers are possible for glueballs. Since the wave function for the bound state of two gluons must be totally symmetric (i.e., they are two identical spin one bosons), L+S must be even. Thus, one can have the states given in Table 1.1 [Robson 1977]. With three gluons and L = 0, one can form the three spin states $J^{PC} = 0^{-+}$, 1^{--}, and 3^{--}. One can form other states by using higher L values or by adding more gluons, which would presumably correspond to higher mass states.

Another piece of needed information is the expected mass of these states. There are basically two ways to proceed in order to estimate the masses. One is to study the properties of QCD and use the known properties of quark states to guess what the mass of a glueball should

Table 1.1. Two gluon states [Robson 1977]

L	J^{PC}
0	0^{++}, 2^{++}
1	0^{-+}, 1^{-+}, 2^{-+}
2	0^{++}, 1^{++}, 2^{++}, 3^{++}, 4^{++}
3	2^{-+}, 3^{-+}, 4^{-+}

be. Most arguments result in a bound state of gluons expected to be in the few GeV range. This guessing approach is not very satisfactory, but does give one an idea of the rough values of masses expected. The more quantitative approach is to carry out the calculations in various models of QCD.

Gluons are massless in the normal formulation of QCD; therefore, one must deal with relativistic bound states. This makes the QCD quantitative calculations even more difficult than they were already. Approaches based on heuristic potential models, lattice gauge theories, bag models, and QCD sum rules appear to give comparable results which seem to be reasonable and are summarized in Figure 1.3 [Heusch 1985]. One should note that many mass calculations present their results for each of the gluonic states only as multiples of the 0^{++} mass and then use some expected value of this state's mass to set the mass scale. These multiples of the 0^{++} mass are more trustworthy than the actual quoted masses, because the 0^{++} glueball mass calculations are very uncertain [Meshkov 1984]. Another aspect of these mass values is that they are influenced by the fact that one of the leading glueball candidates is the $\iota(1440)$, which is believed to have $J^{PC}=0^{-+}$, and many calculations will set the mass of the 0^{++} with this in mind. It is still possible at this point in the theory for the quoted glueball masses to be low by 1-2 GeV [Bjorken 1979]. One example of the uncertainties in calculating the glueball masses is a recent result from lattice gauge theory Monte Carlo calculations which gives the 2^{++} state as the lowest glueball state, rather than the 0^{++} state as previously believed [Berg, Billoire, and Vohwinkel 1986].

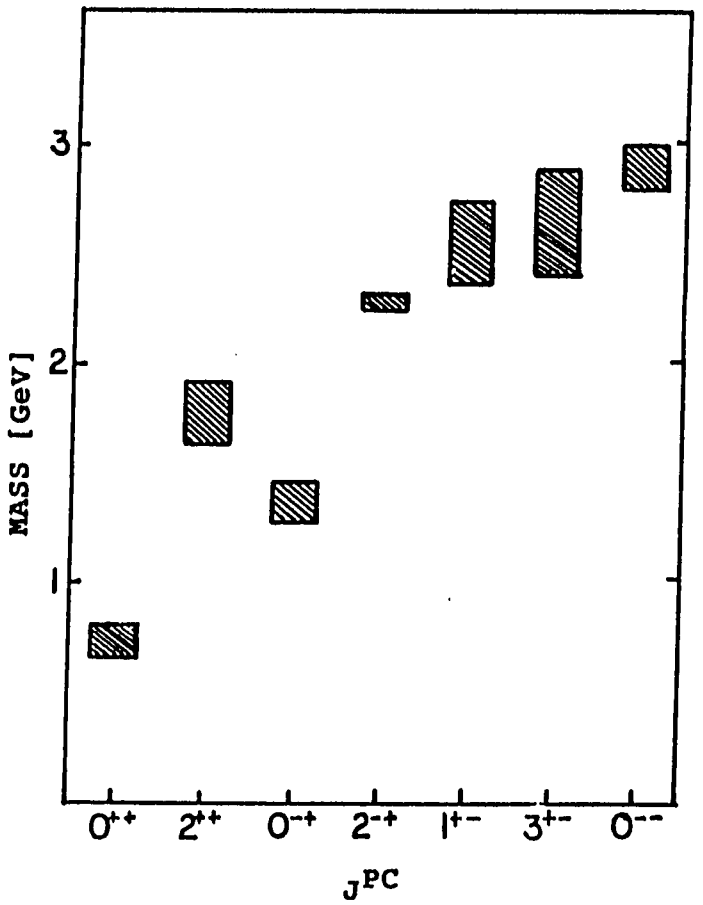

Figure 1.3. Glueball masses for different J^{PC} states [Heusch 1985]

Along with the masses of the glueballs, one needs to know the widths of their decays. Calculations on this area of gluonic states are often in disagreement. Some claim that glueballs have typical hadronic widths, i.e., on the order of 50 MeV or greater, while others claim that they are fairly narrow, with widths on the order of a few MeV [Heusch 1985]. Many calculations predict that the 0^{++} state is very broad and is therefore probably not detectable [Pascual and Tarrach 1982, Gounaris and Paschalis 1985]. Also unresolved is the question of the applicability of the OZI

rule for the suppression of the decays [Chanowitz 1981]. This rule states that disconnected diagrams like Figure 1.4(a) are very much suppressed relative to connected diagrams like Figure 1.4(b). Comparing Figure 1.4(a) to Figure 1.2, one can see that the decay of a glueball into

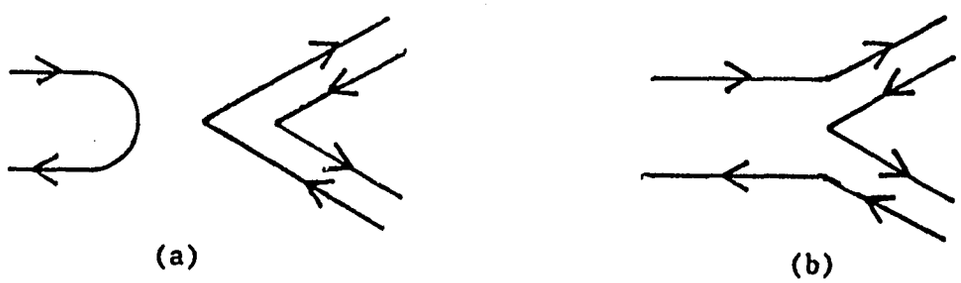

Figure 1.4. Quark digrams showing OZI (a) forbidden and (b) allowed processes

ordinary mesons involves some OZI suppression. By simple counting of the number of vertices one sees that the widths for a glueball or a meson decaying into two ordinary mesons obey:

$$\Gamma(G \rightarrow M_1 M_2) \propto 1/N_{Color}^2$$

$$\Gamma(M \rightarrow M_1 M_2)_{OZI\ allowed} \propto 1/N_{Color}$$

$$\Gamma(M \rightarrow M_1 M_2)_{OZI\ suppressed} \propto 1/N_{Color}^3$$

Thus, a glueball decay width should be the geometric mean of OZI allowed and OZI suppressed decay widths. If this rule does apply, then the conclusion that the states are narrow is probably correct [Heusch 1985]. However, some calculations of the glueball decay widths attempt to get around OZI suppression by introducing intermediate states that are OZI allowed, which creates problems with some meson decay widths that the OZI rule had previously explained [Chanowitz 1981]. Thus, it appears experimentalists must be cautious in relying on theoretical predictions of

the glueball widths. In fact, the measurement of glueball widths will help to clear up some of the theoretical confusion on this point.

Using the information given in this section permits one to specify the allowed decay modes of gluonic states. These are summarized by Table 1.2 [Bjorken 1979]. Some of the entries in the original table have been updated using the Particle Data Group tables [Wohl et al. 1984]. In relation to these decays, there is an often quoted characteristic expected of gluonic decays referred to as flavor symmetry [Lipkin 1981, Lipkin 1982]. Most authors seem to agree that since gluons couple equally to all quarks, that they should then decay equally into all of the quarks except for kinematical and phase space effects (e.g., no preference for u or d quarks as opposed to s quarks) [Heusch 1985].

A final tabulation that is useful for the glueball searcher is a list of quantum numbers and which states are allowed for $q\bar{q}$, gg, and ggg combinations. This is given in Table 1.3 [Coyne, Fishbane and Meshkov 1980].

1.1.3. Present glueball candidates

Presently there are several experimental candidates for gluonic bound states. Here I will just mention the three most common candidates, which are the $\iota(1440)$, the $\Theta(1690)$ and the $g_T(2120, 2220, \text{and } 2360)$. The present status of these states is given in Table 1.4 [Heusch 1985].

For a taste of the debates that have raged on about these states, one needs only to review the history of the $\iota(1440)$. The $\iota(1440)$ is championed as a glueball by some authors [Donoghue and Gomm 1982], some

Table 1.2. Decay modes for low spin gluonia [Bjorken 1979]

Final Mesons	$J^{PC}(L=0)$	$J^{PC}(L=1)$	Components
PP	0^{++}	—	$\pi\pi$, KK, $\eta\eta$, $\eta'\eta'$
PV	1^{+-}	$0^{--},1^{--},2^{--}$	$\pi\rho$, KK^*, $(\eta+\eta', \omega+\phi)$
PA′	1^{--}	$0^{+-},1^{+-},2^{+-}$	πB, KQ, $(\eta+\eta', H+?)$
PS	0^{-+}	1^{++}	πS, $K\kappa$, $(\eta+\eta', S^*+\varepsilon)$
PA	1^{-+}	$0^{++},1^{++},2^{++}$	πA_1, KQ, $(\eta+\eta', D+E)$
PT	2^{-+}	$1^{++},2^{++},3^{++}$	πA_2, KK^{**}, $(\eta+\eta', f+f')$
VV	$0^{++},2^{++}$	etc.	$\rho\rho$, K^*K^*, $\omega\omega$, $\phi\phi$
VA′	$0^{-+},1^{-+},2^{-+}$	etc.	ρB, K^*B, $(\omega+\phi, H+?)$
VS	1^{--}	$0^{+-},1^{+-},2^{+-}$	$\rho\delta$, $K^*\kappa$, $(\omega+\phi, S^*+\varepsilon)$
VA	$0^{--},1^{--},2^{--}$	etc.	ρA_1, K^*Q, $(\omega+\phi, D+E)$
VT	$1^{--},2^{--},3^{--}$	etc.	ρA_2, K^*K^{**}, ωf, $\phi f'$

Notation:

P:	$^1S_0(0^{-+})$	π, K, η, η'
A′:	$^1P_1(1^{+-})$	B, Q, H, ?
V:	$^3S_1(1^{--})$	ρ, K^*, ω, ϕ
S:	$^3P_0(0^{++})$	$\delta, \kappa, S^*, \varepsilon$
A:	$^3P_1(1^{++})$	A_1, Q, E, D
T:	$^3P_2(2^{++})$	A_2, K^{**}, f, f′

Table 1.3. Allowed J^{PC} states [Coyne, Fishbane, and Meshkov 1980]

J^{PC}	$q\bar{q}$	gg	ggg	J^{PC}	$q\bar{q}$	gg	ggg
0^{++}	yes	yes	no	2^{++}	yes	yes	yes
0^{+-}	no	no	yes	2^{+-}	no	no	yes
0^{-+}	yes	yes	yes	2^{-+}	yes	yes	yes
0^{--}	no	no	yes	2^{--}	yes	no	yes
1^{++}	yes	yes	yes	3^{++}	yes	yes	yes
1^{+-}	yes	no	yes	3^{+-}	yes	no	yes
1^{-+}	no	yes	yes	3^{-+}	no	yes	yes
1^{--}	yes	no	yes	3^{--}	yes	no	yes

say the situation is somewhat confused as to the nature of the ι(1440), while others say that it is probably not a glueball [Heusch 1985].

1.1.4. Difficulties in finding gluonic states

One of the main conclusions of all the recent glueball studies is that anything found to be consistent with being a glueball can probably be explained by another hypothesis as well. One of the first problems after a new state is found is to show that it cannot be a $q\bar{q}$ state. While meson spectroscopy is fairly well known below a few GeV, there are still enough problems to make the separation of quarkonic and gluonic states difficult. If these two types of states are near each other and have the same

Table 1.4. Simple checklist for three glueball candidates [Heusch 1985]

Candidate State:	ι(1440)	Θ(1690)	$g_T(1,2,3)$
J^{PC}	0^{-+}	2^{++}	2^{++}
SU(3) singlet	yes	yes	yes
mass[GeV]	1.4	1.7	~2.2
width[GeV]	0.1	0.13	0.2
seen in several channels?	yes	yes	no
flavor independent decay?	no	maybe	probably not
radiative mode?	yes	no	no
seen only in gluon rich channel?	yes	yes	?
Rating (1...10)	2	3	2

quantum numbers, mixing can certainly be a problem. For example, it has been proposed that the f^0 is a mixture of meson and glueball states [Rosner 1981]. This same possibility has been put forward for the f'(1525), and Θ(1690) [Schnitzer 1982], as well as for the η and η' [Carlson and Hansson 1982].

Another problem is that non-glueball exotic states are also possible in QCD. One of the basic ideas of QCD is that only states that are color singlets can exist. By using basic group theory and the representations of quarks and gluons in $SU(3)_{color}$, one can see what types of bound states

are allowed. Quarks are in a representation of rank three (3) of color, antiquarks are in the conjugate representation of rank three (3^*), and gluons are in a color representation of rank eight (8). Thus, our regular mesons ($q\bar{q}$) and baryons (qqq) are permitted since:

$$3_c \times 3_c^* = 1_c + 8_c$$

$$3_c \times 3_c \times 3_c = 1_c + 8_c + 8_c + 10_c$$

Likewise a color singlet can be made out of two (or any larger number) gluons since:

$$8_c \times 8_c = 1_c + 8_c + 8_c + 10_c + 10_c + 27_c$$

In addition to these combinations, it is also possible to form $qq\bar{q}\bar{q}$ [Jaffe 1977] and $q\bar{q}g$ [Chanowitz 1981, Yaouanc et al. 1985] color singlets since:

$$3_c \times 3_c \times 3_c^* \times 3_c^* = (1_c + 8_c) \times (1_c + 8_c)$$

$$3_c \times 3_c^* \times 8_c = (1_c + 8_c) \times 8_c$$

It is particularly important to note that for L = 0 between the gluon and the two quarks one can form every J^{PC} combination except 0^{+-}, and this state can be formed with the addition of only a single unit of angular momentum [Coyne, Fishbane, and Meshkov 1980].

With the additional possibility of these exotic states, one can begin to see the difficulty of isolating a glueball state. When one considers the above, combined with the uncertainty of QCD calculations, the search for glueballs looks even less promising. However, the fact that a task is very difficult (some say impossible) is not a sufficient reason to refuse to attempt it. The prediction of glueballs is important for QCD, and this prediction needs to be confirmed or disproved.

1.2. Double Pomeron Exchange and Gluonic States

The model of Pomeron exchange has proven to be very useful for peripheral reactions at high energies. The name "Pomeron" comes from the name Pomerancuk, who was the man who worked out that at high energies the elastic cross sections for particles and antiparticles should become equal and be isospin-independent [Perkins 1982]. This result is known as the Pomerancuk Theorem.

Experiment has shown that the total cross section is nearly constant at high energies, and Regge theory has been very successful at describing this and other features of high energy scattering. What Regge theory basically does is treat the angular momentum as a continuous complex variable $\alpha(E)$, which is a function of energy. The angular momentum dependence is given by the real part (i.e., $L = \mathrm{Re}\alpha(E)$, where the angular dependence is given by the Legendre polynomials, $P_L(\cos\theta)$). Physically observable states must have integral or half-integral momenta. The path in the complex energy plane followed by α as E increases is called a Regge trajectory. When $\mathrm{Re}\alpha(E) = L =$ integer, a resonant state can occur. Each of the resonances, or "poles", on a given trajectory must have the same quantum numbers except for their angular momentum [Perkins 1982]. Since this includes the parity of the states, one sees immediately that resonances must be separated by two units of angular momentum ($P = -1^L$).

For the total cross section to be nearly constant at high energies, one needs $\alpha(0) = 1$ [Perkins 1982]. If this one trajectory is to account for all elastic scattering phenomena, it must have the quantum numbers of the vacuum, since no quantum numbers (i.e., strangeness, charm, isospin,

etc.) apart from angular momentum may be exchanged in such processes [Perkins 1982]. Since the exchange of a vacuum pole dominates the elastic scattering process, it is implied that the elastic cross sections for particles and antiparticles must be equal, just as the Pomerancuk theorem states. Thus, this "vacuum" trajectory is also called the Pomerancuk trajectory, and the "particle" exchanged in the interaction is termed the Pomeron. The Pomeron exchange process can account for many characteristics of quasi-elastic processes, in addition to purely elastic scattering. By quasi-elastic we mean that one of the incident particles involved is excited slightly, and the other particle is basically undisturbed except for a small momentum transfer (e.g., diffractive scattering). In order for Regge theory to correctly describe these interactions, in addition to other aspects of peripheral scattering, one must do much more work that is well described in the literature [Amaldi, Jacob, and Matthiae 1976]. However, the above discussion is adequate for what needs to be understood for the interaction studied in this paper.

1.2.1. Description of DPE process

An important test of the Pomeron exchange model is to look at the case where two Pomerons are exchanged instead of one. This process is termed Double Pomeron Exchange (DPE). When viewed in the center of mass frame, this results in two fast forward outgoing systems, consisting of the quasi-elastically scattered protons as well as a slow central system consisting of whatever is formed by the interaction of the two Pomerons. This means that the Feynman x, (i.e., the ratio of a particle's

longitudinal momentum to its maximum allowable longitudinal momentum) of the two protons remains close to unity, and all other particles produced in the reaction have a Feynman x near zero. The cross section for this process is 10-30 μb, which is only about 1/2000 of the total cross section at the energies used in this experiment. Therefore, this is a rare process and requires careful set-up of an experiment in order to single out these events.

The DPE process is best pictured by a diagram depicting the rapidity of the outgoing particles of the interaction (Figure 1.5) [Drijard et al. 1978]. The rapidity of each particle is defined by the equation:

$$y = \frac{1}{2} \ln\left(\frac{E + p_L}{E - p_L} \right)$$

where p_L is the longitudinal (along the beam axis) momentum of the

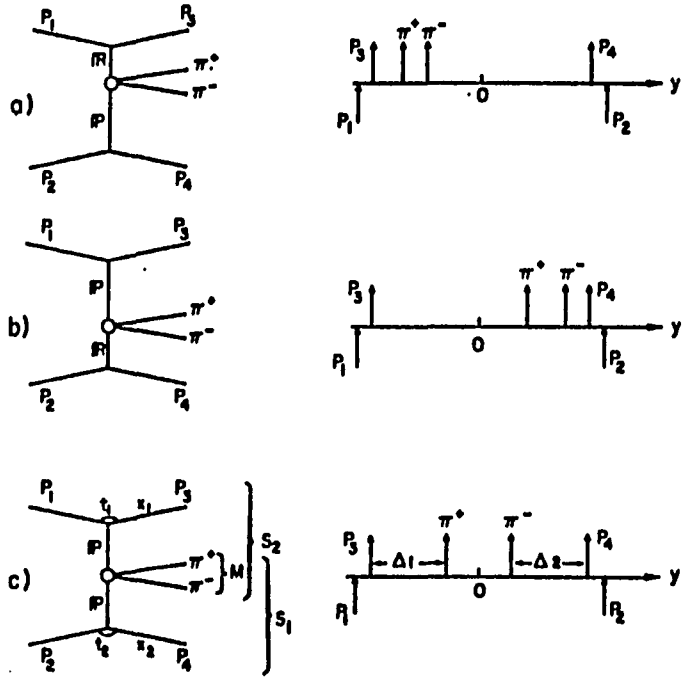

Figure 1.5. Diagrams for (a) and (b) diffractive scattering (Reggeon-Pomeron exchange) and (c) Pomeron-Pomeron exchange (DPE)

particle. The large rapidity gaps Δy_1 and Δy_2, between the fast protons and the central system, shown in Figure 1.5(c), are an important characteristic of DPE. This is one property of a DPE event that one can use to distinguish it from other types of interactions.

The double-inclusive distribution for the two quasi-elastically scattered protons is given by [Amaldi, Jacob, and Matthiae 1976]:

$$\frac{x_1 x_2 d^2\sigma}{dx_1 dx_2 dp_{T1}^2 dp_{T2}^2} = \frac{1}{8\pi^2}\gamma^2(t_1)\gamma^2(t_2)|\eta(t_1)||\eta(t_2)|\frac{\sigma_{PP}(M^2,t_1,t_2)}{(1-x_1)^{2\alpha(t_1)-1}(1-x_2)^{2\alpha(t_2)-1}}$$

where γ and η correspond respectively to the proton couplings and signature factors of the relevant Reggeons, α is the Regge intercept ($\alpha = 1$ for the Pomeron), p_T is the transverse momentum of the protons, M is the mass of the central system, t is the momentum transfer of each proton, x is the Feynman x of each proton, and σ_{PP} is the total Pomeron-Pomeron cross section. In the above equation the asymptotic expressions:

$$\frac{s}{E_i} = \frac{1}{1-x_i} \quad \text{and} \quad M^2 = s(1-x_1)(1-x_2)$$

were used. This equation is the basis for the statement that DPE is the only contribution to the total cross section that includes a double-pole term as x_1 and x_2 approach one. This can be seen by setting $\alpha(t) = 1$, i.e.:

$$\frac{d\sigma}{dx_1 dx_2} \sim \frac{1}{(1-x_1)(1-x_2)}$$

whereas other terms in the total cross section would behave as [Amaldi, Jacob, and Matthiae 1976]:

$$\frac{d\sigma}{dx_1 dx_2} \sim \frac{1}{1-x_1} + \frac{1}{1-x_2}$$

It must be noted that this behavior holds only in the large M^2 limit which is not completely valid at the center of mass energies of this experiment. Therefore, one needs to be cautious in studying the x_1, x_2 dependence of the cross section. If M^2 is not high enough, this double-pole behavior might not be evident. However, one can study plots of x_1 versus x_2 to see what the distribution looks like. If the dominant reaction is single diffraction, then there should be a depletion of events in the region where both x's are near unity. One should also note that there is no s dependence in the double-inclusive distribution for DPE. This is why one expects the effective mass distribution for DPE to have the same form for different energies.

Other kinematical characteristics of DPE include the expectation that the transverse momenta of the two outgoing fast protons should be uncorrelated with each other. In particular, the azimuthal angles of the outgoing protons about the beam axis should be uncorrelated. Also, the momentum transfers at the proton vertices t_1 and t_2, should show no correlation with each other. In addition, the diffractive process should limit these momentum transfers to low values, as otherwise the process would no longer be peripheral. This means that each proton momentum transfer should fall off rapidly as t increases. This behavior in elastic scattering is well fit by the exponential function e^{bt}. For DPE this same behavior is expected to hold, with b being equal to one-half of the value of b for elastic scattering at the same energy [Drijard et al. 1978].

A final important signature of the DPE process concerns the possible quantum numbers of the central system formed by the two Pomerons. The Pomeron carries the quantum numbers of the vacuum (i.e., $J^{PC} = 0^{++}$).

Since the two Pomerons are identical bosons, the system they compose must be symmetric in the spatial part of its wave function as well as being symmetric in its overall wave function. Thus, the orbital angular momentum must be even (i.e., $L = 0,2,4,...$), and since the Pomerons carry no spin, the total angular momentum must be even as well. Also, the parity must be even ($P = -1^L$), and the charge conjugation must be even ($C = -1^{L+S}$). Therefore, only the states $J^{PC} = 0^{++},2^{++},4^{++},...$ are possible for the central system.

By looking at the effective mass of the two pion central system, one has an easy check to see if an interaction is being dominated by single diffraction or DPE. Ordinarily a large ρ^o (i.e., $\rho^o \rightarrow \pi^+\pi^-$) signal is seen in single diffraction and in general particle production reactions. In DPE, this signal must be absent since J^{PC} of the ρ^o is 1^{--}. Further angular momentum analysis should also be able to confirm if the central system is being produced predominately by DPE at effective masses away from the ρ^o mass.

As previously mentioned, DPE is a rare process but has certain characteristics that allow one to select events that should be produced mainly by DPE. The detector used for this experiment has previously been able to separate out a possible DPE signal [Drijard et al. 1978]. This allows one to build on previous results to insure success of collecting a sizable set of DPE events to study.

1.2.2. Gluonic character of DPE process

The idea of the Pomeron being composed of gluons was put forward as a result of QCD's success in explaining strong interactions. The reason for this is simply that the Pomeron was invented as a phenomological model, not as a fundamental theory of strong interactions. The model is useful, in that it allows one to calculate cross sections (something QCD cannot do very well as yet) and explain many features of strong interactions, but one would like to understand the Pomeron in the terms of the basic constituents of matter. This means explaining the Pomeron model in terms of quark and gluon exchange.

It has been attempted to explain Pomeron exchange as a multigluon exchange process [Nussinov 1975, Low 1975]. The model by Low (Nussinov's is similar) is for a "bare" Pomeron, meaning a mechanism which accounts for constant total cross sections, zero real parts of scattering amplitudes, and limiting fragmentation (or Feynman scaling). It consists of the exchange of confined, colored gluons between confined quarks and accounts for the properties just mentioned. This work is given further support by showing that a dynamical model of the Pomeron based on QCD accounts for various hadron cross-sections [Pumplin and Lehman 1981]. Another model, called the subtractive quark model also explains the Pomeron as arising from gluon exchange between quark constituents (this model is implicit in the work of Low and Nussinov) [Pumplin and Lehman 1981].

The are several shortcomings in these attempts to bring the Pomeron model into the structure of QCD. One is that diffractive scattering, the

process for which the Pomeron is so important, does not lie in the realm of perturbative QCD. Yet the works mentioned above involve perturbative calculations [Richards 1985]. Due to the models of the hadronic wave function used, these calculations make it difficult to implement gauge invariance [Richards 1985].

Even with its shortcomings, the theory of a Pomeron being composed of multiple gluons certainly seems likely, in that some sort of gluon exchange is taking place. If the Pomeron is indeed gluonic in nature, then the state formed by the two Pomerons in DPE might produce a gluonic bound state, and this is the basis for using this interaction to search for glueballs [Robson 1977].

2. DETAILS OF EXPERIMENT

This experiment was conducted using facilities at the European Organization for Nuclear Research (CERN) in Geneva, Switzerland. The CERN Laboratory, as its name indicates, is a collaboration of European countries for research in particle physics. It supports accelerator programs in different areas of particle physics research and is an excellent example of international collaboration in basic science research. The accelerator facility used for this experiment was the Intersecting Storage Rings (ISR), and the detector utilized was the Split Field Magnet.

2.1. Description of the ISR

The ISR consist of two interleaved proton storage rings that allow the stored protons to collide almost head-on. Head-on collisions allow one to reach much higher center of mass energies than with fixed target machines of the same beam momentum. In a colliding beam machine, the center of mass energy is twice the energy of each beam, while for a fixed target machine, the center of mass energy increases proportionally to only the square root of the beam energy. For example, the highest center of mass energy of 63 GeV for the ISR is achieved with two beams of 31.5 GeV, but would require a fixed target accelerator with a beam momentum of over 2000 GeV to match it. However, due to the absence of a dense target, this gain in energy is paid for in the loss of interaction rate by many orders of magnitude.

2.1.1. Layout of the ISR

The layout of the ISR with the associated accelerators which inject the proton beams into the ISR are shown in Figure 2.1. The ISR consist of two interleaving rings about 300 meters in diameter which intersect in eight places [Keil 1972]. These rings, or beam lines, are evacuated pipes in which a proton beam can circulate, guided and focused by magnets placed around the rings. The rings are filled with counterrotating proton beams, which collide with each other where the rings intersect. The opening angle, or horizontal crossing angle, of the two beams at an interaction point is about 14.8 degrees. The pressure in the beam pipes is maintained below 10^{-13} torr in the intersection regions and is kept below 10^{-11} torr

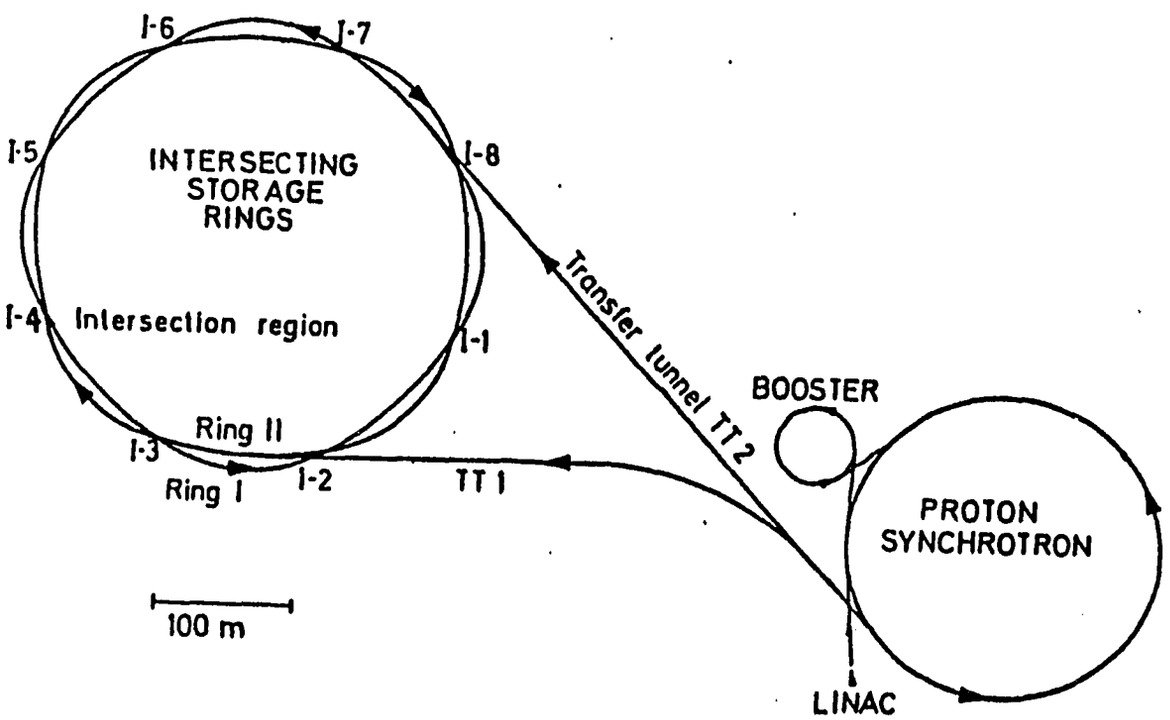

Figure 2.1. Layout of the ISR and their injection lines

everywhere else in the beam pipes. This ultra high vacuum is necessary to avoid the beam protons interacting with residual gases in the beam pipe, which would produce unacceptable background conditions and reduce the lifetime of the circulating beams.

2.1.2. Accelerating process for the ISR

The acceleration process begins with a Cockcroft-Walton accelerator that has hydrogen ions supplied to it by a duoplasmatron ion source. The ion source operates in a pulse mode, and repeated pulses are necessary in order to produce enough protons to perform physics experiments [Michaelis 1981]. This proton pulse is accelerated to 750 KeV by the Cockcroft-Walton stage [Michaelis 1981], and each pulse is then injected into a linear accelerator (linac) where it is accelerated to 50 MeV. These proton pulses are then injected into a booster synchrotron, which accelerates them to 800 MeV and collects these pulses until a large proton bunch is accumulated (containing $\sim 10^{13}$ protons). This group of pulses is then injected into the Proton Synchrotron (PS) which is the final acceleration stage before the protons are injected into one of the two rings of the ISR. For this experiment the highest ISR energy was used, so the protons were injected into the ISR at the maximum energy the PS could supply (26.5 GeV).

Because the phase space available for the protons is much larger in the ISR than the PS, it takes a few hundred injections from the PS until the apertures of the ISR beam lines are filled. The apertures of the ISR beam lines are filled horizontally, and this results in a final proton

beam which is in the form of a thin ribbon about 1 cm high and 6 cm wide. Currents as high as 60 amps have been achieved, but for operation at the highest ISR energy, a current of about 30 amps is normally used. The acceleration of the protons to their final momentum of 31.46 GeV is performed in the ISR themselves [Henrichsen et al. 1974, Fischer et al. 1979].

2.1.3. Other parameters of interest

In a colliding beam machine the number of interactions per second is given by [Hubner 1977]:

$$\frac{dN}{dt} = \frac{\sigma}{ce^2} \frac{I_1 I_2}{h \tan(\alpha/2)}$$

where I_1 and I_2 are the beam currents, α is the crossing angle of the two beams, h is the height of the beams, and σ is the cross-section for the interaction. From this one can define the luminosity [Hubner 1977]:

$$L = \frac{1}{\sigma} \frac{dN}{dt} = \frac{1}{ce^2} \frac{I_1 I_2}{h \tan(\alpha/2)}$$

which is just the counting rate for a unit cross section. The luminosity depends on the beam height but not on the beam width because the ISR beams cross in the horizontal plane.

The data involved in this experiment were recorded in what is called the "low β" mode of the ISR. The reason for this name is that the beam height depends on the beam's vertical betatron oscillation. Thus by lowering the magnitude of the vertical betatron oscillation, one reduces the height of the beam. This is accomplished by a special arrangement of

quadrapole magnets around the I7 intersection region, which increases the luminosity at I7 by more than a factor of two. The importance of knowing in what mode the ISR were operated is that when one does something to the beam at one intersect, it has an effect on the other intersects as well. More details about the beam parameters at the I4 intersect, where the detector used for this experiment is located, will be given in Chapter 3.

2.2. Description of the SFM Detector

This experiment was conducted using the Split Field Magnet detector, which is located at intersect I4 of the ISR. The requirements for a detector in an experiment in which the laboratory frame is almost the center of mass frame are quite different from those for a detector in a fixed target experiment. First, since one is using storage beams for interactions, any analyzing magnet must have a net $\int B \cdot dl$ of zero. In other words, the beam must not be given any net deflection by the detector. Another requirement is that one must have full solid angle coverage in order to completely measure an event. With a fixed target detector this is not necessary since the Lorentz boost from the center of mass frame to the lab frame frequently confines all outgoing particles to a forward cone. Also, a detector at the ISR must be capable of handling the event rate (luminosity) and be able to set up special selection (trigger) criteria to only record events of special interest. For a DPE trigger, one must be able to identify events with two fast protons (high rapidity) and a slow central system (low rapidity) as indicated in Chapter 1. As will be seen, the SFM is capable of handling a trigger with such varied requirements.

2.2.1. SFM Magnet

The name, Split Field Magnet, comes from the type of field produced by the analyzing magnet of the detector. The field is vertical and is arranged so that the field direction is up on one side of the detector and down on the other side, thus making $\int B \cdot dl = 0$. The presence of the magnet allows one to measure the charge and momentum of reconstructed particle tracks in the detector. Because of the dipole arrangement of the magnetic field, charged particles emerging horizontally at 90° from the beam bisector (this is the y-axis in Figure 2.4) are not bent very much in the field and hence are poorly measured. Also, vertical components of momenta are poorly measured since the field itself is largely vertical. In addition to the large dipole magnet, there are compensator magnets on the upstream and downstream segments of the beams in order to correct for the small distortions in the beams caused by the SFM. Figure 2.2 shows a side and top view of this magnet system. To give one an idea of the size of this detector, some of the parameters of the magnet are given in Table 2.1 [Heiden 1982].

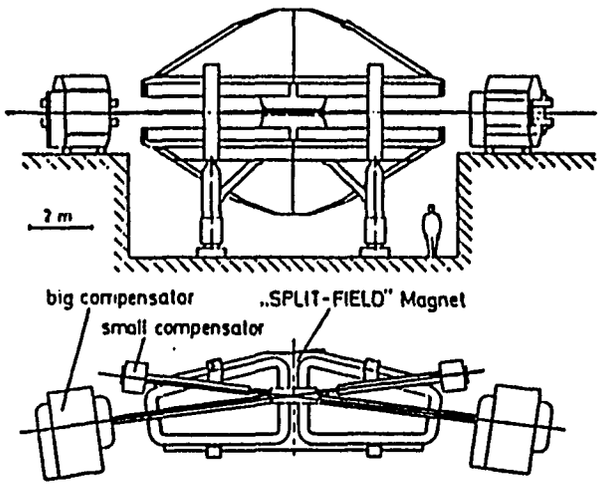

Figure 2.2. Side and top views of detector magnet and compensators

Table 2.1. SFM magnet parameters

Total length	10.3 m
Width	2. to 3.5 m
Height	7.2 m
Distance between pole pieces	1.1 m
Effective magnetic volume	28 m^3
Total iron weight	840 metric tons
Total copper weight	42 metric tons
Maximum field strength	1.14 Tesla

The field of the SFM has been measured with great accuracy, and knowledge of the field is not a significant source of error in track reconstruction [Metcalf 1974]. For this experiment all data were taken with the standard conditions for beam momenta of 31.46 GeV. Thus, the magnetic field of the SFM was set at 1.0 Tesla, resulting in a horizontal crossing angle of the beams of 17.477 degrees [Bryant 1973]. This results in a center of mass motion of $\beta_{cm} = \beta_{beam}\sin(17.477^{o}/2)$ inward towards the center of the ISR.

2.2.2. SFM chamber layout

The volume between the pole pieces of the SFM is filled with multiwire proportional chambers (MWPCs). This system of MWPCs has been described in several papers [Bouclier et al. 1974, Bouclier et al. 1975, Brandt et al. 1975, Bell et al. 1975, Bell et al. 1978]. Figure 2.3 shows a cutaway view of the detector, and the layout of these chambers is shown

in Figure 2.4. From these two figures it can be seen that the SFM separates naturally into three logical groups of MWPCs. There is the central region which detects particles produced at large angles with respect to the two proton beams (e.g., the slow central system of DPE events) and two forward telescopes to detect particles produced at small angles with respect to the two proton beams.

In order to avoid large losses in acceptance (i.e., holes in the detector where particles can escape undetected), these chambers were constructed to be self-supporting (i.e., frameless) [Bouclier et al. 1974]. This was accomplished by using a foam-sandwich type design where a polyurethane sheet with a thin layer of silver sprayed on it serves as both support and cathode of the MWPC. The gain in acceptance by this design is paid for in a substantial increase of material that the particles must pass through, $\simeq 0.6$ g/cm^2 compared to a few mg/cm^2 for conventional chambers, resulting in energy losses and multiple scattering effects. Table 2.2 lists the number of planes and wire spacings for each of these chambers [Heiden 1982], where V, H, and I stand for vertical, horizontal, and inclined planes respectively. The first digit of the chamber indices indicate in which telescope they are contained (Figure 2.4). The 300 chambers make up the $-y$ axis forward telescope, and the 400 chambers make up the $+y$ axis forward telescope. These two sets of chambers are identical, so only the 300 chambers are listed in Table 2.2.

In addition to the MWPCs, which can only record whether or not individual wires are hit, there are also chambers (109 and 209) equipped with analog readouts. These chambers can be used for particle identification. These analog chambers are located close to the

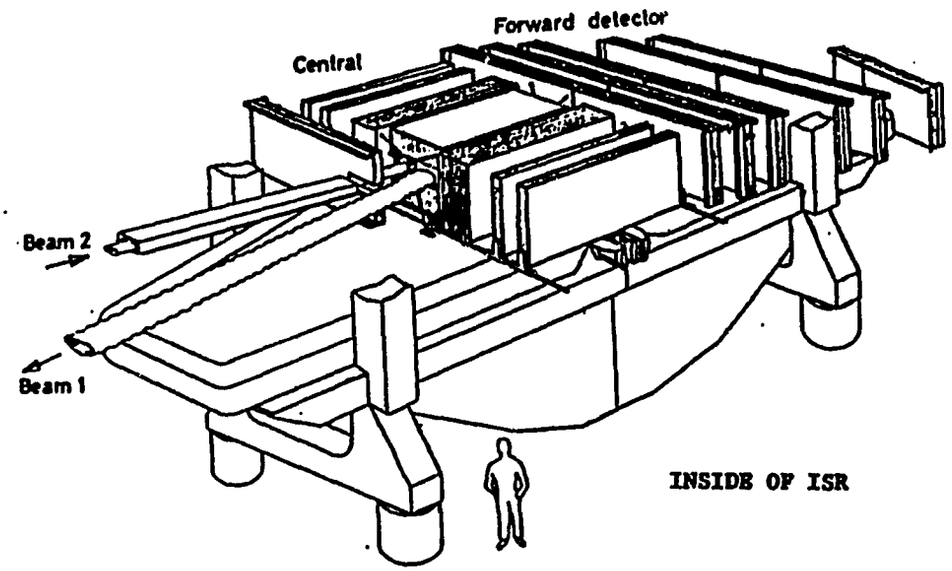

Figure 2.3. Cutaway view of the Split Field Magnet Detector

Table 2.2. Data on the MWPC's parameters

Chamber index	number of V H I -planes	wire spacing (cm)
200,100	4 4 2	0.4
201,202,101,102	1 1 1	0.4
209,109 (analog readout)	3 1 0	0.4
360,350	2 2 1	0.4
600,500	5 4 2	0.4
320,310,314	3 3 2	0.4
321,322,323,324,311,312,313	1 1 0	0.4
325,315,326,316,327,317	1 1 0	0.2
300,301,302,303	2 2 2	0.4

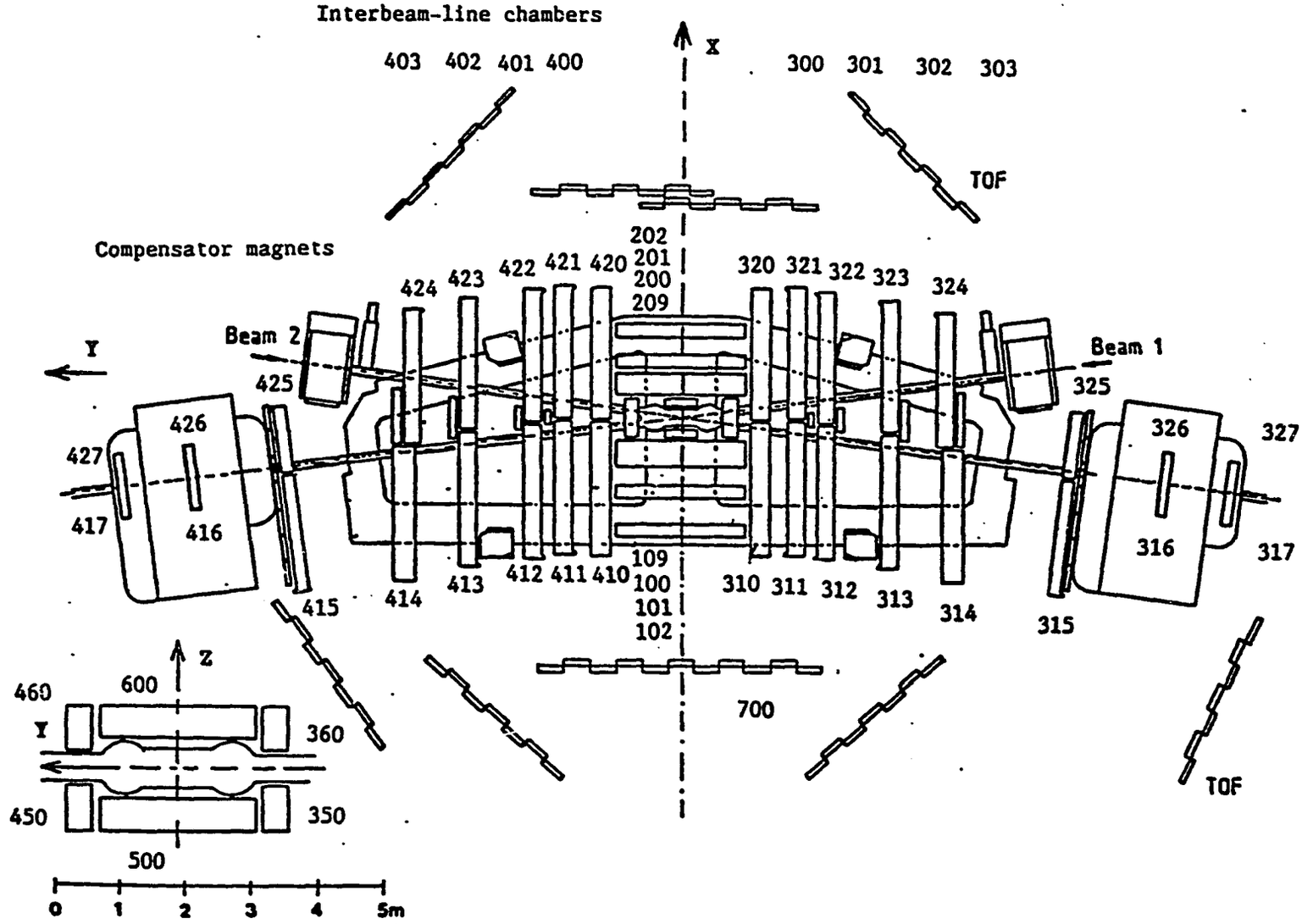

Figure 2.4. Top view of the chamber layout for the SFM detector

interaction region and cover about 15% of the total solid angle. Using the analog readout, the energy deposited in the chamber by a particle can be recorded. Since the energy loss of a charged particle in traversing a medium is inversely proportional to the square of its velocity, this energy loss can be combined with the measured momentum to estimate the mass of the particle. A well known problem of such dE/dx measurements is that there are large Landau fluctuations in the energy loss of a charged particle. Since there are only four planes in the SFM dE/dx chambers, particle identification by this system is very limited and was used with caution in this experiment.

The other part of the detector of particular importance to this experiment is the time-of-flight (TOF) system. This is an array of scintillation detectors set up around the SFM (Figure 2.4) and is used for particle identification. There are 67 counters arranged in eight modules of seven counters each and one module of eleven counters. The size of a single scintillator is 225 cm high by 40 cm wide by 2 cm thick, resulting in a coverage of about ten percent of the total solid angle. Each scintillator is viewed by two photomultiplier tubes situated at its two ends, which are read out by both analog (ADC) and time digitizing (TDC) units. A diagram of a single counter is shown in Figure 2.5 [Heiden 1982]. The analog signal is used for the trigger logic, and the time signal is used for accurate timing information. The basic idea of a TOF system is to measure the flight time of a particle. When combined with the length of the measured trajectory, this gives the velocity of the particle. Since the momentum of the particle is measured using the MWPC system inside the magnet, one can get an estimate of the mass of the

particle by using the equation:

$$t_f^2 \, p^2 = L^2(m^2 + p^2)$$

where t_f is the measured time-of-flight, L is the length of the particle's trajectory, p is the particle's momentum, and m is its mass.

In addition, the SFM is equipped with a set of Cerenkov light detectors which are for particle identification. Since these detectors were not used in this DPE experiment, they are not shown in the layout of the SFM.

2.3. DPE Trigger Setup

As discussed in Chapter 1, DPE events are characterized by two quasi-elastically scattered protons and a slow central system. Thus, all triggers used in data collection required a fast positively charged

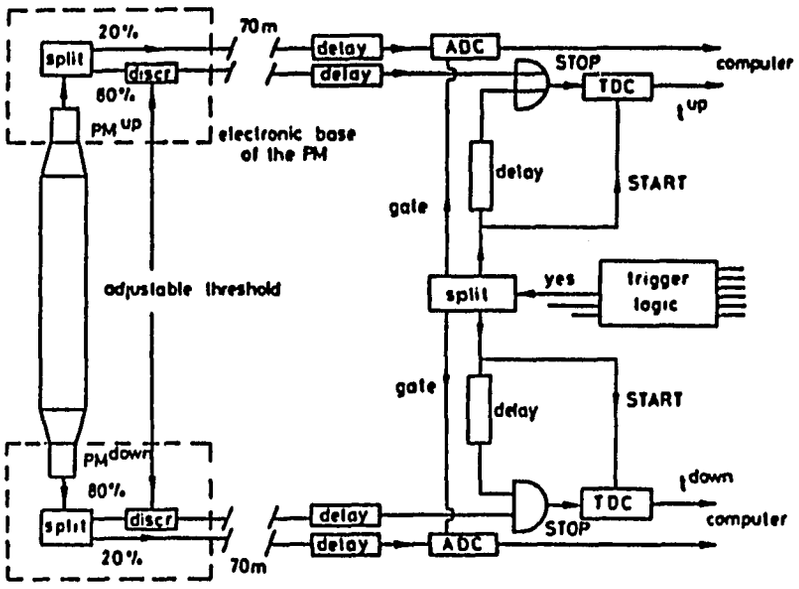

Figure 2.5. Readout diagram of a single time-of-flight counter

particle in each of the two forward telescopes. This was combined with an intermediate angle veto to force the large rapidity gap between the fast protons and the central system. There were three different types of requirements placed on the central system, and each sample will be examined separately.

2.3.1. OR trigger

The central region of the SFM detector can be divided along its y-axis (Figure 2.4) into two halves, one toward and one away from the ISR center. One data sample was recorded which required the presence of a track candidate in at least one of these two halves, in addition to the two fast positively charged particles in the forward telescopes. This requirement is why this trigger is referred to as the "OR" trigger. In order to force the two large rapidity gaps between the forward protons and the central region, characteristic of DPE events, the intermediate angle chambers were used as vetoes.

These requirements were performed by two triggers, one referred to as Fast13 and the other as Slow13. These requirements can be summarized by the logical statements below, where both Fast13 and Slow13 must be true in order for the event to be recorded [Breakstone 1982]:

$$\text{Fast13} = \text{TIME}\cdot\text{T1T2}\cdot\text{IAV3}\cdot\text{IAV4}\cdot\text{CENTRAL}$$

$$\text{Slow13} = (\text{R1}=1)\cdot(\text{R2}=1)$$

where "$\cdot$" means a logical .and. operation. Each of these requirements of the trigger are as follows:

TIME: general timing signal for all chambers of the SFM generated by a logical or of all the chambers

T1T2: coincidence of the two time-of-flight counter banks surrounding the outgoing beam pipes

IAV3: none of the -y side veto chambers were hit, these were chambers 301, 302, 312, 322, 313, and 323

IAV4: none of the +y side veto chambers were hit, these were chambers 401, 402, 412, 422, 413, and 423

CENTRAL: there was at least one track candidate in the central region of the SFM

R1=1: there was a quasi-elastic proton candidate in +y telescope

R2=1: there was a quasi-elastic proton candidate in -y telescope

With a luminosity of 1.06×10^{31} $cm^{-2}s^{-1}$, the trigger rates for the above conditions were 548 Hz for the Fast13 trigger and 137 Hz for the Slow13 trigger. The data acquisition was actually limited by the speed at which data could be written out to magnetic tape, giving a data acquisition rate of only 52 Hz.

2.3.2. AND trigger

Another trigger was used that is very similar to the OR trigger. The only change from the above requirements was that this trigger required at least one track candidate in each half of the central region of the SFM, and thus this trigger is referred to as the "AND" trigger. With the same luminosity as above, the trigger rates were 86 Hz for the Fast13 trigger and 20 Hz for the Slow13 trigger. This resulted in a data acquisition rate of 17 Hz.

2.3.3. TOF trigger

The final trigger used in this experiment was implemented to enrich the number of kaons and protons produced in the central region in the event sample. This was done in order to look for states which exhibit flavor symmetry, a previously mentioned characteristic of gluonic bound states. Ordinarily over 90% of the particles produced in the central system are pions. Thus, with the OR and AND triggers it is not possible to look for flavor symmetry signals due to low statistics.

In order to implement this enrichment of K^+K^- and $p\bar{p}$ pairs produced in the central region, the time-of-flight system of the detector was used. Thus, this trigger is referred to as the "TOF" trigger. Since kaons and protons have higher masses, they will be slower than pions with the same momenta. Thus, by biasing the data toward slower particles in the central region, one increases the percentages of kaons and protons. This was done by adding a requirement using one of the TOF stands in the central trigger. The TOF stand must not be hit until after some set delay time in relation to the timing signals that signal the beginning of the event. The time reference used was the T1T2 signal that signifies that the time-of-flight counters surrounding the outgoing beam pipes have been hit (this is the same T1T2 as in the Fast13 trigger). For the data analyzed in this work, delays of 32, 34, and 36 nanoseconds (ns) were used, with the majority of the data taken with a 32 ns delay. A delay of less than 24 ns does little to enrich the data, and a delay of greater than 36 ns cuts the data rate severely. These delays allowed the collection of roughly as many kaons and protons as pions in the central system.

The 700 TOF stand was used for this trigger delay. Thus, the central region trigger particle had to go through the -x half of the central region of the detector. In order to make sure that the signal from the TOF stand came from the same track as the central trigger, a crude DC road system was set up for the TOF 700 counters. These "roads" are simply groups of wires that are logically or'ed together and then used to form coincidences with each individual slab in the TOF 700 bank. As well as these changes, the veto conditions were relaxed somewhat for the TOF trigger. The Fast13 and Slow13 triggers in this case were:

$$\text{Fast13} = \text{T1T2}\cdot\text{IAV3}\cdot\text{IAV4}\cdot\text{CC1}\cdot\text{DELAY}$$

$$\text{Slow13} = (\text{R1=1})\cdot(\text{R2=1})\cdot\text{TOF700DC}$$

where T1T2, R1=1, and R2=1 are the same as in Section 2.3.2. The other logic requirements listed are:

IAV3: no veto from chambers 312 or 322

IAV4: no veto from chambers 412 or 422

CC1: there is a track candidate in the central chamber pointing toward the TOF 700 bank

DELAY: replaces TIME of previous triggers; requires a delayed hit in the TOF 700 bank in reference to the T1T2 signal

TOF700DC: DC roads for positively charged particles using groups of 32 wires in chambers 100, 101, and 102

Only positively charged central particles were included in the DC roads due to the number of logic units required to implement these roads.

This trigger is the most restrictive of the triggers used, and the trigger rates were somewhat lower. The resulting data acquisition rates were on the order of 1 Hz. Thus, where the OR and AND data were taken

during only two ISR runs, the TOF data were taken over thirteen ISR runs. Along with the above TOF trigger, a small sample of events was recorded without the veto chamber requirement in order to help understand the effects of the intermediate angle veto.

2.4. Data Acquisition and Analysis

Once the trigger logic was satisfied, all the information on the event was read out from the detector and stored on magnetic tape. As mentioned above, only about fifty events per second could be written out to tape. These magnetic tapes were then copied and sent to the High Energy Physics group at Iowa State University for processing.

The Fast13 and Slow13 triggers were not completely efficient in selecting events that had one and only one fast proton in each forward telescope. Thus, to avoid using computer time unnecessarily by fully reconstructing events which did not meet the DPE trigger requirements, the data were first run through a filter process. The filter program reconstructed only forward tracks in the SFM. In order to pass the filter, the events were required to have one and only one positively charged particle with a momentum greater than 18 GeV in each forward telescope. These events were then passed on for full reconstruction.

The track recognition process in the SFM is based on a process developed by H. Wind [Wind 1974, Aubert and Broll 1974, Wind 1978]. The track candidates are found by what is termed a "WTRA". The WTRAs determine what possible combinations of chamber hits may form a valid track, and each region of the SFM is covered by one or more of these WTRAs.

After a valid track candidate is found, it is passed through a subroutine called SPLINE, which effectively performs a quintic spline fit to the measured points [Drijard 1976]. This procedure has the effect of refining the measurement of the momentum, position, and direction of the track. Once this is done the tracks are then extrapolated back to the interaction region to attempt to fit the tracks to a common vertex. If the chi-square of this fit is too large, the track with the largest contribution to the chi-square is dropped, and the fit is retried. This process is repeated until an acceptable vertex is found or until too few tracks are left to define a vertex.

After the vertex is found, it is used as an additional space point to look for other track candidates. Once this is done, all tracks that were not used to fit the vertex are checked to see if they are consistent with having originated from the vertex. Also, tracks that have $\Delta p/p$ greater than 0.30 are refitted with the vertex as one of the data points in order to improve the track parameters. Thus, one winds up with a vertex position, a list of vertex and non-vertex tracks, the momenta, charges, and all of the other detector information on these tracks (such as TOF and dE/dx), plus the errors on these quantities. This information is summarized and written out to a data summary tape (DST) to be used for further physics analysis.

2.5. Data Taking

The OR data were taken during December of 1981 (ISR run #1240), with a total of 1.6 million events recorded. Out of these events, 0.50 million

passed the filter stage (31%), and 492,977 of them were successfully processed and written out to a DST.

The AND data were taken during December of 1981 (ISR run #1240) and May of 1982 (ISR run #1270), with a total of 1.4 million events recorded. Out of these events, 0.42 million passed the filter stage (30%), and 406,356 of them were successfully processed and written out to a DST.

The TOF data were taken March through May of 1983 (ISR runs #1321, 1324-28, and 1335-41), with 1,651,486 events recorded with a delay of 32 ns, 32,239 events recorded with a delay of 34 ns, and 645,970 events recorded with a delay of 36 ns. Out of these events 257,251, 6,928, and 136,782, respectively, passed the filter stage (15.6%, 21.5%, and 21.2%), and 256,896, 6,922, and 134,642 were successfully processed and written out to a DST. Also, a total of 89,474 events were recorded without the intermediate angle veto and with a delay of 32 ns. Out of these events, 9,206 passed the filter stage (10.3%), and 9,202 of them were successfully processed and written out to a DST.

3. FOUR CONSTRAINT FIT OF DATA

3.1. Motivation for Kinematic Fit

A constrained kinematical fit adjusts the measured parameters of all the tracks in an event, according to their associated measurement errors, in order to balance energy and momentum. The end result of such a kinematical fit is a set of "improved" parameters and a "goodness-of-fit" parameter, e.g., χ^2, which gives some measure of how much the track parameters had to be adjusted in order to yield energy and momentum conservation. Also, one obtains what is termed a "pull" or "stretch" distribution for each track parameter, which is a measure of how much, relative to its errors, the parameter had to be changed in order to yield energy and momentum conservation. Such fits can effectively improve the resolution of the detector, discriminate between different hypotheses, and help to eliminate events that were incorrectly measured or had missing tracks.

In order to carry out this fitting process, the error of each track parameter must be known. If the errors are incorrectly determined, one will pull parameters either too much or too little, depending on which way the error is off. The procedure used is to calculate as many of the errors as possible and then to adjust the remaining errors in order to yield reasonable distributions for the pull quantities and χ^2 value of the fit.

A major problem with the SFM detector is to distinguish between events which contain no missing neutral particles and events in which some particles are undetected. The failure to detect some of the final state particles may be due to inefficiencies in the detection chambers and reconstruction codes or to neutral particles which cannot be detected if they do not decay quickly into charged states. This poses a particularly troublesome case for π^0 production, which usually represents about one-third of the ordinary pion production in an experiment. This means one-third of the produced pions are undetected by the SFM detector, which is a problem if one wishes to study completely measured events. One hopes that a kinematic fit of the data will eliminate a significant number of these incompletely measured events by rejecting those with missing particles.

3.2. Details of Kinematic Fitting

Kinematical fitting of the measured track parameters is a well-known technique with numerous references as to how to carry it out [Berge, Solmitz, and Taft 1961, Frodesen, Skjeggestad, and Tofte 1979]. It is usually a least squares fitting technique, based on the minimization of the quantity:

$$\chi^2 = (\mathbf{x} - \mathbf{x}^m)^T \mathbf{V}^{-1} (\mathbf{x} - \mathbf{x}^m)$$

where $\mathbf{x}^m$ is an n-component column matrix of the measured values of the track parameters (each track has three parameters associated with it to give the magnitude and direction of its momentum), $\mathbf{x}$ is an n-component column matrix of the adjusted track parameters, and $\mathbf{V}$ is the nxn covariance matrix for the measured track parameters (note that $\mathbf{V}$ is

symmetric). The fit adjusts values in x until the above quantity is minimized, and the final values in x are the improved parameters. This least squares procedure is often referred to as "chi-square minimization" due to the fact that if the parameters used to give the magnitude and direction of each track are normally distributed, then the χ^2 quantity defined above follows a chi-square probability distribution. The χ^2 quantity has n degrees of freedom, which are reduced by the number of independent constraints applied in the fit. With c external constraints on the fit variables (e.g., energy and momentum conservation), one has n-c independent least squares constraints, so the number of degrees of freedom is equal to n-(n-c) or c. This is what gives this fit process the name 0C fit, 1C fit, 2C fit, etc. In the case of the data considered here, all charged tracks were completely measured, so one could require the conservation of momentum (3 constraints) and of energy (1 constraint), and thus use the term four constraint (4C) fit.

3.2.1. Review of basic equations

For the general case of nonlinear constraints, the usual method to include the external constraints is by the method of Lagrange multipliers rather than by the elimination of some of the parameters. This has the advantages that one does not have to decide which parameters to eliminate and it also requires less computation. The constraint equations can be written as a column matrix f(x) with c rows, with Lagrange multipliers λ (also a c row column matrix). The equation to minimize in this case is:

$$\chi^2 = (x - x^m)^T V^{-1} (x - x^m) + 2 \lambda^T f(x)$$

Thus, the equations to be solved are:

$$\frac{\partial \chi^2}{\partial x} = 2V^{-1}(x-x^m) + 2F^T(x)\lambda = 0$$

$$\frac{\partial \chi^2}{\partial \lambda} = 2f(x) = 0$$

where $F(x) = (\partial/\partial x)f(x)$.

With nonlinear external constraints, the least-squares minimum must be found by an iterative procedure. The iterative procedure is defined by expanding the constraint equations around some approximate solution x^ν, where the superscript refers to the order of the iteration. This results in the iterative equations:

$$\lambda^{\nu+1} = [F(x^\nu)\ V\ F^T(x^\nu)]^{-1}\ [f(x^\nu) - F(x^\nu)\ (x^\nu - x^m)]$$

$$x^{\nu+1} = x^m - V\ F^T(x^\nu)\ \lambda^{\nu+1}$$

$$(\chi^2)^{\nu+1} = (\lambda^{\nu+1})^T\ [f(x^\nu) - F(x^\nu)(x^\nu - x^m)]$$

At the end of each iteration, the value of χ^2 is calculated and compared to the previous value. If it is smaller, the iterative process is continued. If it is larger, the minimum value has been overstepped, so the step is cut down by a factor of two until the χ^2 is decreasing again. This process is continued until some type of convergence criteria are met.

There are various criteria which can be used to terminate the iterative procedure in finding the minimum of the least-squares equation. In our case the requirement was that the χ^2 value converged. Specifically, that

$$\left| \frac{\chi^2_\nu - \chi^2_{\nu+1}}{\chi^2_{\nu+1}} \right| < \varepsilon$$

where ε was set equal to 0.0005 times the number of measured outgoing tracks.

If this criterion was not satisfied within a certain number of iterations, then the iterative procedure was abandoned. To insure that numerical problems were not the cause of a failure to converge, the matrix operations were performed in extended precision, which corresponded to about 15 digit precision on a VAX-11/785 computer.

3.2.2. Variables used for SFM data

The variables used to parametrize the measurements for kinematical fitting in the SFM are 1/p, λ, and ϕ of each track, where p is the magnitude of the momentum, λ is the angle out of the horizontal x-y plane of the SFM, and ϕ is the angle from the x-axis of the SFM (see Figure 2.4). The momentum and angle errors for each track are stored on the DST as the error on the momentum and direction cosines. Thus, the errors must be transformed to the fit variables. The entries in the derivative matrix J, for this transformation are:

$$k = \frac{1}{p} \qquad \lambda = \sin^{-1}(\cos\gamma)$$

$$\phi = \sin^{-1}(\cos\beta/\sin\gamma) = \sin^{-1}[\cos\beta/(1 - \cos^2\gamma)^{1/2}]$$

$$\frac{\partial\lambda}{\partial(\cos\gamma)} = [1 - \cos^2\gamma]^{-1/2} = [\cos^2\alpha + \cos^2\beta]^{-1/2} = p/p_{xy}$$

$$\frac{\partial\phi}{\partial(\cos\gamma)} = \cos\gamma\,\cos\beta[1 - \cos^2\beta/(1 - \cos^2\gamma)]^{-1/2}(1 - \cos^2\gamma)^{-3/2}$$

$$= \cos\gamma\,\cos\beta(1 - \cos^2\gamma)^{-1}(1 - \cos^2\gamma - \cos^2\beta)^{-1/2}$$

$$= \cos\gamma\,\cos\beta(1 - \cos^2\gamma)^{-1}(\cos\alpha)^{-1} = (pp_yp_z)/(p_{xy}^2p_x)$$

$$\frac{\partial\phi}{\partial(\cos\beta)} = (1 - \cos^2\gamma)^{-1/2}[1 - \cos^2\beta/(1 - \cos^2\gamma)]^{-1/2}$$

$$= (1 - \cos^2\gamma - \cos^2\beta)^{-1/2} = 1/\cos\alpha = p/p_x$$

$$\frac{\partial\lambda}{\partial(\cos\beta)} = 0 \qquad \frac{\partial\lambda}{\partial k} = 0 \qquad \frac{\partial\phi}{\partial k} = 0$$

$$\frac{\partial k}{\partial k} = 1 \qquad \frac{\partial k}{\partial(\cos\gamma)} = 0 \qquad \frac{\partial k}{\partial(\cos\beta)} = 0$$

where $\cos\alpha$, $\cos\beta$, and $\cos\gamma$ are the direction cosines from the SFM x, y, and z-axes, respectfully; p_x, p_y, and p_z are the track momenta in the x, y, and z directions; and p_{xy} is the track momentum in the horizontal plane. With the above derivatives, the error matrix is converted to the variables used in the kinematic fit by the transformation:

$$V(1/p,\lambda,\phi) = J^T V(1/p,\cos\beta,\cos\gamma)J$$

In terms of the fit variables, the external equations of constraint to require energy and momentum conservation are:

$$f_1 = \Sigma\, \eta_j E_j = \Sigma\, \eta_j (p_j^2 + m_j^2)^{1/2} = 0$$
$$f_2 = \Sigma\, \eta_j p_{xj} = \Sigma\, \eta_j p_j \cos(\lambda)_j \cos(\phi)_j = 0$$
$$f_3 = \Sigma\, \eta_j p_{yj} = \Sigma\, \eta_j p_j \cos(\lambda)_j \sin(\phi)_j = 0$$
$$f_4 = \Sigma\, \eta_j p_{zj} = \Sigma\, \eta_j p_j \sin(\lambda)_j = 0$$

where for the outgoing tracks $\eta = +1$ and for the incident beam protons $\eta = -1$.

It is assumed that there are no track-track correlations in this error matrix. This is reasonable since correlations between tracks arise, for example, during the fitting of several tracks to find a common vertex or by using a given vertex to find other tracks which may come from that vertex. Therefore, track-track correlations should be small compared to the actual measurement errors. Correlations between the track variables are usually not zero, so no additional assumptions about the error matrix are made.

3.2.3. Output results of fit

The output of the fitting routine consists of the "improved" track parameters (improved in the sense that they are now consistent with energy and momentum conservation), the errors on these parameters, the value of χ^2, and the value of the pull quantities for each parameter. The formulas for the fitted track parameters have been given above. The errors can be conveniently calculated at the end of the iterative process by using the equation:

$$\langle(\delta x^{\nu+1})(\delta x^{\nu+1})^T\rangle = V - VF^T(x^\nu)[F(x^\nu)VF^T(x^\nu)]^{-1}[VF^T(x^\nu)]^T$$

Note that this requires very little extra work since most of these quantities are used in the iterative fitting procedure.

The "pull" quantity for each parameter is a measure of how far, relative to the associated errors, the parameter had to be moved in order to satisfy the constraints of energy and momentum conservation. The quantities are defined as:

$$\text{PULL}(x) = \frac{(x^{fit} - x^m)}{\Delta(x^{fit} - x^m)_{rms}}$$

or in terms of quantities of the iterative procedure above:

$$\text{PULL}(x) = \frac{(x^{\nu+1} - x^m)}{|\langle(\delta x^{\nu+1})(\delta x^{\nu+1})^T\rangle - \langle(\delta x^m)(\delta x^m)^T\rangle|^{1/2}}$$

$$= \frac{(x^{\nu+1} - x^m)}{|\{V - V\,F^T(x^\nu)[F(x^\nu)\;V\;F^T(x^\nu)]^{-1}[V\;F^T(x^\nu)]^T\} - V|^{1/2}}$$

$$= \frac{(x^{\nu+1} - x^m)}{|\;V\;F^T(x^\nu)[F(x^\nu)\;V\;F^T(x^\nu)]^{-1}[V\;F^T(x^\nu)]^T\;|^{1/2}}$$

If the measured track parameters are normally distributed around their

true values, then these pull quantities are normally distributed. Furthermore, if the errors have been determined correctly, then the pulls have standard deviations equal to unity. These criteria may be used to investigate the correctness of certain assumptions made in calculating the a priori errors on the track parameters.

3.3. Determination of Beam Parameters

While the errors of the track parameters are calculated in the SFM track analysis, the beam parameters must be input to the fitting program. It is important to determine these values as accurately and as precisely as possible in order to benefit maximally from the fitting procedure. In order to do this, one must understand the characteristics of the beams at the I4 intersect of the ISR.

3.3.1. Beam momenta parameters

One important characteristic of the beams in the ISR is that they have a momentum spread of about ±3%, which is a large error if only the central value of the beam momenta is used as an input for the fitting process. However, we can use the known correlation between the beam momentum and the horizontal position of the beam particles to determine the beam momentum to a greater accuracy on an event-by-event basis. For each event, the momentum of the beam protons can be calculated from the vertex position using:

$$\frac{\Delta p}{p} = \frac{\Delta x}{\alpha_p}$$

where Δp[GeV] is the shift in momentum from the value at the center of the beam p[GeV], Δx[meters] is the distance from the center of the beam, and α_p[meters] is the momentum compaction function [Hubner 1977]. The value of α_p is typically about 2 meters in the ISR, and the total width of each of the two beams is about 0.06 meters.

For each ISR run, the value of α_p for each beam is calculated from the momentum bite of the beams given on the ISR Data Sheets that record run conditions. Specifically, the beam momenta on the ISR Data Sheets are given at the "top" and "bottom" of each beam, with these positions defined as the first measurement points where the beam current density drops below 10% of the maximum current density [Bryant 1985]. The measurements were done in 0.25 mm steps for the ISR Data Sheets. However, in finding the beam edges from the beam profiles determined by the reconstructed vertices in the SFM, steps of 1.00 mm were used. Once the beam edges are found from the beam profiles in the SFM, the momentum compaction is set to give the same momentum bite as given on the ISR Data Sheets. The equation used to determine α_p once the edges are determined is:

$$\alpha_p = \frac{1}{(p^t/p^b - 1)} (\Delta x^t - \Delta x^b p^t/p^b)$$

where the superscripts refer to the top and bottom of the beam, Δx is the distance from the center of the beam (note that Δx^b is negative), and p is the momentum taken from the ISR Data Sheets. Once α_p is found, one can find the momentum at the center of the beam p_o, by the equation:

$$p_o = \frac{p^t}{1 + \Delta x^t/\alpha_p}$$

The errors for these two quantities are (ignoring the error on the momenta of the top and bottom of the beams from the ISR Data Sheets):

$$\sigma^2_{\alpha_p} = \frac{1}{(p^t/p^b - 1)^2} \left[\sigma^2_{(\Delta x^t)} + \sigma^2_{(\Delta x^b)} (p^t/p^b)^2\right]$$

$$\sigma^2_{p_o} = \frac{p_o^2}{\alpha_p^2 (1 + \Delta x^t/\alpha_p)^2} \left[\sigma^2_{(\Delta x^t)} + (\sigma_{\alpha_p} \Delta x^t/\alpha_p)^2\right]$$

The errors calculated above were consistent from run to run, so the same values for these errors were used for all ISR runs in the 4C fitting program.

3.3.2. Beam horizontal crossing angle parameters

The beams cross in the horizontal plane at a nonzero angle as previously noted in the section which introduces the ISR. These angles are taken from a SFM Internal Note [Bryant 1973]. The errors on these values due to measurement errors and changes to the ISR and SFM setup since the measurements were taken are estimated to be about 1 part in a 1000 [Bryant 1985]. Since the momentum varies from the nominal value of 31.460 GeV for different ISR runs, the actual crossing angle used in the fitting procedure is interpolated from these values with a quadratic equation. The parameters are determined from the crossing angles at 31, 26, and 22 GeV in a 1 Tesla field. The resulting equation is:

$$\alpha[\text{degrees}] = 0.00456746p^2 - 0.366528p + 24.4874$$

where p is the momentum of the beam at its center. The angles in terms of the fit variable ϕ are:

$$\phi_{\text{beam1}} = +(\pi + \alpha_1[\text{rad}])/2$$

$$\phi_{beam2} = -(\pi + \alpha_2[\text{rad}])/2$$

Due to the optics of the ISR, there is an additional correction to the angle of a beam proton. This is given as:

$$\Delta\phi[\text{rad}] = D'_x \frac{\Delta p}{p} = D'_x \frac{\Delta x}{\alpha_p}$$

where D'_x is a parameter of the ISR. For all data, the value of 0.03 ±0.01m is used for each beam [Bryant 1985]. This value comes from the I4 beam parameters for the ISR being operated in their low beta mode.

3.3.3. Beam vertical crossing angle parameters

After the initial 4C fitting of the data, it was noticed that the vertical crossing angle of the beams could be correlated to the z (vertical) vertex position. This was parametrized empirically for the OR data by:

$$\lambda_{beam} = (z_o - z)D'_z + \lambda_o$$

where z_o is the average z vertex position, λ_o is the crossing angle at $z = z_o$, and D'_z is a parameter that was determined empirically from the data.

The procedure used to determine D'_z was to fit events using different values of D'_z and then study the mean of the pull distributions as a function of the z vertex position. Specifically, the pulls were plotted for z vertex positions in the top and bottom (vertically) of the beams, and the mean values of these pull distributions were plotted as a function of D'_z. The value of $0.7\text{x}10^{-4}$ was chosen on the basis of these distributions and was checked for consistency with other ISR runs and each DPE trigger. The error on λ_{beam} used was (neglecting the error on z_o):

$$\sigma_\lambda^2 = \sigma_z^2 D_z'^2 + \sigma_{D_z'}^2 (z_o - z)^2 + \sigma_{\lambda_o}^2$$

The above equation, coupled with the similar equation for the horizontal crossing angle, makes sense optically for the beam. What these two equations describe is a beam that is being defocused in the horizontal plane and focused in the vertical plane. This is what one wants, since the luminosity of the ISR depend on the height of the beams but not on their width (this is because the beams cross in the horizontal plane).

3.4. Outgoing Track Parameters

As mentioned previously, the standard SFM production chain calculates the track parameters and their respective covariance matrices. A detailed study of the calculated errors is complicated due to the way tracks are found in the SFM detector and to the fact that the SFM detector uses MWPCs with different wire spacings. After careful study it was demonstrated that these measured parameters were consistent within their respective errors and that their errors were correct as far as could be determined. There were a few adjustments made to the measured parameters before inputing them to the kinematical fit. These adjustments will be discussed below, as well as the reasons for deciding why to make them.

3.4.1. Correction for multiple scattering

Using only the errors on track parameters due to track reconstruction (e.g., position errors of chambers, number of wire hits and their

accuracy, etc.) results in the calculated errors for the λ angles of the fast outgoing protons being too small. This is due to the fact that the actual charged particles multiple scatter when passing through material in the detector. For the fast outgoing protons in each telescope, this multiple scattering is dominated by the beam pipe. This was corrected by adding to the track λ angle errors of the fast protons an additional error due to multiple scattering:

$$\sigma^2_{ms} = \frac{(4.41\text{x}10^{-4})\ E^2 r}{p^4} \simeq \frac{(4.41\text{x}10^{-4})\ r}{p^2}$$

where r is the number of radiation lengths of material the protons pass through in the detector, and p is the momentum of the track [GeV]. The given approximation is valid since the leading protons are all at high momenta. Elastically scattered protons go through about 0.3 radiation lengths of material, so this was used to approximate r for the leading protons [Breakstone 1984].

3.4.2. Other leading proton parameters

The idea of adjusting p and ϕ of the leading protons to account for the nonzero mean values of the pull distributions, caused by systematic errors, was considered and dismissed. This was decided for a number of reasons. A major source of skewness in the pulls could come from events which actually had missing tracks, but still yielded a reasonable χ^2 value. This hypothesis is consistent with the signs of the mean values of the pull quantities in 1/p and ϕ. On the average, events with missing tracks would require increasing the momenta of the leading outgoing

protons and decreasing the momenta of the incident beam protons, while changing the ϕ angle of both leading and beam protons to decrease their longitudinal momenta in order to satisfy the constraints of energy and momentum conservation. Thus, it was decided that only if one had unambiguous evidence of a systematic error would such a correction be attempted. This criterion was never satisfied for the leading proton parameters.

Another problem with using the pull quantities to adjust the track parameters of the leading protons is that some of the basic assumptions about the distribution of the measurements are not completely valid. Specifically, the measurements made by MWPCs are not usually normally distributed. They are close enough so that the χ^2 for the 4C fit can be approximately interpreted as a chi-square probability distribution, but care should be exercised in interpreting the mean values and widths of the pull quantities. For example, when studying the widths of the pull quantities one does not want to include events which are inconsistent with the fit hypothesis (e.g., events with missing tracks). This requires making a cut on χ^2 to eliminate most of these events. However, once this is done the interpretation of the widths of the pull quantities becomes more difficult in that one no longer expects normal distributions with unit widths. The widths of the pull quantity distributions in general may depend strongly on just where one decides to cut in χ^2.

Thus, in order to use the pull quantity distributions to make adjustments in the track parameters input to the fit, it was required that they all give consistent indications of a needed adjustment. An example of this was mentioned above in the parametrization of the vertical

crossing angle of the beam as a function of vertical vertex position. It was decided that the primary goal was to make the χ^2 distribution look correct at lower values (i.e., a flat distribution in the probability-of-fit for higher probabilities) rather than to get all the pull quantities to have a width of unity. Such deviations from unity are largely the result of a general misestimate (usually an underestimate) of the true errors in the track parameters input to the fit. Thus, the beam errors were adjusted to get roughly equal widths of the pull quantity distributions after a probability-of-fit cut at 0.10. All these considerations lead one to exercise caution when interpreting data from MWPC detectors in terms which were developed for ideal circumstances or for another type of measuring device, e.g., a bubble chamber.

3.4.3. Central track parameters

The only correction made to the parameters of the central tracks were energy loss corrections that were determined previously for the SFM detector. These corrections apply only for low momentum tracks and account for the average energy a particle of a particular mass loses in going through the central region of the detector. The energy loss was paramatrized by a quadratic equation in terms of the measured momentum:

$$p_{cor} = p_{meas} + A + B/p_{meas} + C/p_{meas}^2$$

Table 3.1 gives the values for A, B, and C for pions, kaons, and protons. The correction was only applied for a certain range of momenta. The range was between p_{low} and p_{high}, also given in Table 3.1. The lower cut is based on calculations that particles below these momenta will not be

detected. The upper cut is based on the fact that the energy loss becomes negligible at higher momenta.

Table 3.1. Energy loss correction parameters

Particle	A	B	C	p_{low}[GeV]	p_{high}[GeV]
pion	0.0016	0.00132	0.00007185	0.075	0.625
kaon	-0.012	0.01268	0.0003442	0.125	1.00
proton	-0.029	0.03341	0.001685	0.225	1.00

In all the 4C fits done, the central tracks were well behaved once the beam λ distribution was put in empirically. This is very reassuring, since the central tracks are by far the most important part of each event. Even if the problems mentioned in Section 3.4.2 about using the pull distributions are ignored, one sees no real evidence for any systematic errors in the measurement of the central track parameters.

3.4.4. Mass hypotheses used for 4-prong events

For the 4-prong events there are two central particles, which due to conservation of various quantum numbers such as baryon number, charge, isospin, etc. must be the antiparticles of each other. This requires the central particle pair to be $\pi^+\pi^-$, K^+K^-, or $p\bar{p}$. The fitting was done for each of these mass hypotheses separately, since mass identification in the

SFM detector is limited. The fit results were later used to help accept or reject a particular mass hypothesis. Each of these three hypotheses differs from the others only in the mass assignments of the central particle-antiparticle pair, and hence the only difference occurs in the energy conservation constraint.

3.4.5. Mass hypotheses used for 6-prong events

In the case of 6-prong events there are four central particles. Thus, for strong decays of the central system there are a total of fifteen different mass combinations to try when fitting the data. This is a rather large number of fits to perform, and even more difficult to handle when it comes to doing the physics analysis of the events. Since most of the central particles are pions for the AND and OR data, it was decided to try to identify one of the four particles in the central system to reduce the number of fits attempted. For the TOF data, it was decided that the safest route was to do all fifteen fits and decide at a later point in the analysis as to which mass combinations to study. This was necessary because of the enrichment of kaons and protons in the TOF data sample.

If one particle can be clearly identified, then only five fits are required. If the mass identification is ambiguous between π/K or K/p, then nine fits are required. The hypothesis that all the central particles were pions was tried in every case, regardless of any particle identification. This was important since for the OR and AND data almost all central particles were pions. If no particle identification could be done, then the 4-pion hypothesis was the only one tried for the AND and OR data.

To perform the mass identification when fitting the AND and OR data, the TOF system of the SFM was used. When more than one particle was identified by the TOF, the most reliable identification was taken. The identification scheme used was to perform a test on the number of standard deviations the mass squared (M^2) as calculated by the TOF system was from the M^2 value of the three possible particles (π, K, or p). The only error used was the error on the TOF M^2 measurement itself. For an identification to be labelled unique, the TOF M^2 was required to be closer to one hypothesis than to the other two and to be at least three standard deviations away from the other two hypotheses. If the particle identification was not unique, then the other categories were π/K ambiguous and K/p ambiguous (π/K/p ambiguous is equivalent to no identification). For the π/K case, the M^2 was required to be closer to the kaon than to the proton and to be at least three standard deviations away from the proton. The same type requirement was used for the K/p case. The ambiguous cases were considered equivalent to no information for the AND and OR data since they represented such a small fraction of the data and were not used.

3.5. Summary of Beam Parameters Used for Each ISR Run

Table 3.2 summarizes the beam parameters used for each ISR Run. In this table $\bar{x}$, $\bar{y}$, and $\bar{z}$ are the average vertex positions of the data recorded during each ISR run. The same values for errors on the beam angle errors and $\Delta p/p$ were used for all fits. The values used were 0.002 for $\Delta p/p$, 1.0×10^{-8} for σ^2_λ, and 4.0×10^{-7} for σ^2_ϕ.

Table 3.2. Beam parameters for the 4C-fit

ISR Run	$\bar{x}$[cm]	$\bar{y}$[cm]	$\bar{z}$[cm]	α_{p1}[m]	α_{p2}[m]	p_1[GeV]	p_2[GeV]
1240	-2.70	+4.20	-0.28	1.70	2.54	31.41	31.37
1270	-2.77	+2.50	-0.07	1.90	2.52	31.44	31.36
1321	-3.04	+2.75	-0.26	2.17	2.58	31.39	31.34
1324	-3.13	+0.32	-0.20	2.37	2.56	31.42	31.36
1325	-2.78	+1.23	-0.07	2.32	2.62	31.44	30.72
1326	-3.01	+1.24	-0.19	2.29	2.61	31.44	31.36
1327	-2.74	+0.89	-0.14	2.31	2.36	31.50	31.37
1328	-3.16	+0.43	-0.17	2.34	2.61	31.38	31.36
1335	-2.89	+0.07	-0.11	2.29	2.58	31.41	31.40
1336	-3.03	-0.23	+0.01	2.22	2.71	31.40	31.39
1337	-2.78	-0.24	-0.08	2.25	2.63	31.40	31.41
1338	-2.92	+1.52	-0.16	2.20	2.50	31.46	31.35
1339	-3.37	+1.14	-0.26	2.15	2.43	31.37	31.35
1340	-3.08	+0.73	-0.19	2.15	2.42	31.43	31.42
1341	-2.96	+1.50	-0.18	2.36	2.47	31.46	31.37

4. FOUR PRONG "OR" DATA ANALYSIS

4.1. Final Cuts on Data

Of the 492,977 events taken with the OR trigger which were successfully processed and stored on a DST, 83,367 of them were events with four outgoing tracks where all four tracks were found to come from a common vertex. The requirement of one and only one outgoing fast positively charged particle in each forward telescope was again made on the fully reconstructed events, and each fast forward particle was required to have a Feynman x (x_F) greater than 0.55 and less than 1.8. The lower value was chosen to remain consistent with the 18 GeV cut on the protons' momenta in the filter processing, and the higher cut was chosen to remove very badly measured events. This cut reduced the number of events to 80,980. Those events remaining were then required to maintain charge balance (i.e., the two central tracks were required to have opposite charge). This cut further reduced the number of events to 67,410. These events were then subjected to the 4C-fit procedure described in Chapter 3.

As explained in Chapter 3, the main purposes of the 4C-fitting procedure were to reject events with missing or badly measured tracks and at the same time effectively improve upon the measured track parameters. Thus, events which failed to match the hypothesis of energy and momentum conservation were rejected on the basis of an unacceptable χ^2 value. After studying the chi-square and probability-of-fit distributions, a cut at a probability-of-fit value of 0.05 was chosen (Figure 4.1). This means that one would be throwing away 5% of the good events if all the errors

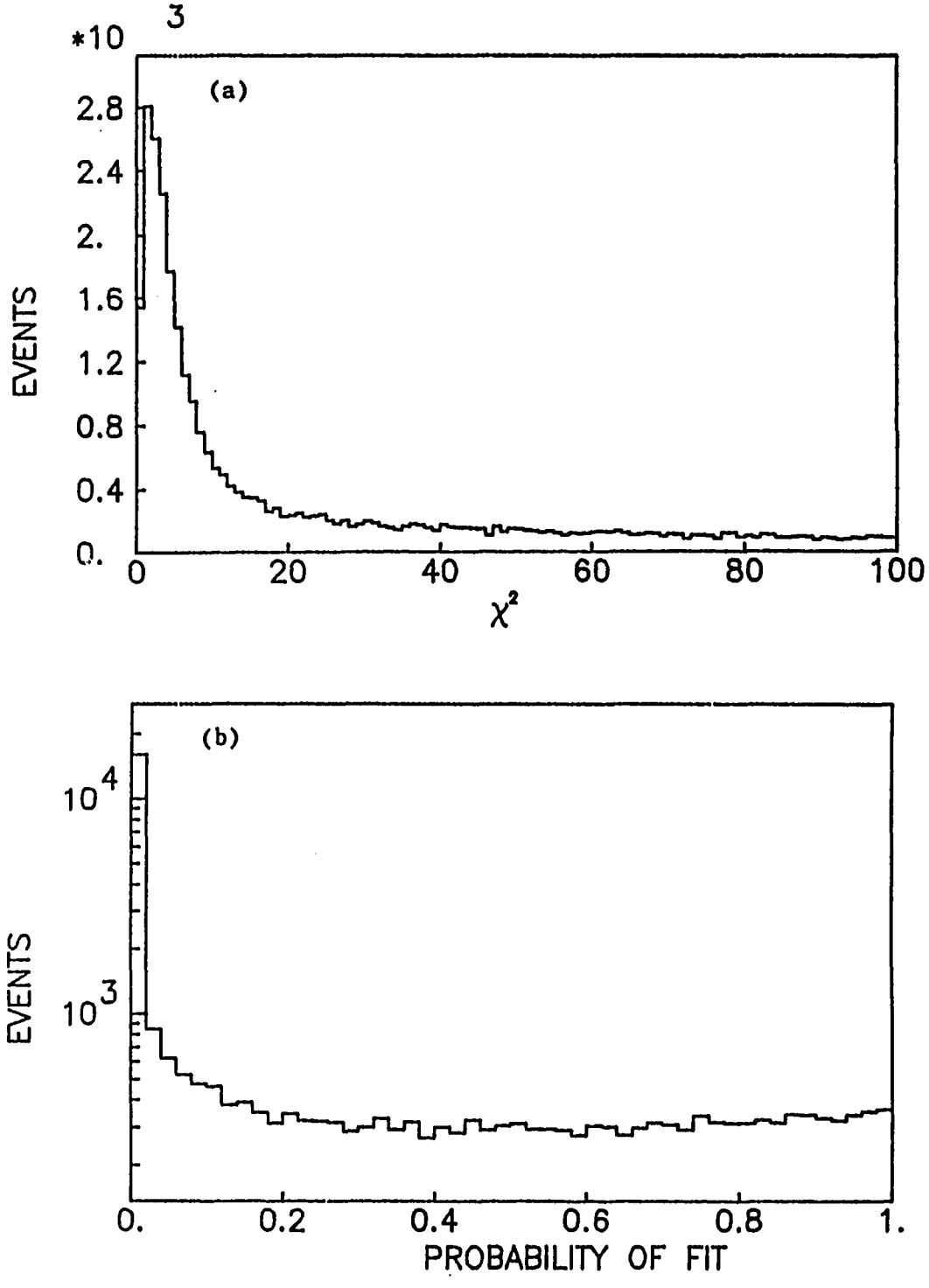

Figure 4.1. Distributions of (a) the χ^2 values and (b) the probability-of-fit values from the 4C-fit of the four prong OR data

were correctly determined.

To give further confidence that this cut was both reasonable and effective, the mass distribution was studied in probability-of-fit divisions of 0.01 around the chosen cut of 0.05. There is a clear change in the mass distribution with the cut between 0.04 and 0.05 where the mass distribution becomes dominated by incompletely measured events (i.e., events with missing tracks). Thus, below a probability-of-fit value of 0.05, contamination from events that do not satisfy energy and momentum conservation increases significantly as indicated by the probability-of-fit distribution. The mass distributions of the central $\pi^+\pi^-$ pairs are shown in Figure 4.2 for events with probability-of-fit values greater than 0.05 (Figure 4.2(a)) and less than 0.05 (Figure 4.2(b)). For Figure 4.2(b), only events which had $\chi^2 < 100$ were included (recall that this chi-square distribution has four degrees of freedom). Since the distribution changes drastically (i.e., the peak of the distribution shifts and the enhancement around the region of 1200 MeV disappears), this cut appears consistent with what is expected if it is separating real four track events from events which have missing tracks. Figure 4.2 shows that the effort spent on refining the parameters used in the 4C-fit was very valuable when measured by the amount of background rejected from the data.

In addition to the cut on the probability-of-fit value, a cut was also placed on the x_F values calculated from the fitted track parameters for the leading protons. Figure 4.3 shows the x_F distribution of the four outgoing tracks calculated using the fitted variables. The two small double peaks in the x_F regions around -0.5 and +0.5 are consistent with particles coming from single diffraction. From this one can see that the

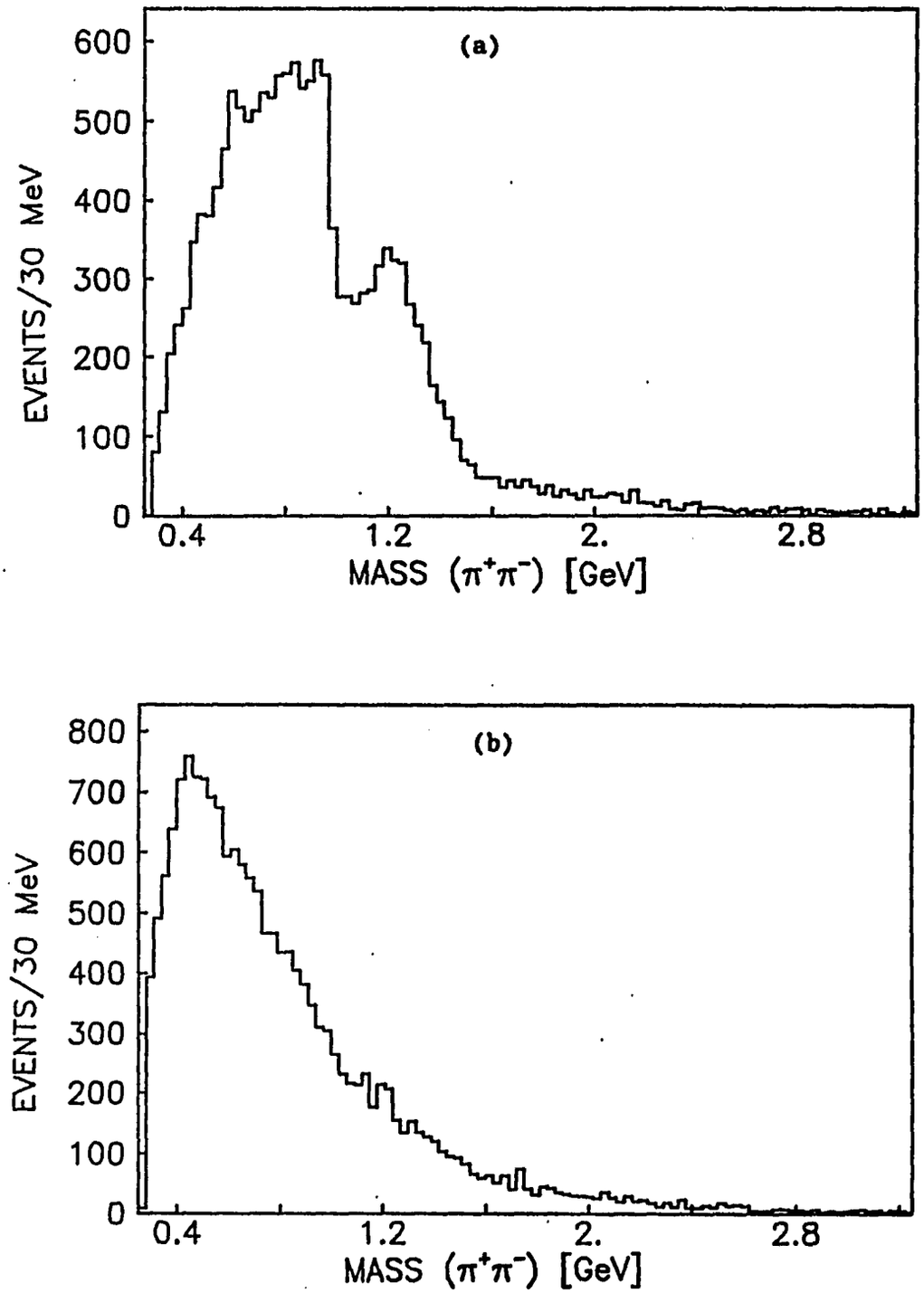

Figure 4.2. $\pi^+\pi^-$ mass distribution for (a) probability-of-fit values greater than 0.05 and (b) less than 0.05

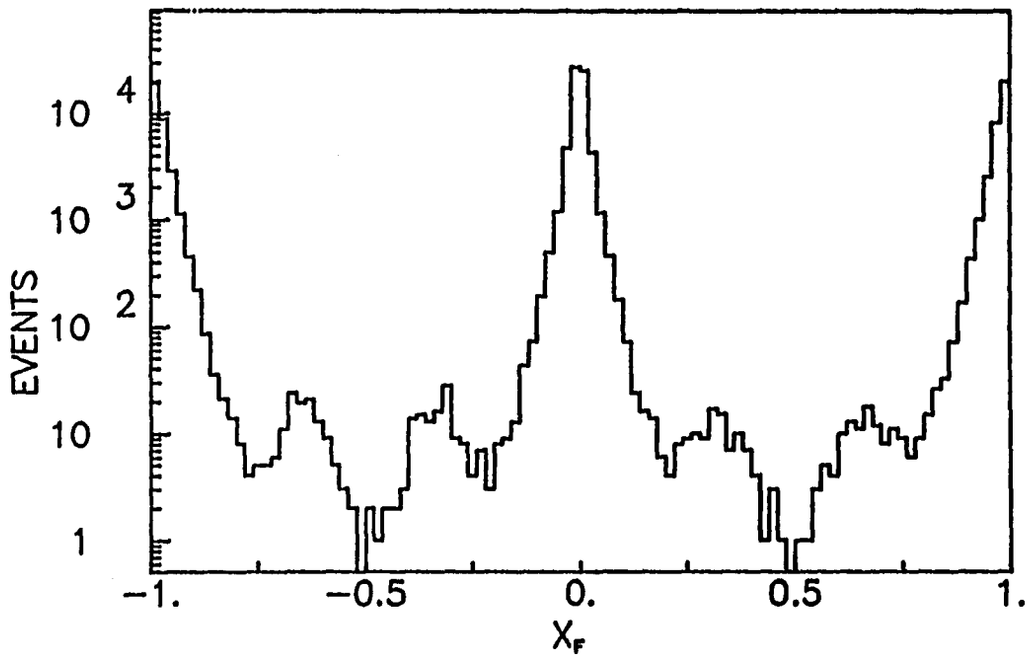

Figure 4.3. Feynman x distribution for outgoing tracks

single diffraction contribution to the data is very small (i.e., less than 1%) and can be nearly eliminated with the cut $x_F > 0.8$ for the leading protons.

Since there were very few events with K^+K^- or $p\bar{p}$ pairs in the central system, these events were treated as contamination of the data. The time-of-flight system of the SFM detector was used to reject the events which had any of the central particles identified as a kaon or proton, i.e., where this identification was inconsistent with a pion identification. The TOF mass squared (M^2) distribution for those central tracks, where this information exists, is shown in Figure 4.4(a). From this plot one can see that the vast majority of the data do indeed have the central system consisting of two pions. To see that some separation of pions from kaons or protons is possible, a log plot of the TOF M^2 with the momenta of the tracks required to be less than 0.6 GeV is shown in Figure 4.4(b).

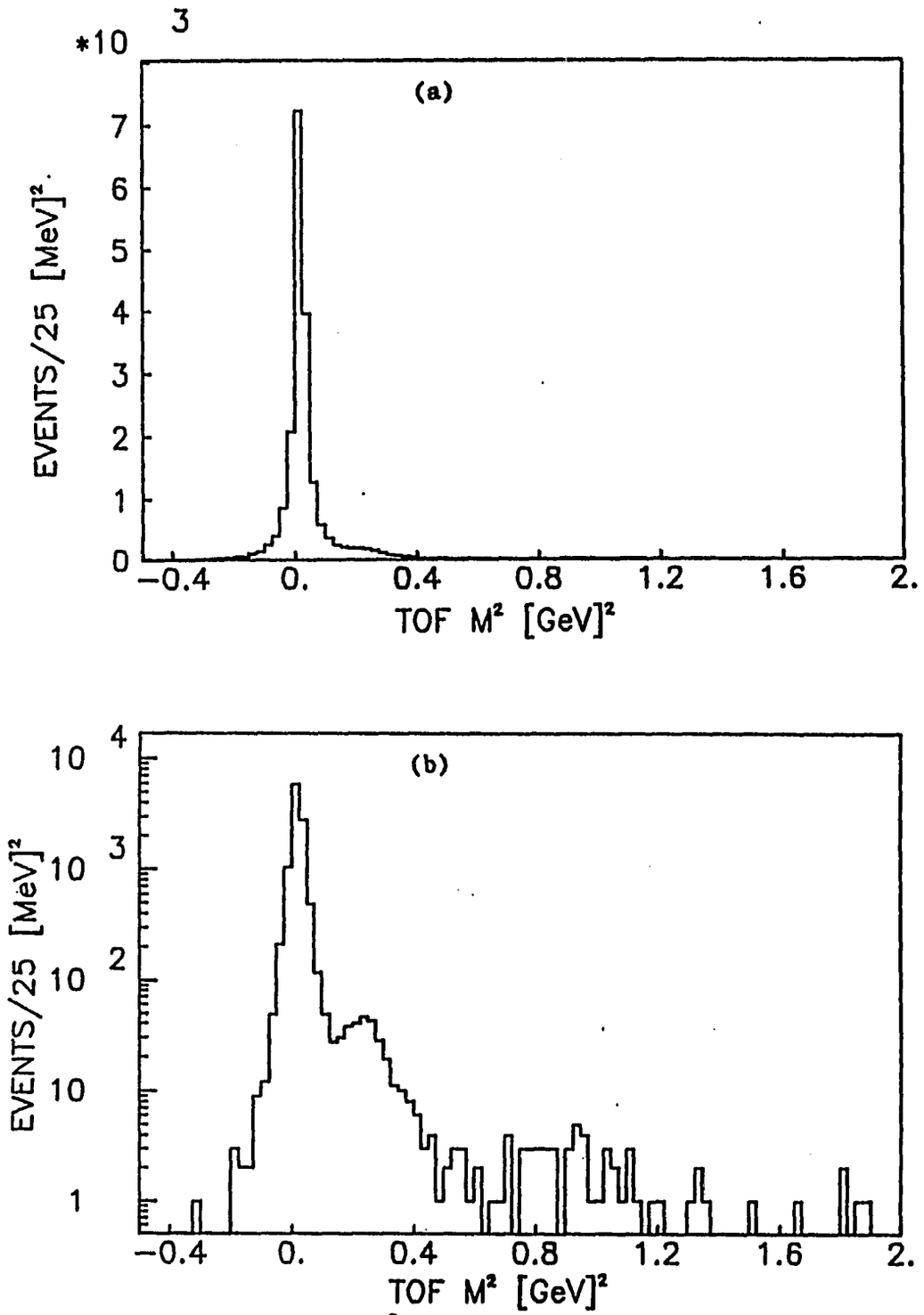

Figure 4.4. Time-of-flight M^2 distribution (a) for all momenta and (b) for track momenta less than 0.6 GeV (log plot)

Events were discarded if the measured TOF M^2 value was closer to the value for the kaon or proton M^2 than to the value for the pion M^2 and was at least 5 standard deviations away from the pion value (M_π^2 = 0.01948 GeV^2, M_K^2 = 0.2437 GeV^2, M_p^2 = 0.8804 GeV^2). This cut reduced the data sample by 440 events.

To show the effect of the 4C-fit on the mass distribution of the central $\pi^+\pi^-$ pairs, the mass distributions using the unfitted and fitted track parameters are shown in Figure 4.5. Table 4.1 shows how the average error on the mass of the $\pi^+\pi^-$ pair has improved for different ranges of the mass value. As expected, one can see that the 4C-fit has considerably improved the track parameters. On the basis of the studies of the probability-of-fit values and the mass distributions, the fit has also drastically reduced the number of events with missing tracks.

After all of the described cuts were performed, a total of 15,461 events remained in the four prong OR data sample. In Figure 4.5(b) we see

Table 4.1. Error on mass of $\pi^+\pi^-$ system

Mass($\pi^+\pi^-$) [GeV]	Unfitted Error [GeV]	Fitted Error [GeV]
M<0.5	0.049	0.012
0.5<M<1.0	0.122	0.024
1.0<M<1.5	0.159	0.037
1.5<M<2.0	0.211	0.047
M>2.0	0.279	0.063

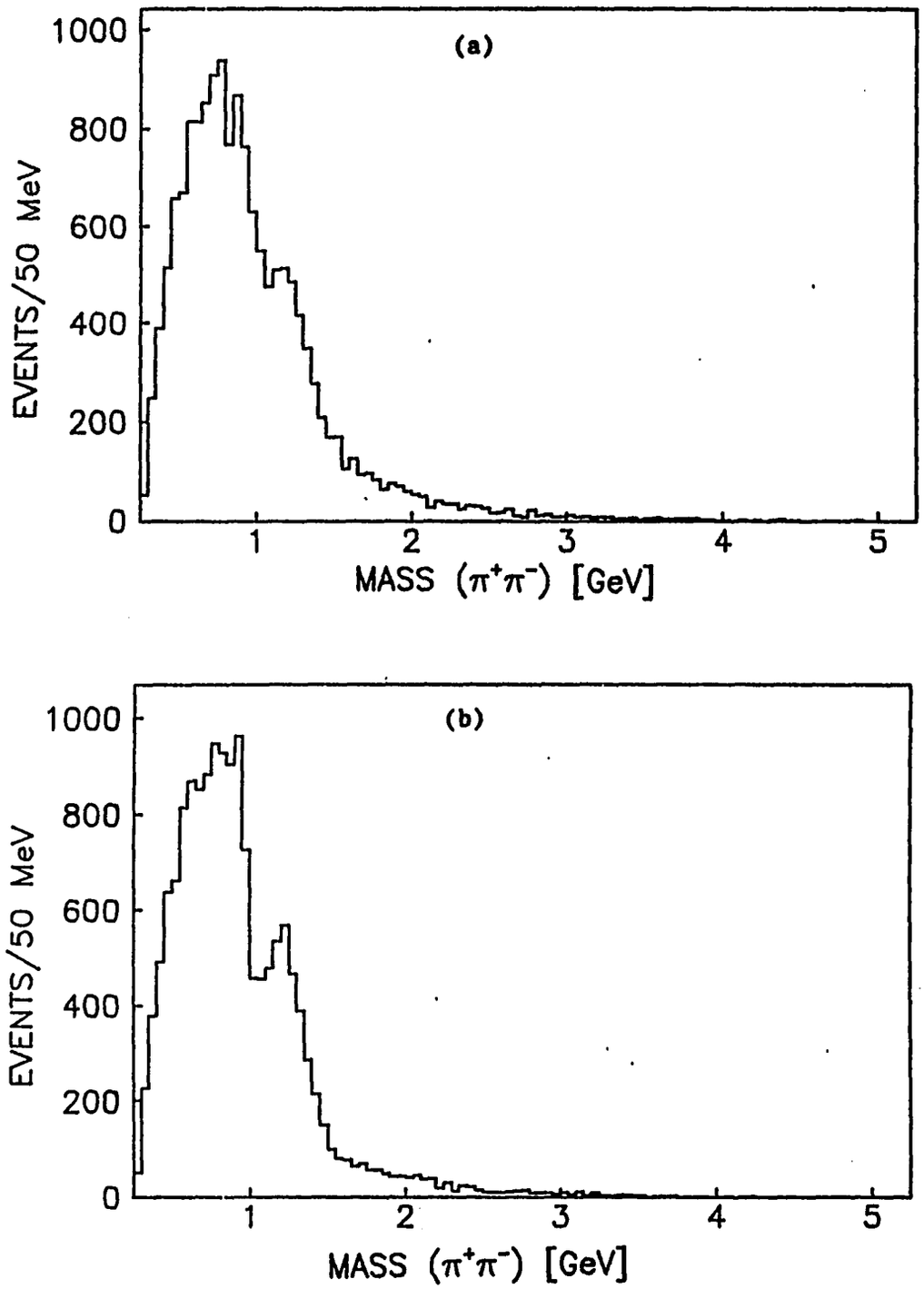

Figure 4.5. $\pi^+\pi^-$ mass distribution using (a) measured (unfitted) track parameters and (b) fitted track parameters

no evidence for a signal for the ρ^0 meson (m = 770 MeV, $J^{PC} = 1^{--}$) in the $\pi^+\pi^-$ mass distribution, while there is a strong enhancement in the region of the f^0 meson (m = 1274 MeV, $J^{PC} = 2^{++}$). As explained in Chapter 1, this is a powerful argument that we have in fact isolated a sample of DPE events by the use of this trigger. One can also see that the DPE trigger limits the data to low mass values for the central $\pi^+\pi^-$ system.

Figure 4.6 shows x_F of one outgoing leading proton versus x_F of the other outgoing leading proton. This plot shows the double-pole distribution as expected for DPE (see Section 1.2.1). Also, this plot shows that the bulk of the data have x_F of each of the fast leading protons greater than 0.92, since 95.8% (14,811 events) of the events appear in this plot.

Figure 4.7 shows the azimuthal angle around the beam pipe of one fast leading proton versus the azimuthal angle of the other fast leading proton. The structure in this plot is dominated by the geometric acceptance of the detector. For example, the gaps around 180^o were caused by the fact that chamber 415 was broken during the ISR runs when this data was recorded, so that no protons with $p_y > 0$ in the region of 180^o could be detected (note that this chamber is needed for the R1 trigger discussed in Section 2.3.1). Thus, this angle is not very useful to check for a lack of correlations between the two fast outgoing protons as predicted for DPE.

Figure 4.8 shows the momentum transfer t, of one fast leading proton versus that of the other. This plot shows no obvious correlation between the t values, and it also illustrates the rapidly decreasing distributions with increasing momentum transfer.

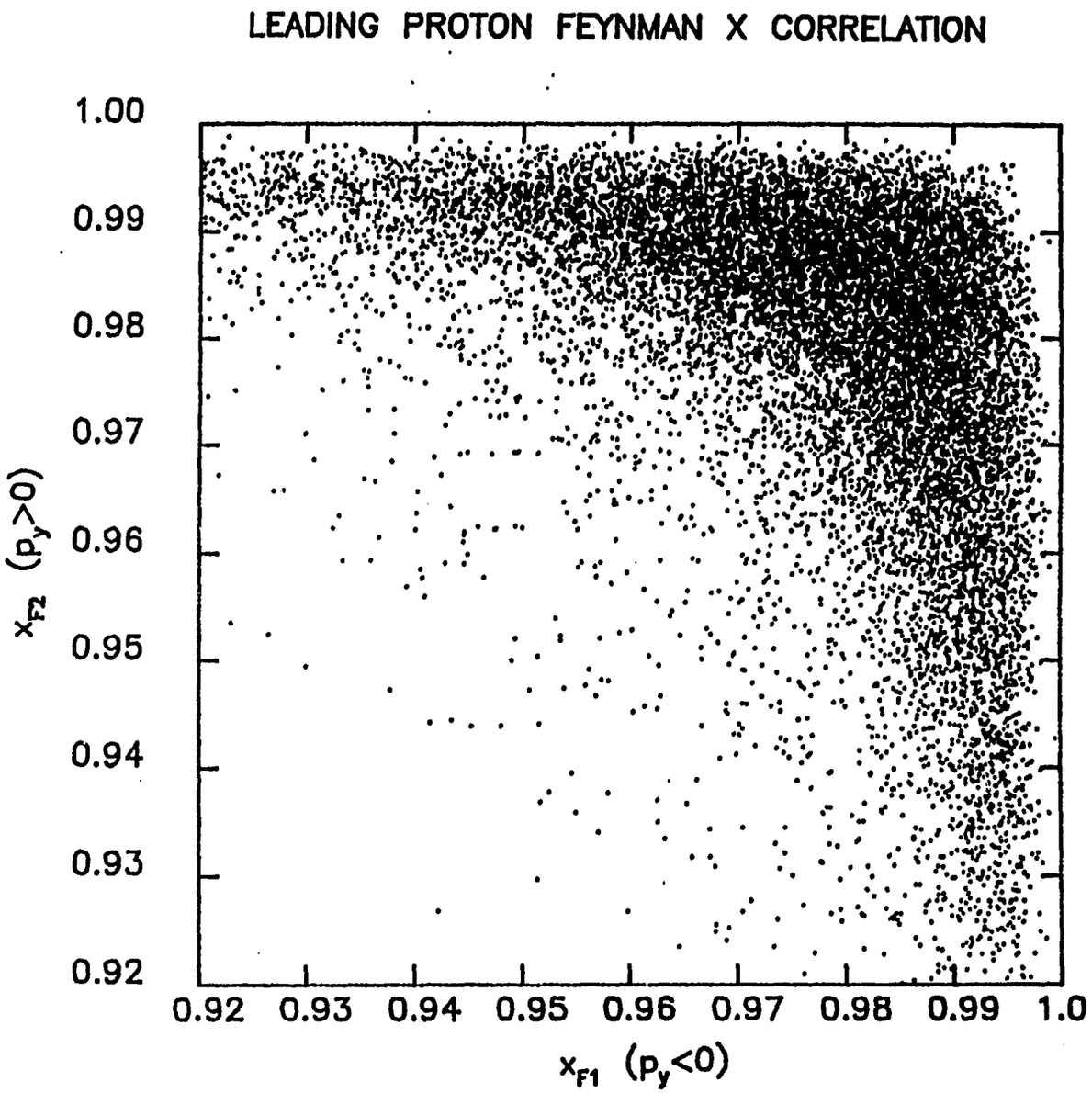

Figure 4.6. Scatterplot showing the correlation of x_F of one fast leading proton with x_F of the other fast leading proton

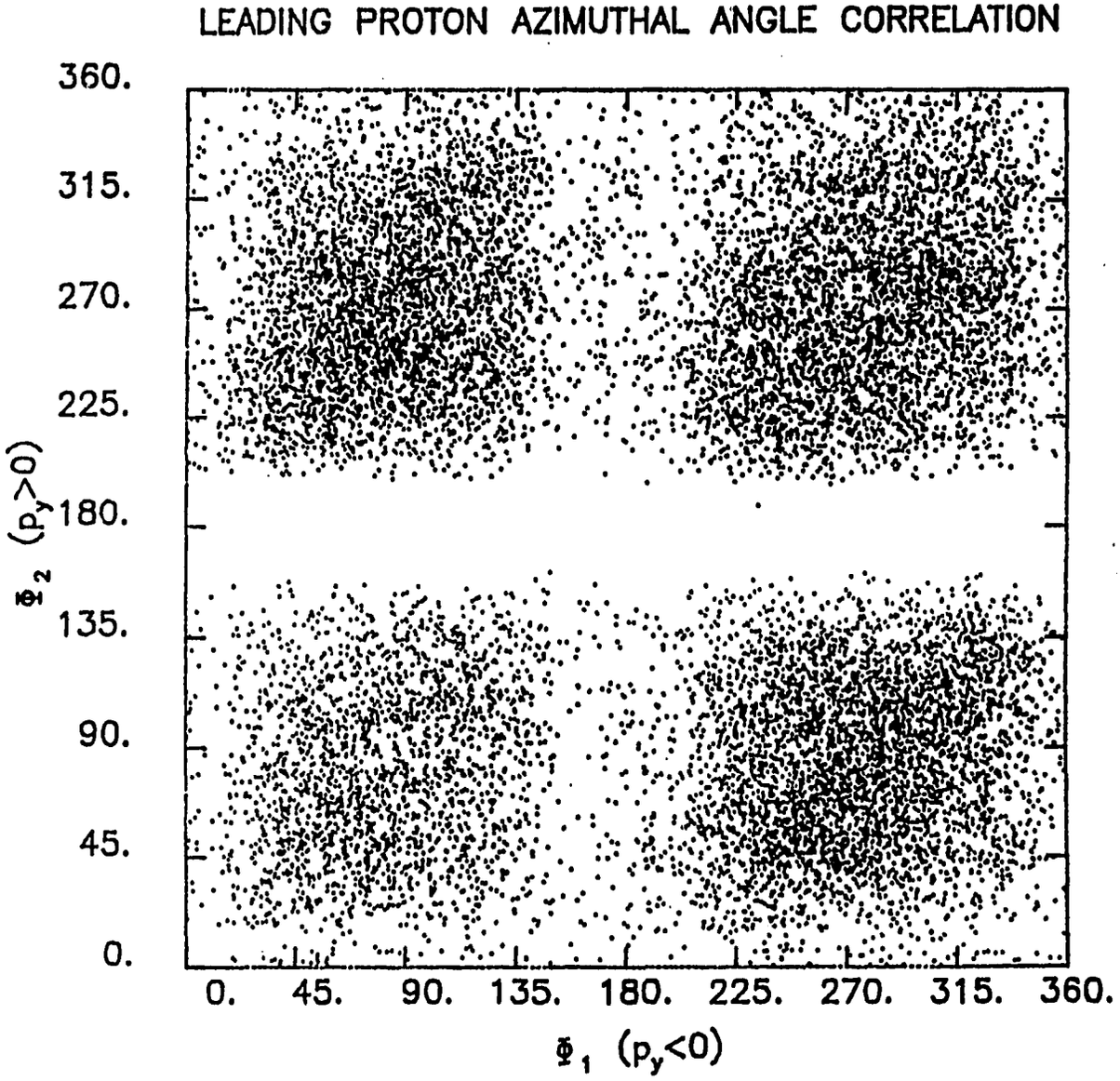

Figure 4.7. Scatterplot showing the correlation of the azimuthal angle of the two fast leading protons

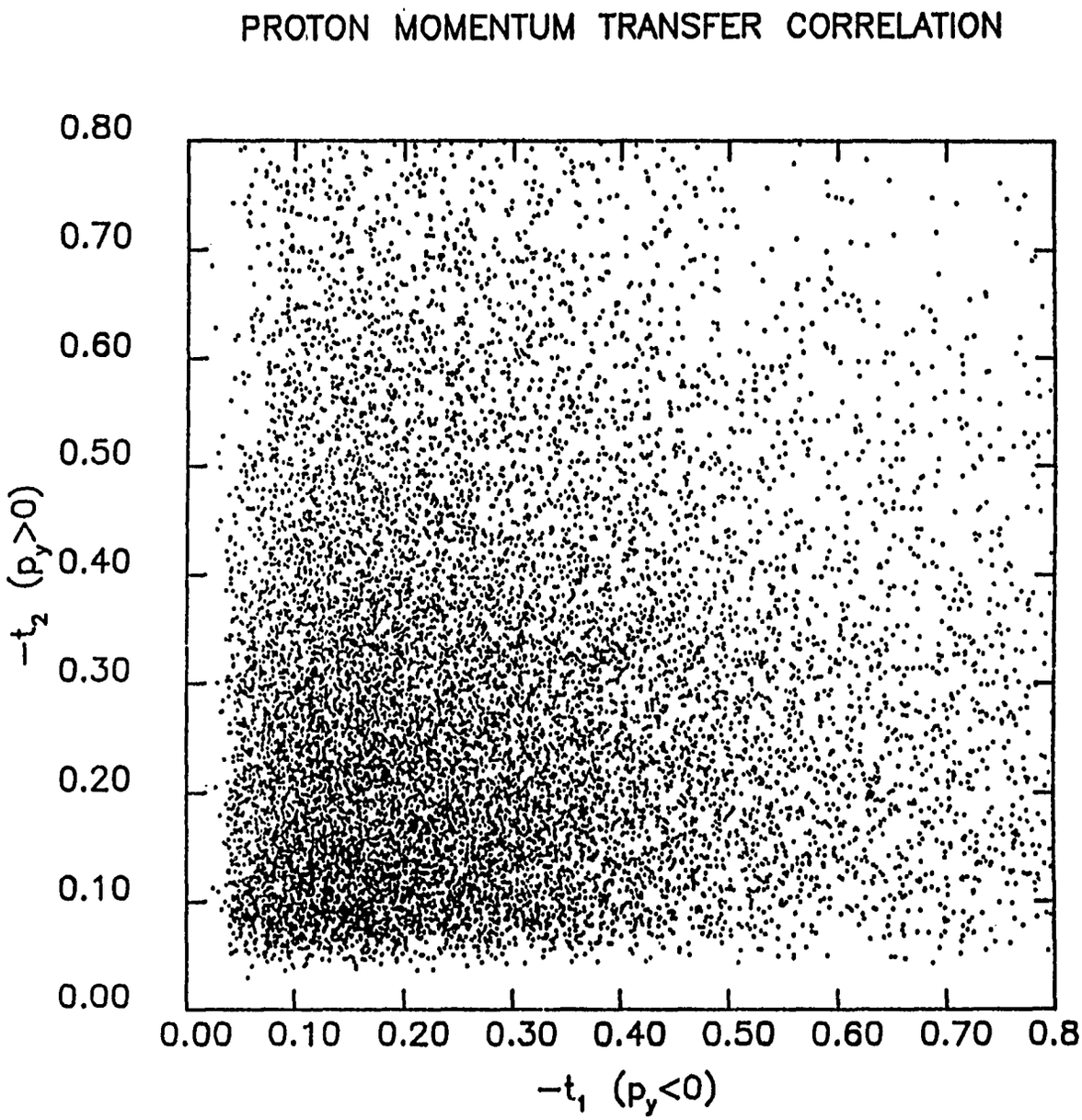

Figure 4.8. Scatterplot showing the correlation of the momentum transfer of the two fast leading protons

All of these studies seem to indicate that we have succeeded in the separation a sample of events that are consistent with DPE being the dominate production mechanism. The contribution from single diffraction appears to be quite small.

4.2. SFM Acceptance Corrections

After obtaining the 4C sample described in Section 4.1, the next step in the analysis was to correct for the acceptance of the SFM detector. This is particularly important for studying angular distributions in order to perform a spin-parity analysis. The acceptance calculations for the DPE data were performed in careful detail for this trigger. The approach used a combination of Monte Carlo generated data and so-called "Minimum Bias" data recorded with the SFM in order to fully correct for effects due to the limited and nonuniform acceptance of the SFM.

First, a Monte Carlo program was used for generating single tracks. These tracks were then swum through the magnetic field of the SFM detector to calculate the exact path they would follow [Messerli]. The tracks could then be checked to see which chambers of the SFM they would pass through. By doing this for a large sample of events for different initial track directions and momenta, one can generate a set of tables to use to decide whether or not a specific track would satisfy any of the trigger requirements or would cause the event to be vetoed. The use of a set of tables keeps one from having to calculate the trajectory of every track generated by later Monte Carlo programs in order to see which parts of the detector the track would have passed through. This is important due to

the large number of generated events necessary to calculate the acceptance of the SFM detector for various processes.

Next, events were generated according to general phase space requirements by a Monte Carlo process. The process used the CERN program FOWL, which is described in the CERN Program Library and is a well understood phase space event generator [James 1967]. These events were then tested to see if they would have been accepted or rejected by the OR trigger using the tables generated by the single tracks described above. Approximately three million events were created for each 100 MeV mass bin of the central $\pi^+\pi^-$ pair in the range of 300 to 3000 MeV (i.e., Mass($\pi^+\pi^-$) = 300, 400, 500,..., 3000 MeV). Events were only generated for every 100 MeV interval due to the large amount of computer processing necessary to generate these events.

For each generated fake event, an additional weight was calculated for the efficiency of the SFM reconstruction code to locate and correctly measure tracks. In order to calculate this, data taken with a minimum bias trigger were used. A minimum bias trigger requires the presence of at least one possible track candidate in the detector in order to record the event. Thus, these events do a good job of representing the acceptance of the SFM detector and can be used to calculate a weight that gives the probability that a track in a specific region of the detector will be reconstructed by the SFM reconstruction code. There were two parts to this correction. First, one expects minimum bias events to exhibit cylindrical symmetry around the beam pipes of the ISR since the beam protons are not polarized. Thus, for a specific bin in x_F and transverse momentum p_t, the azimuthal angles of the leading protons around

the beam pipe were plotted, and a weight was calculated which forced this distribution to be be flat. Second, the single inclusive particle distribution is well known from other experiments [Alper et al. 1975]. Thus, one can plot the p_t distribution for a specific x_F bin and calculate the weights necessary to bring the distribution into agreement with the known distributions.

One more set of weights was generated to correct for assymetries in the acceptance of the SFM for the fast outgoing protons. It was discovered that there was a dependence upon the projected angle of the fast outgoing protons in the x-z plane of the SFM (see Figure 2.4). The projected angles in the x-z plane are equivalent to looking at the transverse momentum components in the x and z directions, respectively, since the angles are defined by $\cos\Theta = p_x/p$ and $\cos\phi = p_z/p$. These projected angles in the x-z plane of the leading protons were tabulated for the real data and for the Monte Carlo data. A table of weights was then calculated that gave the Monte Carlo events the same distribution as the real data. This approach proved to be much better than using cuts to delete the regions where the Monte Carlo data gave drastically different results than what was observed in the real data. One of the major reasons this was done was because the real data must be subjected to the same cuts as the Monte Carlo data before they can be compared. Thus, if the cuts from the Monte Carlo are too stringent, an unacceptable amount of data would be lost.

At this point, one has a set of simulated events generated by Monte Carlo methods that (a) satisfy the OR trigger requirements and (b) carry a weight according to their position in phase space and to their probability

of being reconstructed by the SFM. These simulated events can then be subjected to the same analysis as the real data in order to separate effects due to the detector acceptance from those which come from real physical interactions.

4.3. Moment Calculations

The first step in trying to determine the spin and parity of the central system is to calculate the moments of the $\pi^+\pi^-$ decay angular distributions. The moments are defined in terms of the spherical harmonics $Y_L^M(\Theta,\phi)$:

$$Y(LM) = \langle Y_L^M(\Theta,\phi)\rangle = \frac{1}{n}\sum_{i=1}^{n} Y_L^M(\Theta_i,\phi_i)$$

where $L = 0,1,2,\ldots$, $M = -L,-L+1,\ldots,L$ and the sum runs over all of the measured events (note that the Y(LM) values for $M \neq 0$ have both real and imaginary parts). The coordinate system used is the $\pi^+\pi^-$ rest frame with the Pomeron-Pomeron axis defining the z-axis. The y-axis is defined as the normal to the plane formed by the incoming and outgoing momenta of one of the protons. This leaves one with an ambiguity, since one can choose either proton to define this plane. In this case, the proton with $p_y>0$ was chosen. Writing this coordinate system down explicitly we get:

$$\hat{z} = \frac{p^i - p^f}{|p^i - p^f|}$$

$$\hat{y} = \frac{p^i \times p^f}{|p^i||p^f|}$$

$$\hat{x} = \hat{y} \times \hat{z}$$

where p^i is the momentum of the incoming beam proton and p^f is the momentum of the same proton after it is quasi-elastically scattered in the DPE process (both in the $\pi^+\pi^-$ rest frame).

Due to parity conservation in the production process, it is irrelevant whether the direction of the y-axis is given by $p^i x p^f$ or $p^f x p^i$. This is because the reaction must be invariant under the transformation $R_{\hat{n}}(\pi)P$, where P represents a space inversion and $R_{\hat{n}}(\pi)$ is a 180^o rotation about the production normal (in this case the y-axis). Thus, the moments must be invariant under the transformation $\phi \rightarrow -\phi$. Since this changes the sign of the imaginary part of Y(LM), all the moments must be real.

Another property of this interaction is that it must be symmetric under the transformation $\hat{z} \rightarrow -\hat{z}$ since there is no way of choosing one proton momentum transfer direction over the other proton momentum transfer direction to define the positive z axis. This causes $\Theta \rightarrow \pi-\Theta$ and $\phi \rightarrow -\phi$. Since ϕ can change its sign by the arguments in the previous paragraph independent of what happens to Θ, the moments must be invariant under the separate transformation: $\Theta \rightarrow \pi-\Theta$. Under this transformation:

$$P_L^M(\cos\Theta) \rightarrow (-1)^{L+M} P_L^M(\cos\Theta)$$

Thus, all the nonzero moments must have L+M even. Note that the zero result comes from the fact that the moments are a sum, and the sum one gets from $0 \leq \Theta \leq \pi/2$ is exactly canceled by the sum one gets from $\pi/2 \leq \Theta \leq \pi$.

Note that the above arguments that (a) only the moments that are real and (b) only the moments that have L+M even can be nonzero come only from the production process being parity invariant, and do not depend on any

assumptions about the decay of the central system. Additional requirements may be placed on the moments if the two central pions are produced as the result of a parity conserving decay. In this case, the moments are invariant under a simple space inversion (i.e., it cannot matter whether we use the π^+ or π^- to define the angles). This means that the amplitude must be invariant under the transformations $\theta \rightarrow \pi-\theta$ and $\phi \rightarrow \pi+\phi$, which results in only moments with L even being nonzero. Thus, of all the nonzero moments, those with L odd can only come from background processes to the decay of the central system into two pions, provided one is considering only strong decay processes.

From these arguments, one can see that if any of the moments that are imaginary or have L+M odd are nonzero, then they can only come from the angular dependence of the acceptance of the detector. This was used as a check for the effectiveness of the acceptance corrections applied to the data.

In Figures 4.9-4.12 we show the normalized moments uncorrected for acceptance. Before these moments were plotted, the real data were forced to satisfy the same cuts as placed on the Monte Carlo data. Specifically, each outgoing fast proton was checked to see if the Monte Carlo would have included it, and the central tracks were checked to see if they would have been accepted by the Monte Carlo. The edges of the windows generated to decide if the OR trigger was satisfied were loosened slightly in order to avoid forcing an unnatural sharp cutoff on the real data. This reduced the number of events to 13,656. The $\pi^+\pi^-$ mass distribution changes insignificantly so it is not replotted here.

Superimposed on these plots of the data are results of the same moment analysis performed on Monte Carlo generated data for different hypotheses for the angular dependence of the the decay. The solid line is the result for isotropic decay (i.e., S-wave), the dashed line is for P-wave decay, the dotted line is for D-wave decay, and the dashed-dotted line is for S+D wave decay with the phase of the interference term being set to 0^{o} and the relative magnitudes of S-wave and D-wave being equal. These curves are the result of a smoothing process that is necessary because of the fluctuations of the Monte Carlo values. These fluctuations are due to the weights which were calculated to force the Monte Carlo data to reproduce the distribution of the real data in the projected angle in the x-z plane for the outgoing leading protons. The Monte Carlo points (recall that they were done every 100 MeV) were well fit by two cubic polynomials which were forced to overlap and were matched by a cubic spline. The first cubic equation was fitted from 300 to 1300 MeV, and the second cubic equation was fitted from 900 to 3000 MeV. The values for the curves from 300 to 900 MeV were taken from the first polynomial, and the values for the curves from 1100 to 3000 Mev were taken from the second polynomial. The values for the entire curves were then obtained by a cubic spline, which took care of matching the two polynomials between 900 and 1100 MeV.

These plots show what the detector acceptance causes in the moment distributions. One can see that in many cases the detector is not sensitive to the different types of angular distributions. However, these plots clearly show that there is no evidence for anything other than S-wave below 1 GeV. Above 1 GeV the D-wave term and the S-D interference

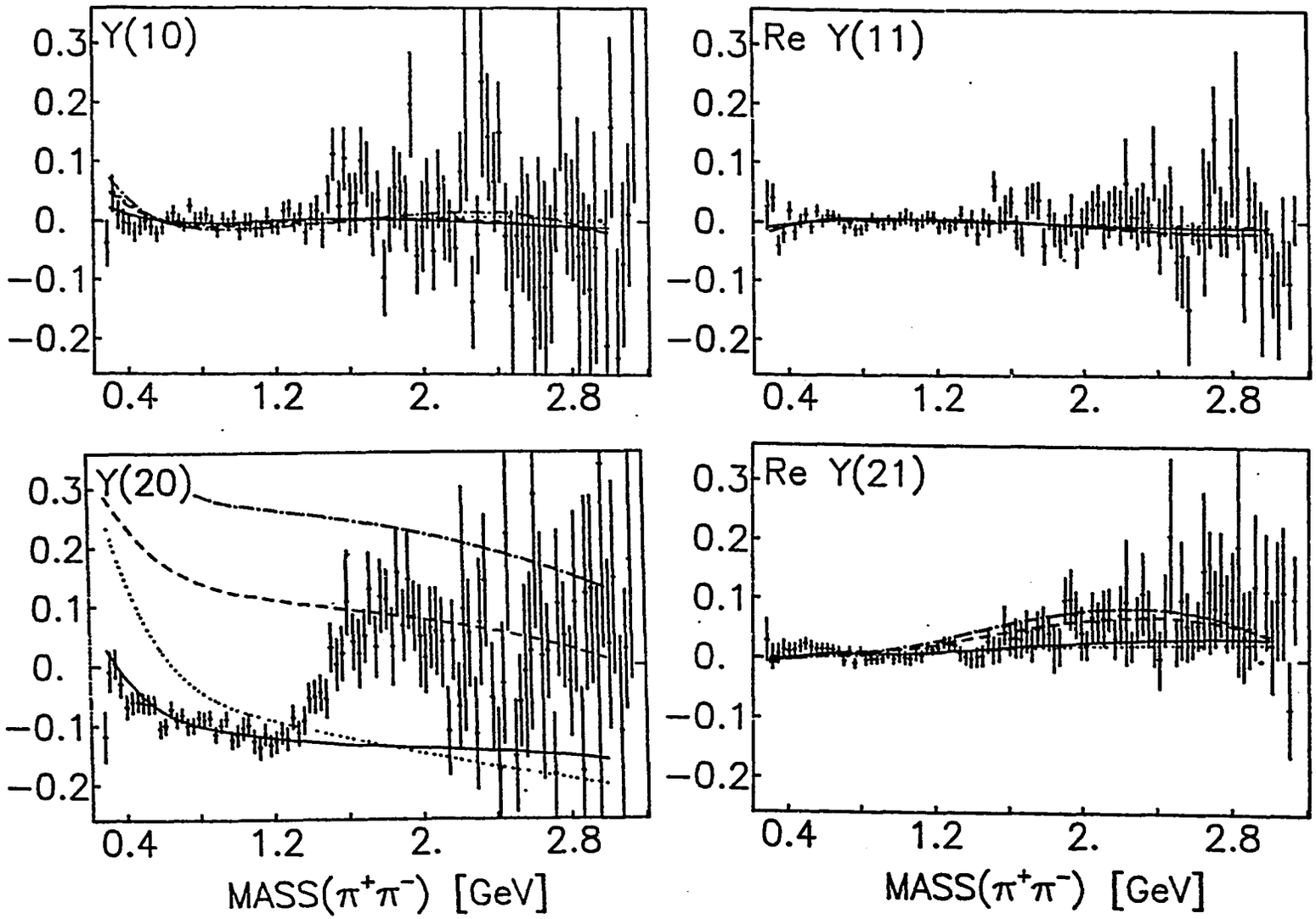

Figure 4.9. Selected moment distributions (Y(LM)) including Monte Carlo predictions (S-wave ⇔ solid line, P-wave ⇔ dashed line, D-wave ⇔ dotted line, S+D wave ⇔ dashed-dotted line)

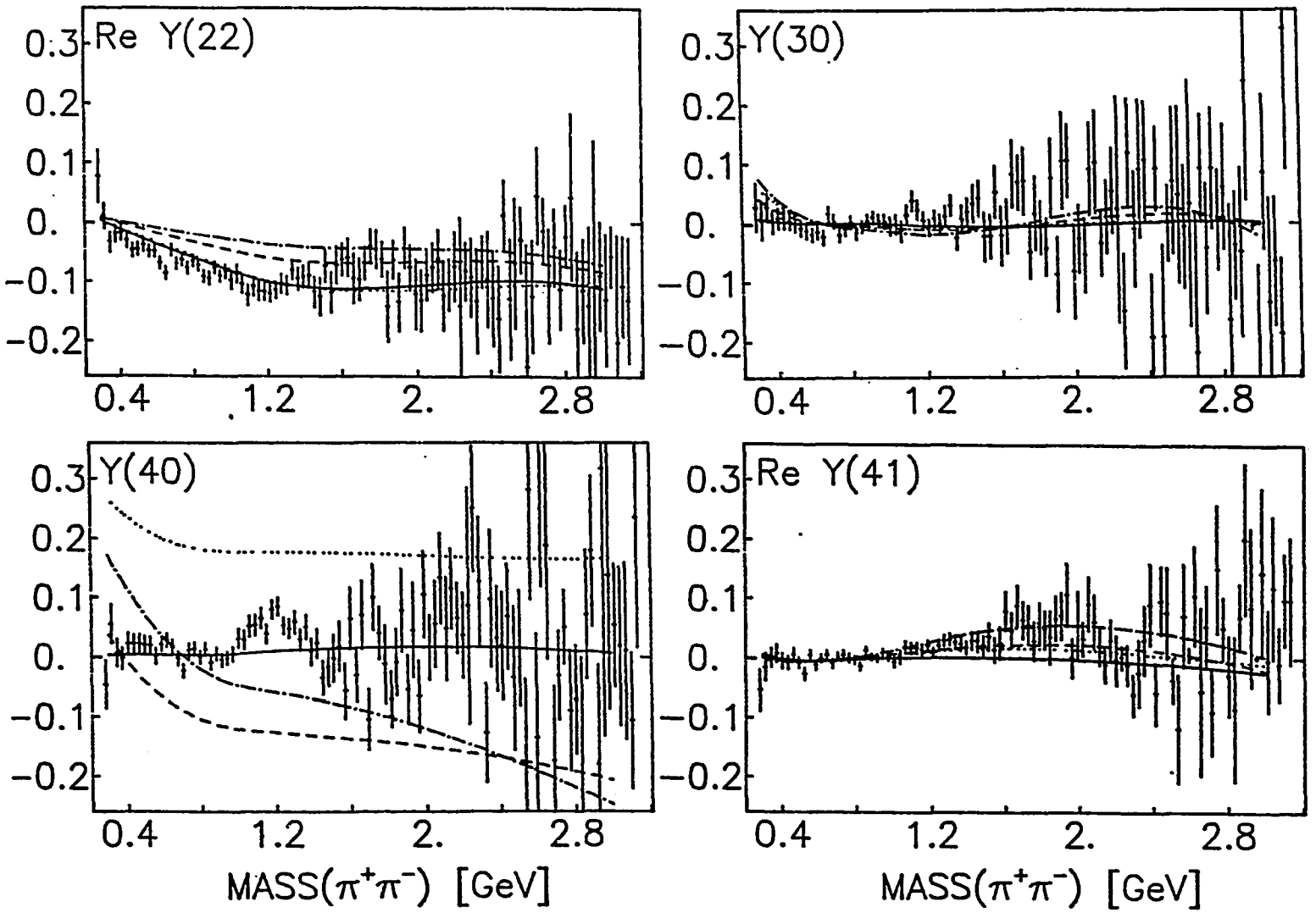

Figure 4.10. Selected moment distributions (Y(LM)) including Monte Carlo predictions (S-wave ⇔ solid line, P-wave ⇔ dashed line, D-wave ⇔ dotted line, S+D wave ⇔ dashed-dotted line)

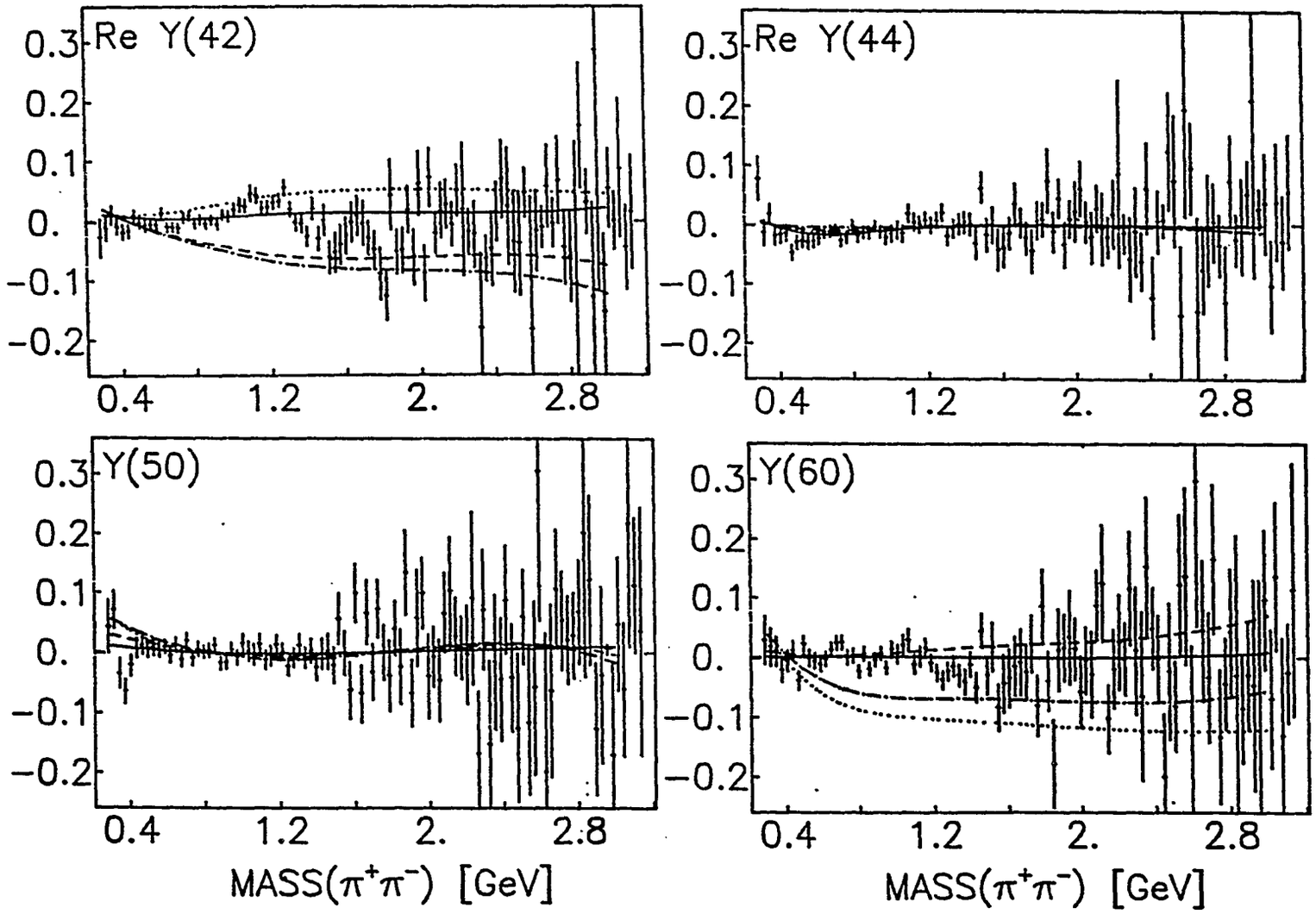

Figure 4.11. Selected moment distributions (Y(LM)) including Monte Carlo predictions (S-wave ⇔ solid line, P-wave ⇔ dashed line, D-wave ⇔ dotted line, S+D wave ⇔ dashed-dotted line)

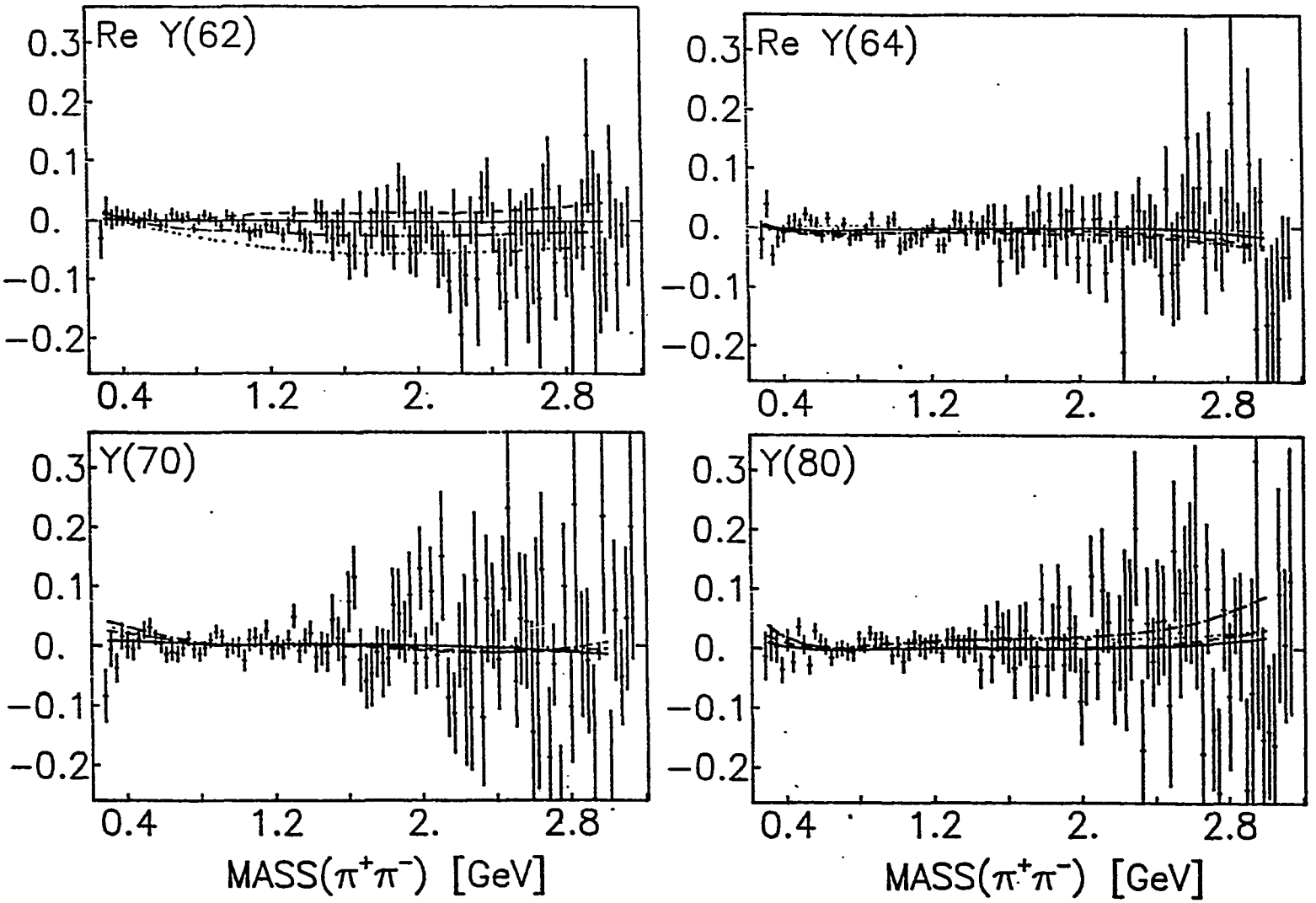

Figure 4.12. Selected moment distributions (Y(LM)) including Monte Carlo predictions (S-wave ⇔ solid line, P-wave ⇔ dashed line, D-wave ⇔ dotted line, S+D wave ⇔ dashed-dotted line)

term become important and a combination of S-wave and D-wave plus their interference term appears to be sufficient to fit the moment distributions of the data. However, a more detailed analysis is necessary before one can say exactly how much S-wave and D-wave are present in these moment distributions. This is the Spin-Parity analysis described in the next section.

4.4. Spin-Parity Analysis

In order to calculate the relative strengths of the S-wave and D-wave plus any interference effects between them for the decay of the central system into the $\pi^+\pi^-$ pair a fit must be done. This fit will also be used to make sure that S-wave and D-wave plus their interference are sufficient to fit the moment distributions. This requires using acceptance corrections to separate the real angular dependence of the data from that forced on it by the acceptance of the detector.

One method is to fit the moments of the data to a function of the moment distributions calculated by Monte Carlo for various decay hypotheses. This means that each moment is expected to be described by a linear combination of the Monte Carlo moment distributions plotted in Figures 4.9-12. Specifically,

$$Y(LM) = \sum_{i=1}^{n} a_i Y_i^{MC}(LM)$$

where $Y_i^{MC}(LM)$ is the value of the Monte Carlo Y(LM) for a specific decay hypothesis, a_i is its respective coefficient, and the sum runs over the

hypotheses used to fit the Y(LM) distributions of the data. Since only n hypotheses will be used and there are m moment distributions to be fitted, the above results in a system of m equations and n unknowns. Thus, the best solution will be chosen to be the set of a_i's that minimize the chi-square defined by:

$$\chi^2 = \sum_{k=1}^{m} [(\sum_{i=1}^{n} a_i Y_i^{MC}(LM))_k - Y_k(LM)]/\sigma_k^2$$

where the error used is the error on the data.

Since only states with M = 0 and even L are are permitted for the central decaying system in DPE (recall that the pomerons are spinless bosons with positive space and charge parity), and all evidence shows that DPE is the dominant production mechanism, the data were fitted assuming that the central system came from the decay of only S-wave and D-wave states with M = 0. Thus, the only Y_L^M hypotheses for the Monte Carlo data used were the angular decay distributions Y_0^0 and Y_2^0. Thus, there were three parameters to find, (1) $|S|^2$, the amount of Y_0^0 or S-wave, (2) $|D|^2$, the amount of Y_2^0 or D-wave, and (3) $|S||D|\cos\delta$, the phase of the interference term between S-wave and D-wave.

There were really just two parameters for the fit, $|S|^2$ and $\cos\delta$, since $|D|^2 = 1-|S|^2$. The χ^2 was minimized using the MINUIT minimization routines developed at CERN. The initial values were found using the SEEK routine in MINUIT, which uses a Monte Carlo method to search for the minimum of the χ^2 function. The results of SEEK were then used as the starting positions for SIMPLEX, which uses a simplex method developed by Neldler and Mead that is reasonably safe even if SEEK gave a result far

from the actual minimum. Finally, the values found in SIMPLEX were used as the starting positions for MIGRAD, which is based on a variable metric method by Fletcher. All of the MINUIT routines are described in the CERN MINUIT Long Write-up [James 1983]. The results of this fit, as well as the errors calculated by MIGRAD are given in Table 4.2 and are plotted in Figures 4.13-15. The quoted errors correspond to a change in the value of the χ^2 value of 1.0.

The moments included in the fit were the ones that showed the capability of separating out the behavior of S-wave and D-wave angular decay distributions. The following moments were selected to use: (1) Y(20), (2) ReY(21), (3) ReY(22), (4) Y(40), (5) ReY(41), (6) ReY(42), (7) Y(60), (8) ReY(62) and (9) Y(80). The most important moments to the fit were Y(20) and Y(40). The inclusion of additional moments (up to 27 moments were tried) had little effect on the results of the fits.

The fits given here were performed in 90 MeV bins (i.e., three data bins were combined from Figs. 4.9-12 before the fit was made). This relatively large interval was chosen for two reasons. One was that it reduced the errors on the fit parameters, and the other was that the fits done in 30 and 60 MeV bins show the exact same behavior, except that they have worse statistical fluctuations.

There are several comments in order on these results. One is that the two large negative fluctuations below 1.0 GeV in the cos(δ) term correspond to the D-wave term going to zero, making the fit insensitive to changes in cosδ. Thus, a more reasonable value would be obtained by averaging the two adjacent bins (i.e., cos$\delta \simeq 0.0$). Another is that the dip around 1.0 GeV in the cosδ term is not a statistical fluctuation and

Table 4.2. Results of fit to S-wave and D-wave ($|D|^2=1-|S|^2$)

Mass [Gev]	$\|S\|^2$	$\cos\delta$	$\|D\|^2$
0.375	0.974 ±0.028	-0.001 ±0.001	0.026 ±0.028
0.465	0.921 ±0.041	-0.002 ±0.001	0.079 ±0.041
0.555	0.953 ±0.036	-0.008 ±0.004	0.047 ±0.036
0.645	0.973 ±0.034	0.004 ±0.004	0.027 ±0.034
0.735	1.000 ±0.000	-1.000 ±1.755	0.000 ±0.000
0.825	0.983 ±0.013	-0.013 ±0.006	0.017 ±0.013
0.915	1.000 ±0.000	-0.952 ±1.620	0.000 ±0.000
1.005	0.958 ±0.040	-0.002 ±0.027	0.042 ±0.040
1.095	0.901 ±0.026	-0.422 ±0.089	0.099 ±0.026
1.185	0.760 ±0.040	-0.098 ±0.040	0.240 ±0.040
1.275	0.692 ±0.045	0.025 ±0.036	0.308 ±0.045
1.365	0.751 ±0.058	0.242 ±0.050	0.249 ±0.058
1.455	0.875 ±0.052	0.475 ±0.087	0.125 ±0.052
1.545	0.700 ±0.106	0.707 ±0.092	0.300 ±0.106
1.635	0.384 ±0.106	0.784 ±0.105	0.616 ±0.106
1.725	0.502 ±0.130	0.847 ±0.100	0.498 ±0.130
1.815	0.604 ±0.169	0.990 ±0.344	0.396 ±0.169
1.905	0.593 ±0.191	0.985 ±0.314	0.407 ±0.191
1.995	0.599 ±0.179	0.755 ±0.146	0.401 ±0.179
2.085	0.445 ±0.174	0.754 ±0.150	0.555 ±0.174
2.175	0.420 ±0.158	0.399 ±0.151	0.580 ±0.158
2.265	0.876 ±0.256	0.316 ±0.422	0.124 ±0.256
2.355	0.779 ±0.170	1.000 ±1.256	0.221 ±0.170

Table 4.2(cont). Results of fit to S-wave and D-wave ($|D|^2=1-|S|^2$)

Mass [Gev]	$\|S\|^2$	cosδ	$\|D\|^2$
2.445	0.212 ±0.127	0.948 ±1.087	0.788 ±0.127
2.535	0.951 ±0.096	0.719 ±0.546	0.049 ±0.096
2.625	0.419 ±0.354	1.000 ±1.979	0.581 ±0.354
2.715	0.876 ±0.126	0.995 ±1.856	0.124 ±0.126
2.805	0.667 ±0.217	1.000 ±0.169	0.333 ±0.217
2.895	0.520 ±0.330	0.795 ±0.354	0.480 ±0.330
2.985	0.053 ±0.145	1.000 ±1.710	0.947 ±0.145

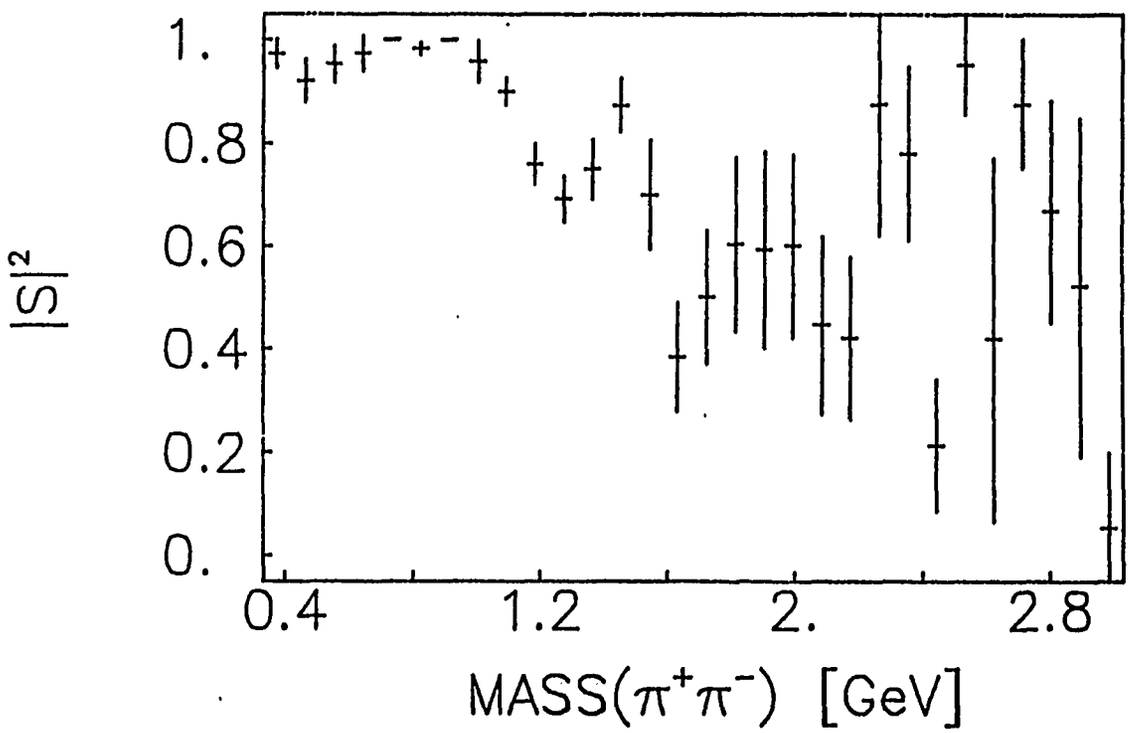

Figure 4.13. $|S|^2$ term from fit as a function of mass

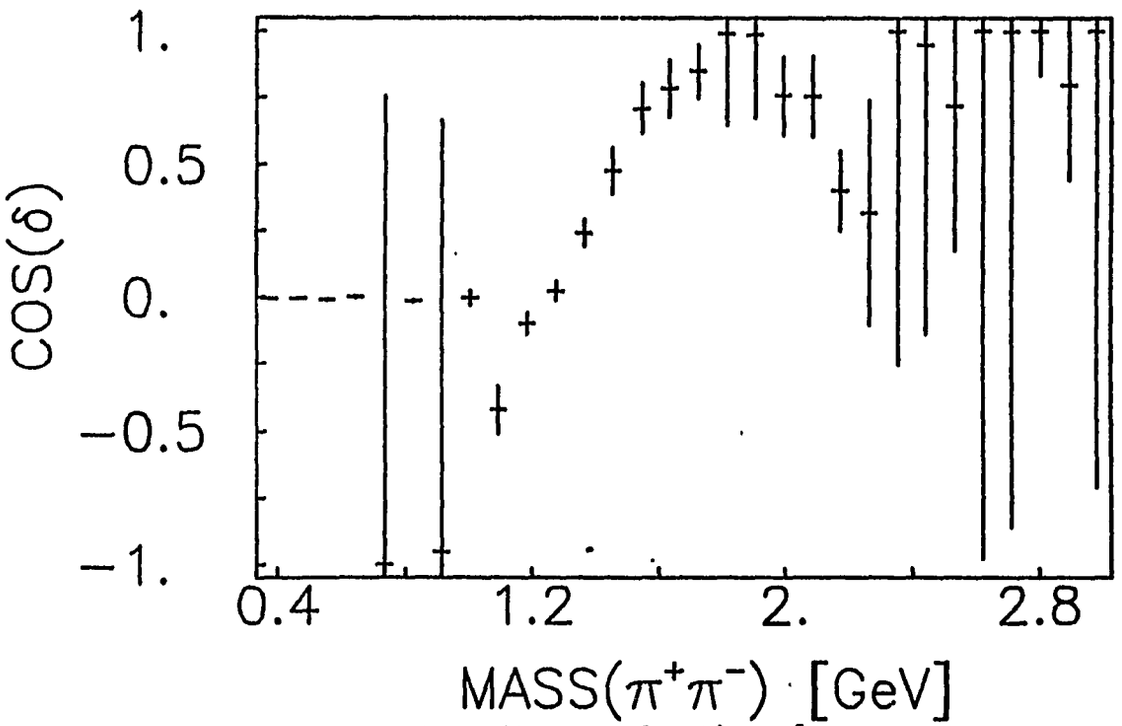

Figure 4.14. cos(δ) term from fit as a function of mass

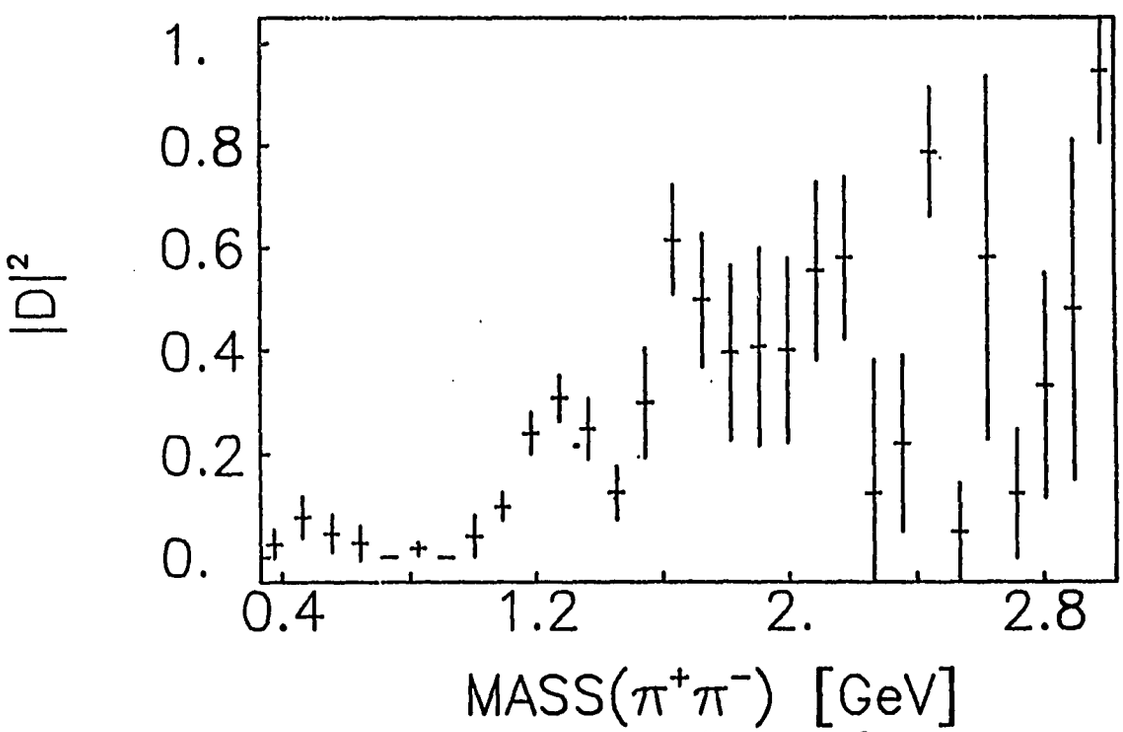

Figure 4.15. $|D|^2$ term calculated using $|D|^2 = 1 - |S|^2$

shows up clearly in the fits that were performed in 30 and 60 Mev bins not shown here.

These results clearly show a spin-two enhancement centered at a mass between 1230 and 1320 MeV, consistent with the mass of the f^o meson (m = 1274 MeV). Using Figure 4.16, one would place the peak of this enhancement at the position of the center of the bin just above 1200 MeV (low edge at 1230 MeV, high edge at 1320 MeV). This would correspond to 1275 MeV. On the basis of the fits done in 60 MeV bins (not shown), the center of the peak would be placed at about 1260 MeV. This adds a large amount of confidence to the identification of the peak in the $\pi^+\pi^-$ invariant mass distribution as the f^o.

This is even more significant considering previous work published by the SFM collaboration on the f^o [Breakstone et al. 1986]. If one looks at Figure 4.2(a), one will notice that the center of the enhancement attributed to the f^o is shifted down to about 1200 MeV. In the paper just mentioned, this mass shift was accounted for by fitting the mass spectrum to a relativistic D-wave Breit-Wigner distribution and a fast falling background term. The result of this fit found the mass and width of the enhancement to be equal to 1270 $\pm$10 MeV and 184 $\pm$25 MeV, respectively. The results of this spin-parity analysis confirm the results in the above paper, and the identification of the enhancement with the f^o meson.

5. FOUR PRONG "AND" DATA ANALYSIS

5.1. Final Cuts on Data

The four prong events recorded with the AND trigger are essentially a subset of the four prong OR data as explained in Section 2.3. Thus, the analysis was identical to that of the OR data described in Chapter 4, and one should reference that chapter for any details on the analysis. An attempt is made to keep redundant explanations in this chapter to a minimum.

Of the 406,356 events taken with the AND trigger which were successfully processed and stored on a DST, 28,955 of them were events with four outgoing tracks where all four tracks were found to come from a common vertex. The requirement of one and only one outgoing fast positively charged particle in each forward telescope with $0.55 < x_F < 1.8$ reduced this number of events 28,068. After the requirement of charge balance, the number of events was reduced to 22,867. These events were then subjected to the 4C-fit procedure described in Chapter 3.

As in Chapter 4, a cut on the probability-of-fit value at 0.05 was chosen after studying the invariant mass distribution of the central $\pi^+\pi^-$ pair. The probability-of-fit distribution is shown in Figure 5.1. As in the four prong OR data, there is a clear change in the mass distribution for a probability-of-fit cut between 0.04 and 0.05, where the distribution becomes dominated by events with unmeasured tracks (i.e., events which are not consistent with energy and momentum conservation). The invariant mass distributions of the central $\pi^+\pi^-$ pairs are shown in Figure 5.2 for events with probability-of-fit values greater than 0.05 (Figure 5.2(a)) and less

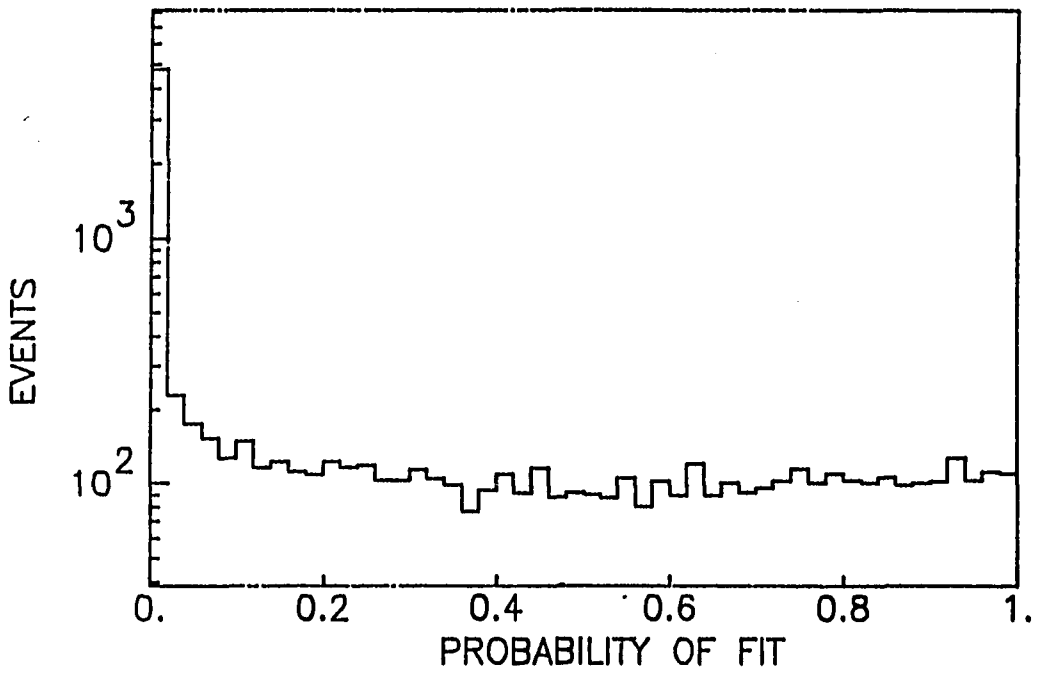

Figure 5.1. Probability-of-fit value distribution from the 4C-fit of the four prong AND data

than 0.05 (Figure 5.2(b)). For Figure 5.2(b), only events that had $\chi^2 <$ 100 were included (recall that this chi-square distribution has four degrees of freedom). Since the distribution changes even more drastically than for the OR data (i.e., the peak of the distribution shifts and the enhancement around the region of 1200 MeV disappears), the value of the 4C-fit is made very clear.

As in the four prong OR data, each leading outgoing proton was required to have $x_F > 0.8$, and any events that had a TOF mass identification of one of the central particles inconsistent with a pion were rejected. Table 5.1 shows the the improvement on the average error on the mass of the central $\pi^+\pi^-$ pair as a result of the 4C-fit.

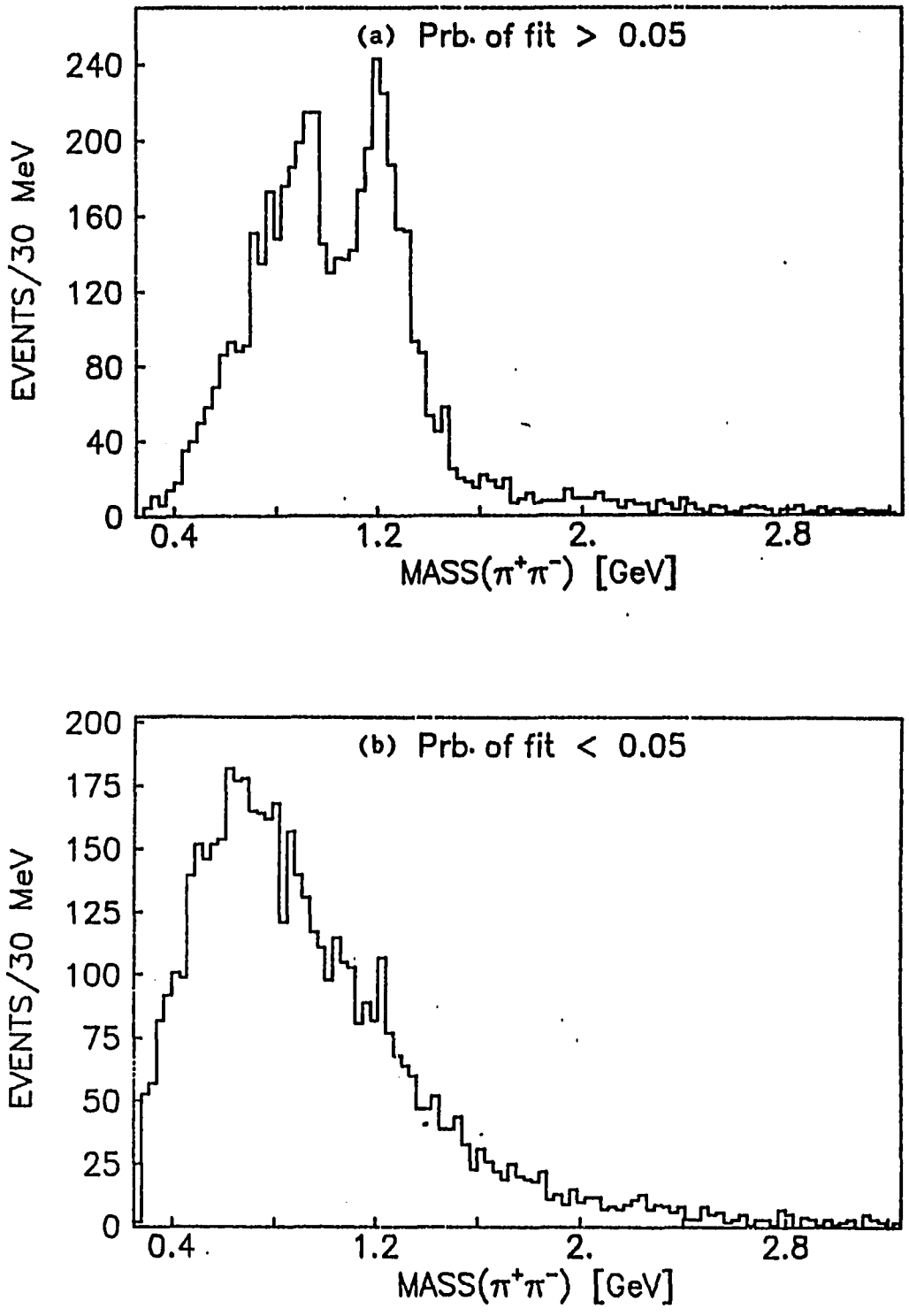

Figure 5.2. $\pi^+\pi^-$ mass distribution for (a) probability-of-fit values greater than 0.05 and (b) less than 0.05

Table 5.1. Error on the mass of the $\pi^+\pi^-$ system

Mass($\pi^+\pi^-$) [GeV]	Unfitted Error [GeV]	Fitted Error [GeV]
M<0.5	0.032	0.015
0.5<M<1.0	0.053	0.025
1.0<M<1.5	0.070	0.035
1.5<M<2.0	0.135	0.048
M>2.0	0.190	0.065

After all of the described cuts were performed, a total of 5,052 events remained in the four prong AND data sample. In Figure 5.2(a) we see no evidence for a signal for the ρ^0 meson (m = 770 MeV, $J^{PC} = 1^{--}$) in the $\pi^+\pi^-$ mass distribution, while there is a very strong enhancement in the region of the f^0 meson (m = 1274 MeV, $J^{PC} = 2^{++}$). As in Chapter 4, this is a powerful argument that we have in fact isolated a sample of DPE events by the use of this trigger. One can also see that the DPE trigger limits the data to low mass values for the central $\pi^+\pi^-$ system.

The plot of x_F (not shown here since it looks just like Figure 4.6) for one outgoing leading proton versus x_F of the other outgoing leading proton again shows the double-pole distribution as expected for DPE (see Section 1.2.1). The momentum transfer t, of one fast leading proton versus the other again shows no obvious correlation between the t values, just as for the OR data. As in the four prong OR case, these studies seem to indicate that we have succeeded in the separation of a sample of events that are consistent with DPE being the dominate production mechanism.

5.2. SFM Acceptance Corrections

After obtaining the 4C sample described in Section 5.1, the next step in the analysis was to correct for the acceptance of the SFM detector. This process was described in Chapter 4 and is the same for the AND data. In fact, the same Monte Carlo events were used. The only difference is that for the AND data the two central tracks were required to be on opposite sides of the detector and both of them must satisfy the trigger requirements described in Chapter 2. An important fact to note is that this additional requirement reduces the number of simulated events by a factor of ten compared to the OR trigger, since we are using the same set of Monte Carlo events for both data samples. Thus, there are only one-tenth as many simulated events for the AND trigger as compared to the OR trigger. This aspect of the Monte Carlo generation of events is consistent with the Fast13 trigger rates for the OR and AND data of 548 Hz and 86 Hz, respectively (see Chapter 2). Thus, one has a set of simulated events generated by Monte Carlo methods that (a) satisfy the AND trigger requirements and (b) carry a weight according to their position in phase space and according to their respective probability of being reconstructed by the SFM. These Monte Carlo events can then be subjected to the same analysis as the real data in order to separate effects due to the detector acceptance from those that come from real physical interactions.

5.3. Moment Calculations

The same moment analysis was repeated for the AND data that was performed on the OR data (see Section 4.3). Before this was done the real data were forced to satisfy the same cuts as placed on the simulated data generated by Monte Carlo, i.e., the real events were required to satisfy the AND trigger requirements as given by the same tables used to generate the Monte Carlo events. This reduced the number of events to 4,398. The resulting $\pi^+\pi^-$ mass distribution is shown in Figure 5.3 and uses the same size mass bins as used for the plots of the moments.

In Figures 5.4-5.7 we show the normalized moments uncorrected for acceptance. Superimposed on these plots are results of the same moment analysis performed on Monte Carlo generated data for different hypotheses

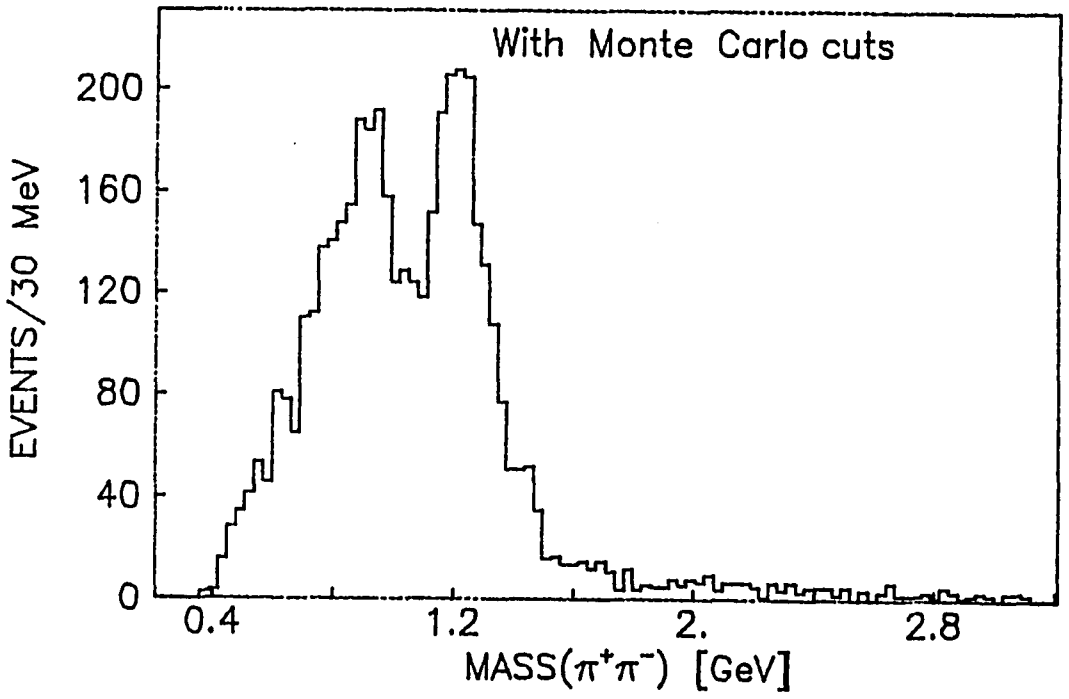

Figure 5.3. $\pi^+\pi^-$ mass distribution after cuts from Monte Carlo

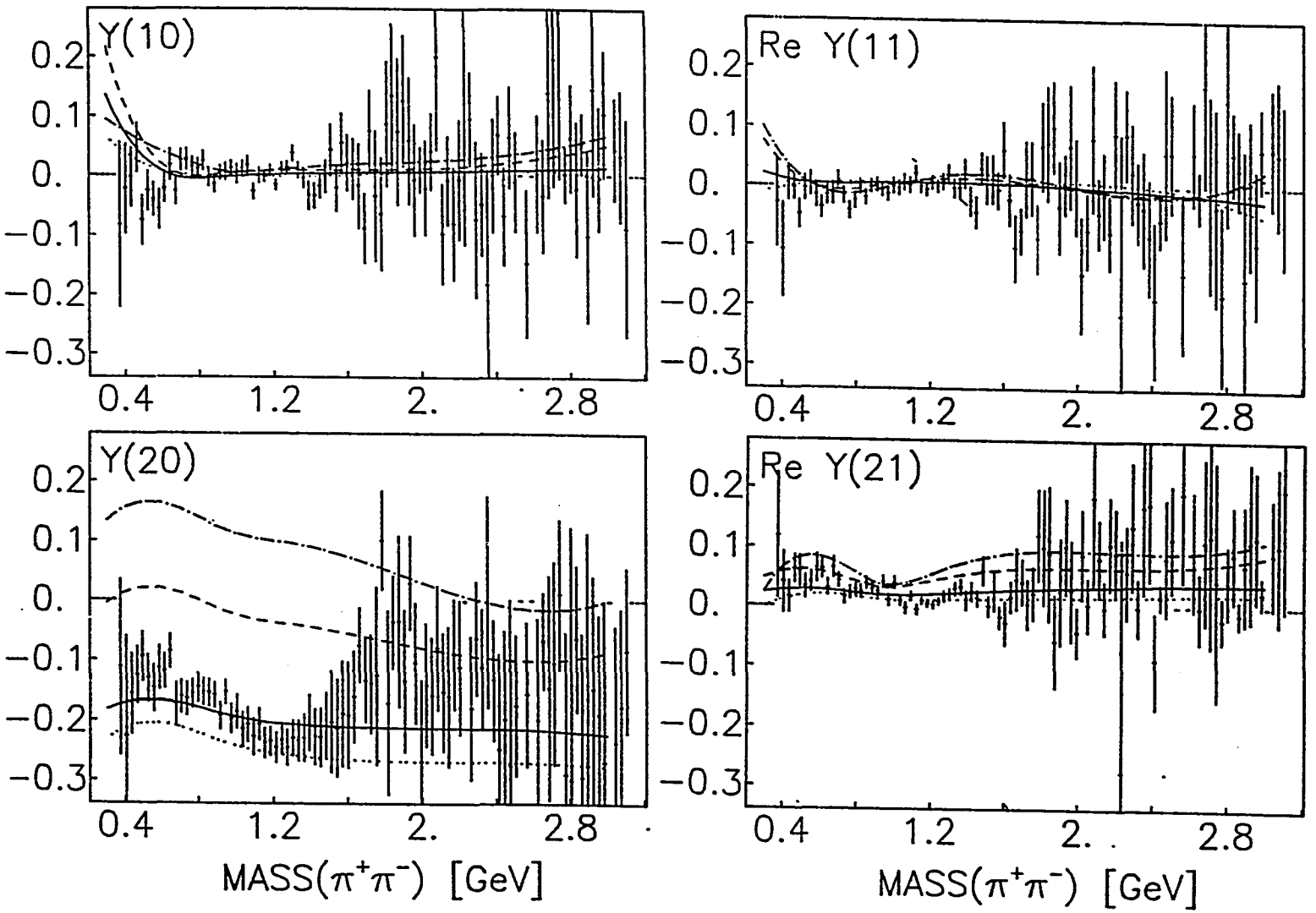

Figure 5.4. Selected moment distributions (Y(LM)) including Monte Carlo predictions (S-wave ⇔ solid line, P-wave ⇔ dashed line, D-wave ⇔ dotted line, S+D wave ⇔ dashed-dotted line)

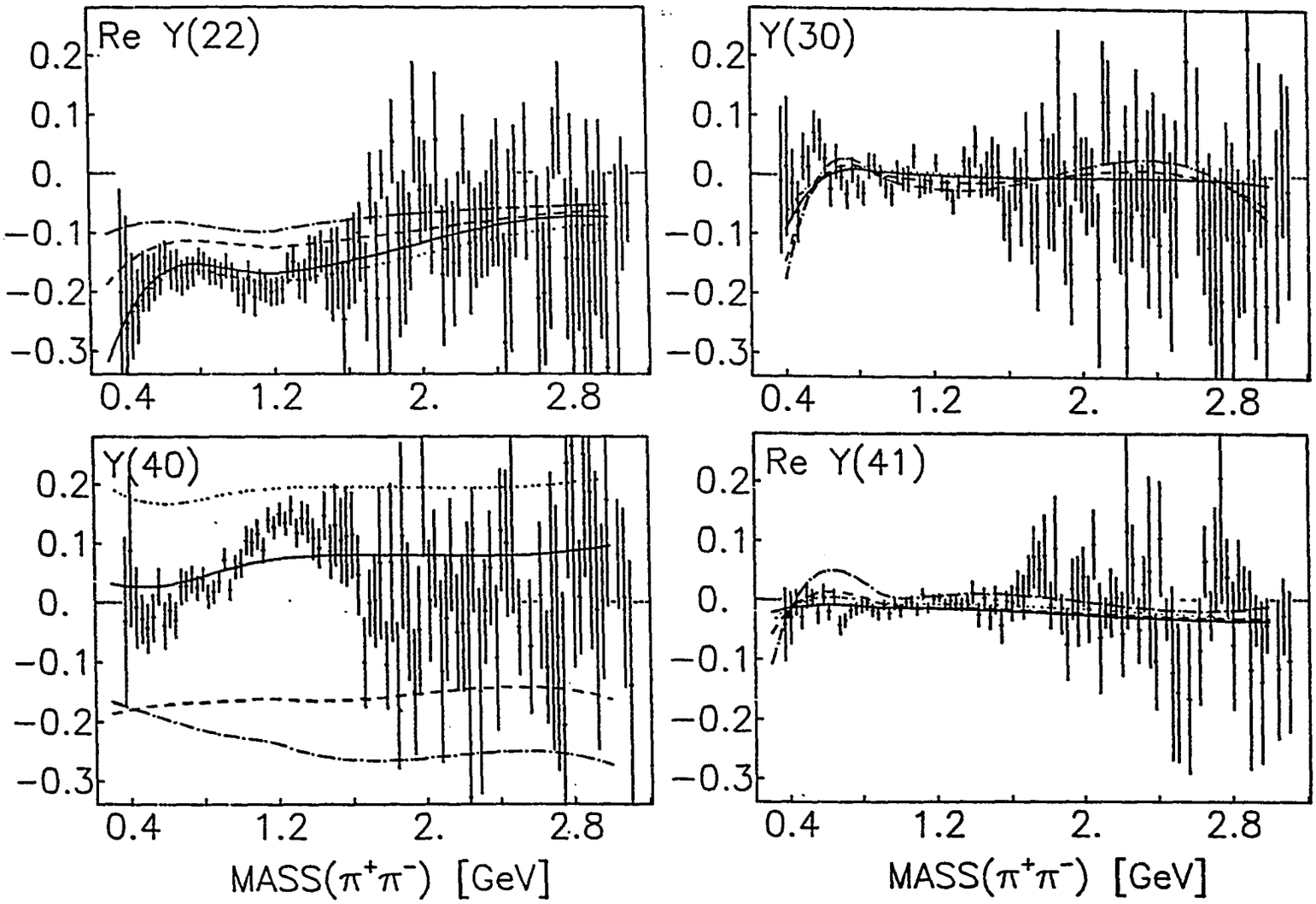

Figure 5.5. Selected moment distributions (Y(LM)) including Monte Carlo predictions (S-wave ⇔ solid line, P-wave ⇔ dashed line, D-wave ⇔ dotted line, S+D wave ⇔ dashed-dotted line)

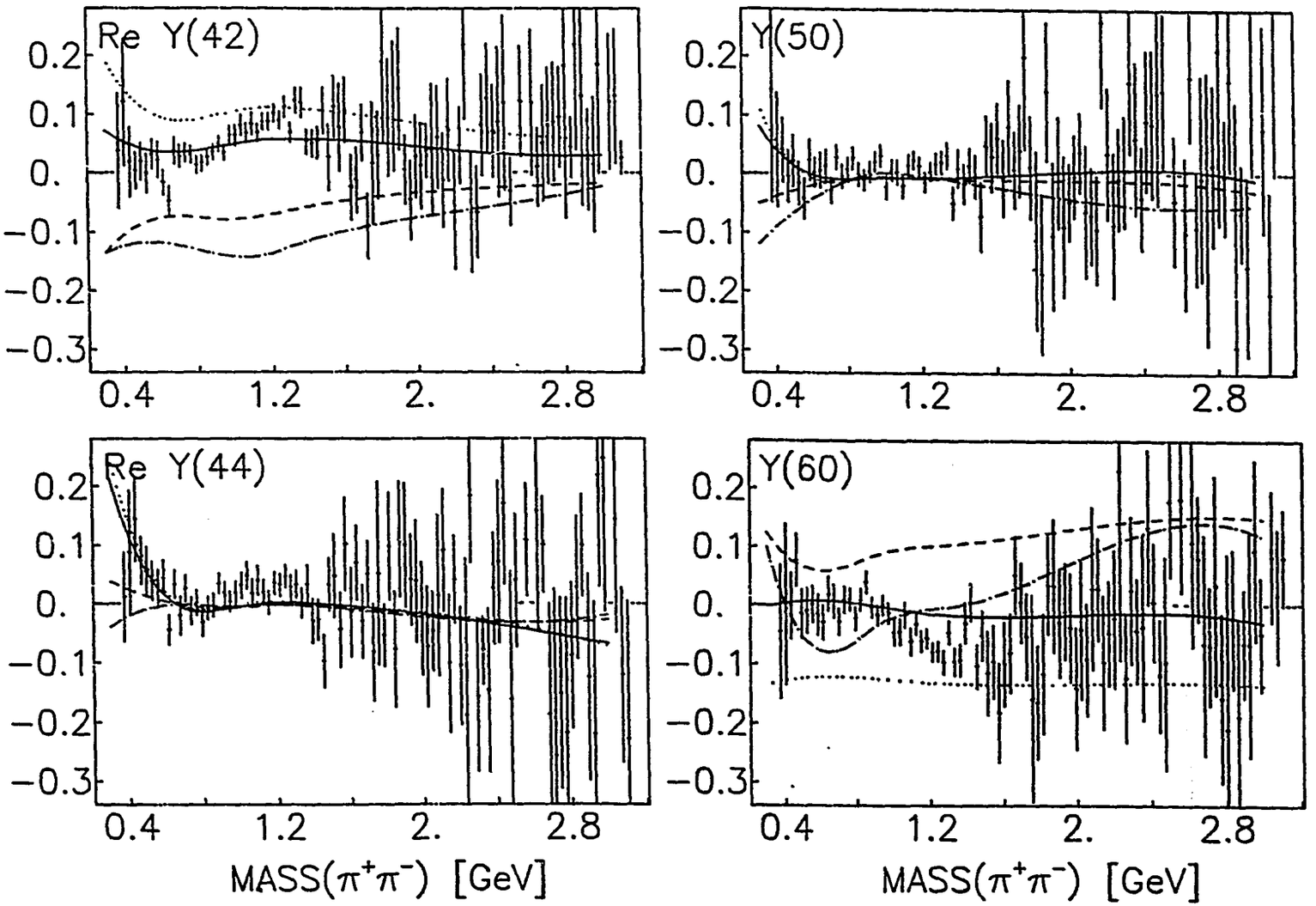

Figure 5.6. Selected moment distributions (Y(LM)) including Monte Carlo predictions (S-wave ⇔ solid line, P-wave ⇔ dashed line, D-wave ⇔ dotted line, S+D wave ⇔ dashed-dotted line)

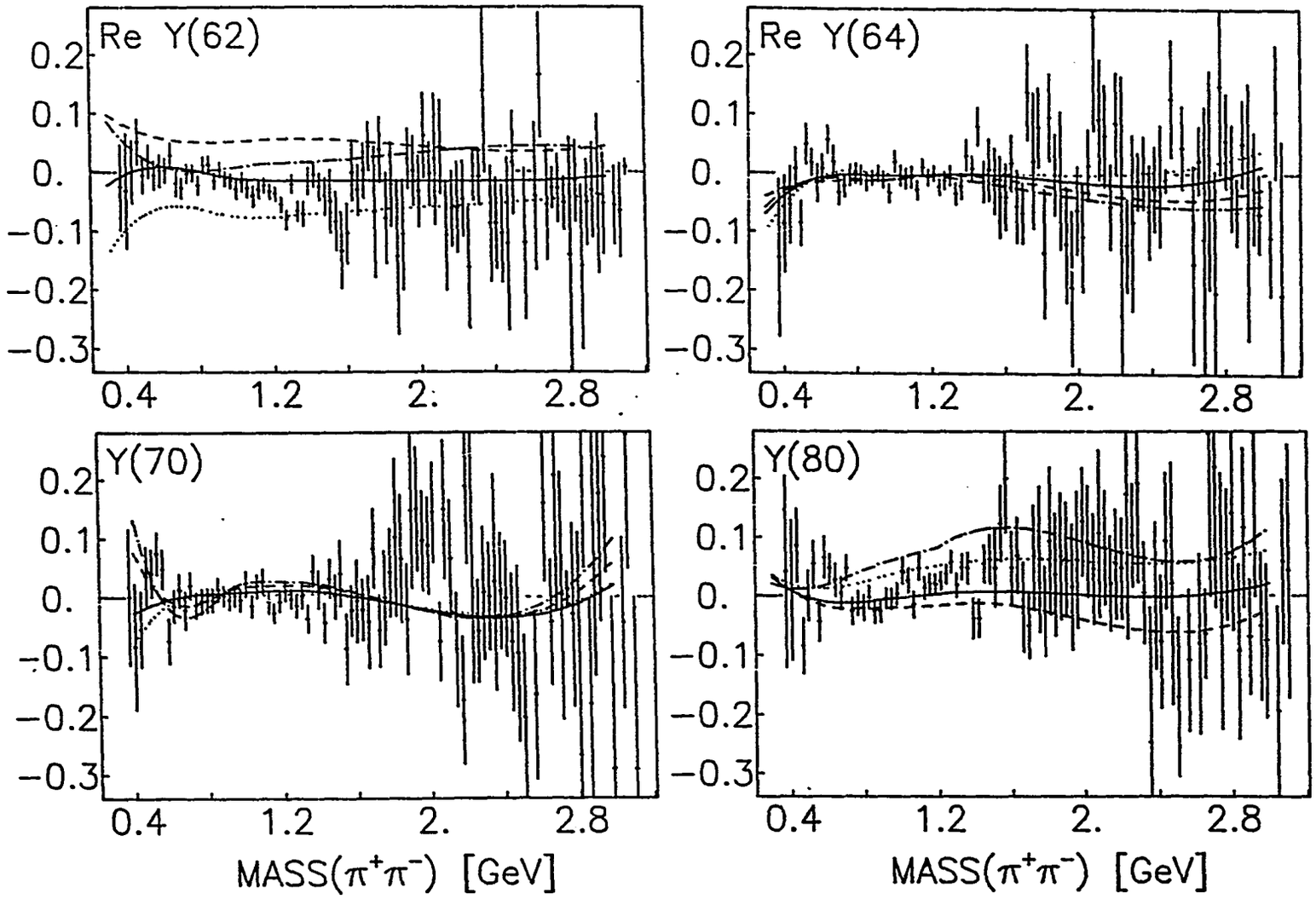

Figure 5.7. Selected moment distributions (Y(LM)) including Monte Carlo predictions (S-wave ⇔ solid line, P-wave ⇔ dashed line, D-wave ⇔ dotted line, S+D wave ⇔ dashed-dotted line)

for the angular dependence of the the decay. The solid line is the result for isotropic decay (i.e., S-wave), the dashed line is for P-wave decay, the dotted line is for D-wave decay, and the dashed-dotted line is for S+D wave decay with the phase of the interference term being set to 0^{o} and the relative magnitudes of S-wave and D-wave being equal. These plots show that there is little evidence for anything other than S-wave below 1 GeV. As in the OR data, above 1 GeV the D-wave term and the S-D interference term begin to become important, and a combination of S-wave and D-wave plus their interference appears to be sufficient to fit the moment distributions of the data.

5.5. Spin-Parity Analysis

The same fits were performed using the same nine Y(LM)s as in the OR data, and the same hypotheses were used to generate the expected distributions from the fake Monte Carlo events, i.e., moments Y(20), ReY(21), ReY(22), Y(40), ReY(41), ReY(42), Y(60), ReY(62), and Y(80) and the decay angular distributions of $|S|^2$, $|D|^2$, and $|S||D|\cos\delta$. The results of this fit, as well as the errors calculated by MIGRAD are given in Table 5.2 and are plotted in Figures 5.8-10. The quoted errors correspond to a change in the value of the χ^2 value of 1.0.

The fits given here were performed in 90 MeV bins (i.e., three data bins were combined from Figures 5.4-7 before the fit was made). This relatively large interval was needed in this case much more than in the OR data case in order to reduce the errors on the fit parameters. The fits done in 30 and 60 MeV bins show the same behavior, but they have much larger statistical fluctuations.

Table 5.2. Results of fit to S-wave and D-wave ($|D|^2=1-|S|^2$)

Mass [Gev]	$\|S\|^2$	cosδ	$\|D\|^2$
0.375	0.674 ±0.262	0.539 ±0.258	0.326 ±0.262
0.465	0.979 ±0.019	1.000 ±1.563	0.021 ±0.019
0.555	0.952 ±0.043	0.593 ±0.209	0.048 ±0.043
0.645	0.979 ±0.012	1.000 ±1.719	0.021 ±0.012
0.735	0.960 ±0.070	0.100 ±0.159	0.040 ±0.070
0.825	0.992 ±0.006	1.000 ±1.576	0.008 ±0.006
0.915	0.999 ±0.003	1.000 ±1.970	0.001 ±0.003
1.005	0.805 ±0.056	-0.037 ±0.081	0.195 ±0.056
1.095	0.705 ±0.060	-0.001 ±0.072	0.295 ±0.060
1.185	0.568 ±0.048	-0.091 ±0.056	0.432 ±0.048
1.275	0.429 ±0.082	0.041 ±0.093	0.571 ±0.082
1.365	0.477 ±0.082	0.037 ±0.090	0.523 ±0.082
1.455	0.769 ±0.106	0.006 ±0.136	0.231 ±0.106
1.545	0.028 ±0.039	1.000 ±2.000	0.972 ±0.039
1.635	0.550 ±0.210	0.734 ±0.198	0.450 ±0.210
1.725	0.464 ±0.244	0.956 ±0.403	0.536 ±0.244
1.815	0.537 ±0.203	1.000 ±0.146	0.463 ±0.203
1.905	0.610 ±0.348	1.000 ±1.871	0.390 ±0.348
1.995	0.408 ±0.206	1.000 ±1.302	0.592 ±0.206
2.085	0.827 ±0.227	1.000 ±1.996	0.173 ±0.227
2.175	0.585 ±0.327	0.817 ±0.303	0.415 ±0.327
2.265	0.424 ±0.256	1.000 ±0.351	0.576 ±0.256
2.355	0.847 ±0.177	1.000 ±0.430	0.153 ±0.177

Table 5.2(cont). Results of fit to S-wave and D-wave ($|D|^2=1-|S|^2$)

Mass [Gev]	$\|S\|^2$	$\cos\delta$	$\|D\|^2$
2.445	0.294 ±0.368	-0.027 ±0.557	0.706 ±0.368
2.535	0.854 ±0.115	1.000 ±0.157	0.146 ±0.115
2.625	0.824 ±0.151	1.000 ±0.195	0.176 ±0.151
2.715	0.483 ±0.314	1.000 ±0.434	0.517 ±0.314
2.805	0.096 ±0.946	-0.069 ±1.450	0.904 ±0.946
2.895	0.382 ±0.786	-0.542 ±0.632	0.618 ±0.786
2.985	0.979 ±0.064	1.000 ±1.939	0.021 ±0.064

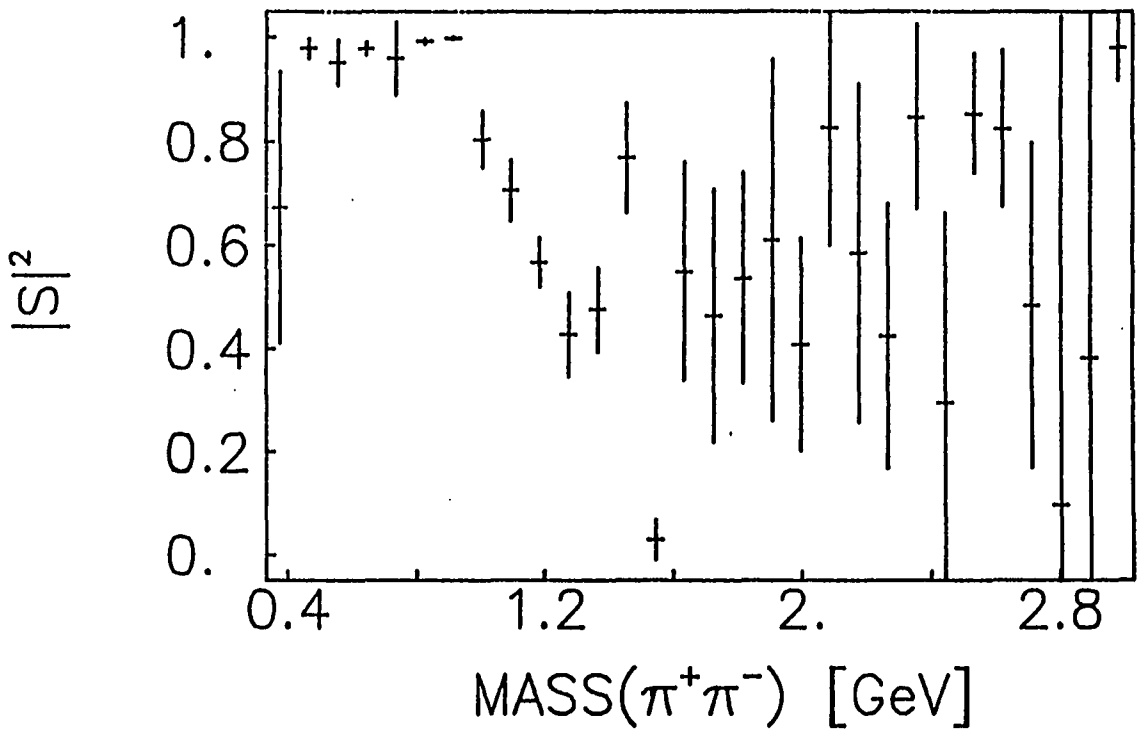

Figure 5.8. $|S|^2$ term from the fit as a function of mass

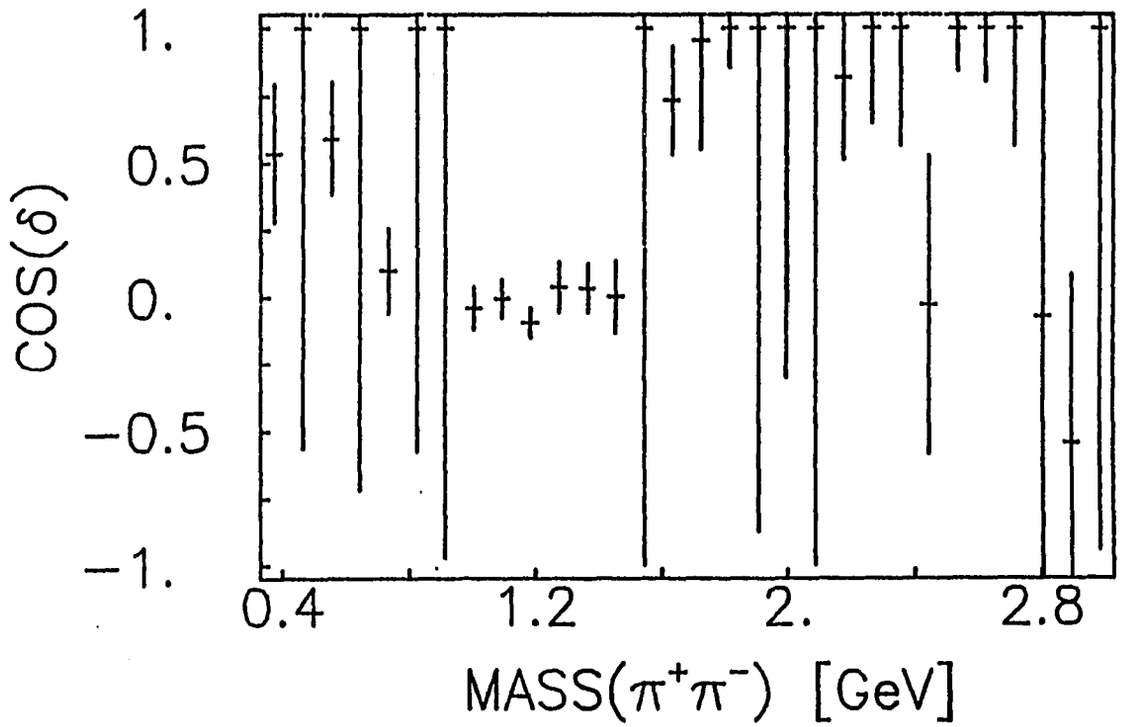

Figure 5.9. cos(δ) term from the fit as a function of mass

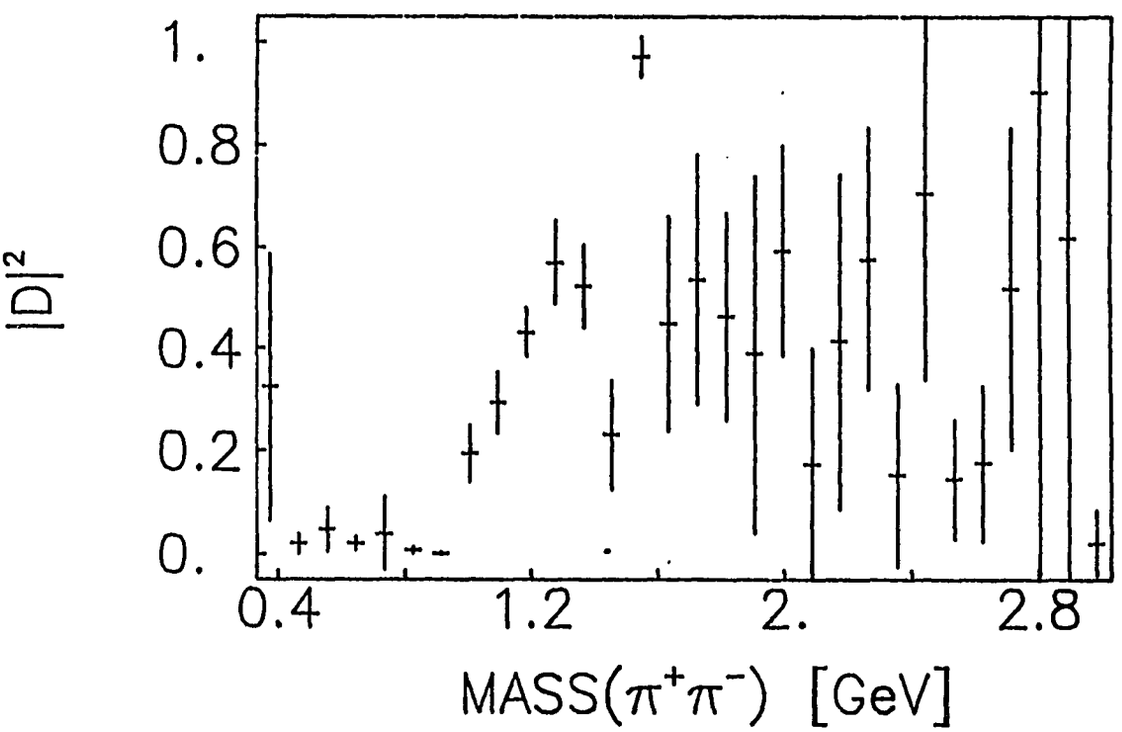

Figure 5.10. $|D|^2$ term calculated using $|D|^2 = 1 - |S|^2$

These results clearly show a spin-two enhancement centered at the mass of the f^0 meson. This provides much confidence to the identification of the peak in the $\pi^+\pi^-$ invariant mass distribution as evidence for the copious production of this state in DPE. As is stated in Chapter 4, this confirms previous work [Breakstone et al. 1986] that had to account for the shift in the peak of the f^0 downward by about 70 MeV. The very low value for the S-wave term just below 1.6 GeV is caused by what appears to be a statistical fluctuation in the moment distributions near this mass value (e.g., see the Y(20) and Y(22) moments).

The large fluctuations in Figures 5.8-10 make any other conclusion from these fits rather uncertain. One of the contributors to the fluctuations is simply that enough Monte Carlo events were not generated to avoid statistical fluctuations in the Monte Carlo predicted moments. The reason more events were not generated is a direct consequence of the fact that the AND trigger accepts only one-tenth as many events as the OR trigger. Thus, to generate the same number of events as were used in the OR data analysis one would require ten times the computer processing time, corresponding to roughly 150 CPU days on a VAX 11/785 computer. It was decided that the AND data was not of sufficient quantity to justify such an allocation of computer resources. However, the shortcomings of this spin-parity analysis should not overshadow the importance of showing that the large signal in the region of the f^0 is being produced by the decay of a spin-two object.

6. SIX PRONG "OR" DATA ANALYSIS

6.1. Final Cuts on Data

Of the 492,977 events taken with the OR trigger which were successfully processed and stored on a DST, 60,563 of them consisted of six outgoing tracks which were found to come from a common vertex. After the same cuts as described in Chapter 4, i.e., charge balance, and $0.55 < x_F < 1.8$ for the outgoing fast leading protons, there remained 41,085 six prong events which were subjected to the 4C-fit procedure described in Chapter 3.

The probability-of-fit value cut for this data was set at 0.20 since the probability-of-fit distribution does not fall as rapidly for low probability values in this case as it does in the four prong case. The probability-of-fit distribution is shown in Figure 6.1. For this cut on the probability-of-fit value, the data were studied to be sure that the probability distribution was a reasonable representation of the amount of background being included by the chosen cut placed on this quantity and to be sure that such a stringent cut on this value was necessary. It was decided by studying the mass distribution of the four pion central system in intervals of 0.02 around the 0.20 cut that the probability-of-fit distribution was accurate in reflecting that by cutting below 0.20 one would be allowing an unacceptable amount of background (i.e., events that were not consistent with energy and momentum conservation).

A cut was placed on the value of x_F calculated from the fitted track parameters for the two fast leading protons, requiring them to have

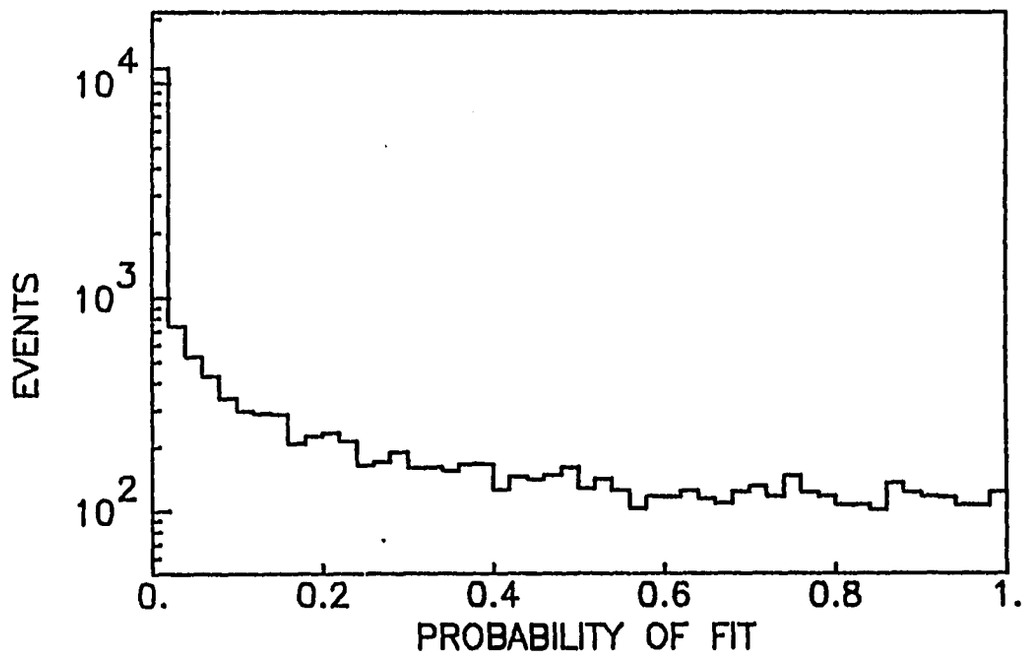

Figure 6.1. Probability-of-fit distribution for the 4C-fit

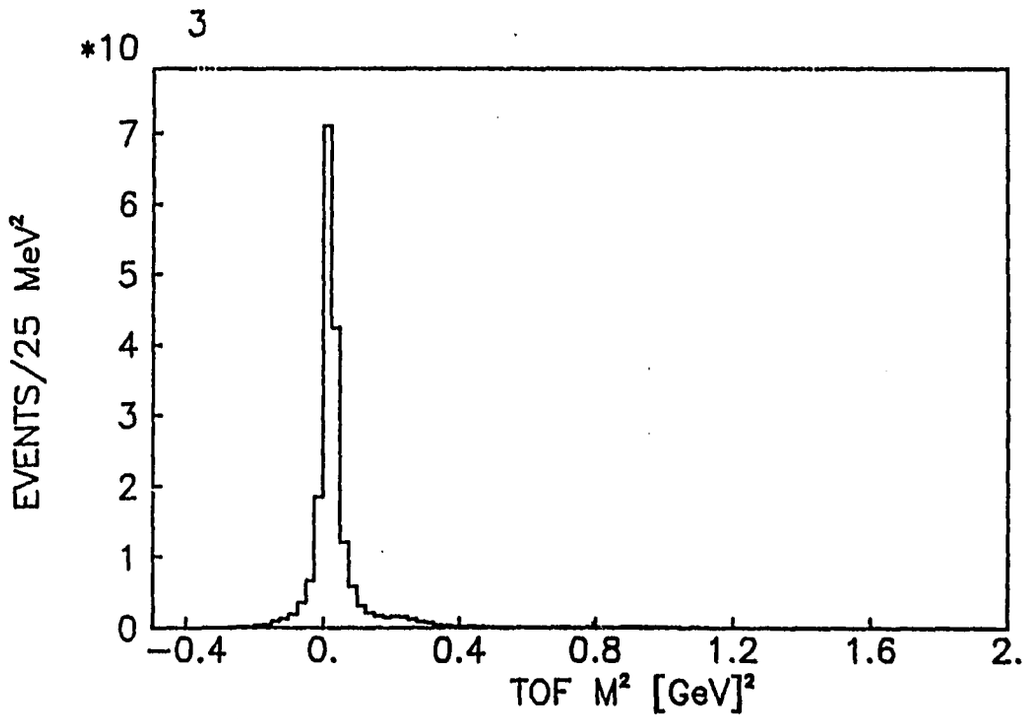

Figure 6.2. TOF M^2 distribution of the central tracks for all momenta

$x_F > 0.8$, as in the four prong OR data. Also, as in the four prong OR data, the majority of the events in the six prong OR data have all four of their central particles consisting of pions which can be seen by the plot of the measured TOF M^2 distribution shown in Figure 6.2. Thus, any events that have TOF information inconsistent with this hypothesis are rejected. These three cuts reduced the data sample to 5,321 events.

For these data, the plot of x_F of one fast leading proton versus the other is shown in Figure 6.3. As expected, the x_F values are on the average lower than in the four prong data, but the data still clearly show the double-pole structure expected for DPE events. The plots of the correlation of the azimuthal angles and momentum transfer of one fast leading proton with the other are very similar to the four prong data and are not shown here. Figure 6.4 shows the invariant mass distributions of the four particle central system for the six prong OR data using the unfitted (Figure 6.4(a)) and fitted (Figure 6.4(b)) track parameters. No unambiguous structure is apparent in the fitted mass distribution. However, there is some evidence for structure around 1.3 GeV because of the shoulder in the plot.

6.2. Study of the Four Pion Central State

With no clear structure in the four particle central system mass distribution, some different subprocesses will be examined to search for any enhancements in the data. The mass distribution of $\pi^+\pi^-$ pairs in the four particle central system is shown in Figure 6.5 (four combinations per event). There is a clear enhancement in the region of the ρ^0 meson (m = 770 MeV, Γ = 154 MeV, $J^{PC} = 1^{--}$). Note that ρ^0 production is allowed in

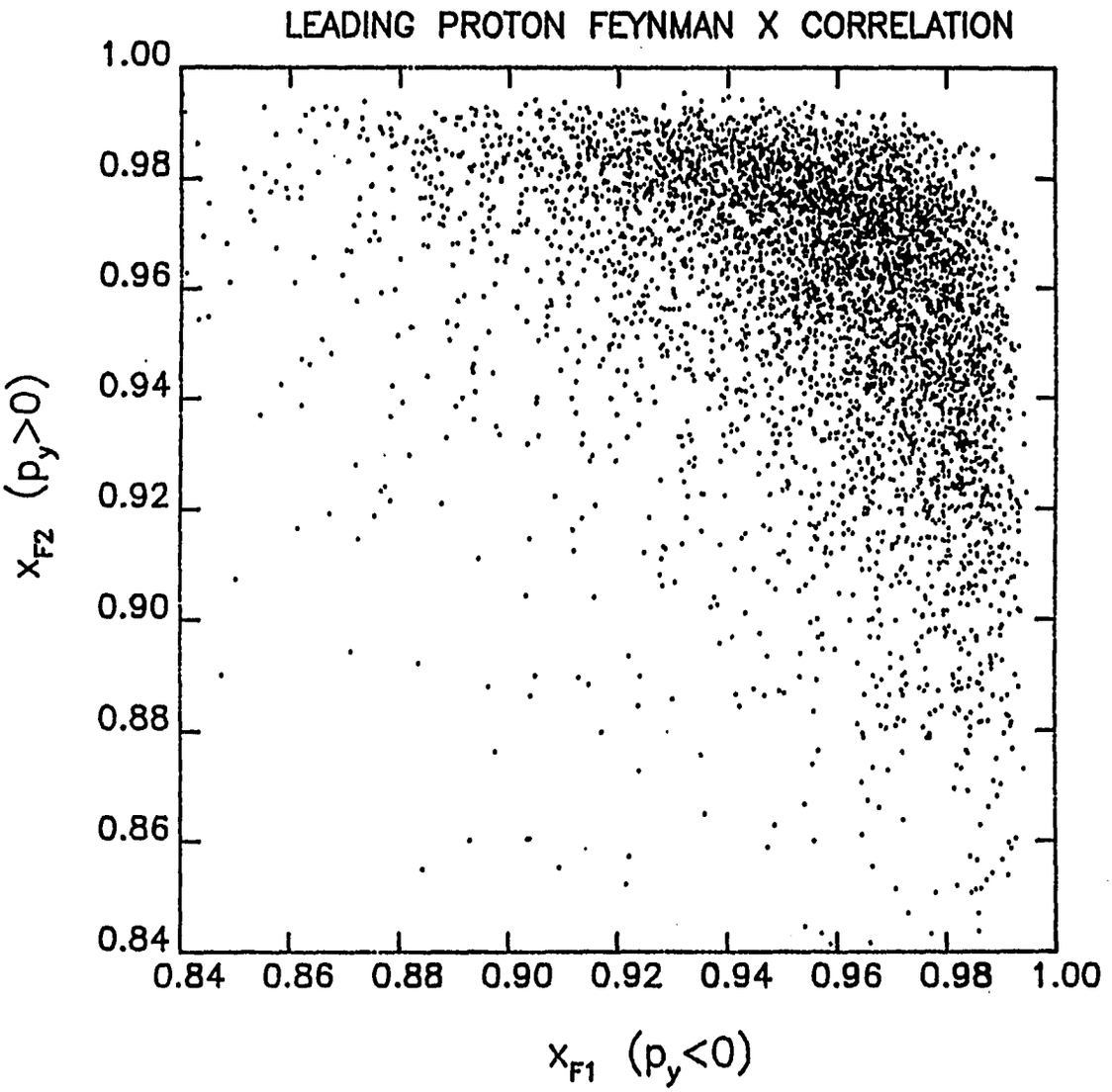

Figure 6.3. Scatterplot showing the correlation of x_F of one fast leading proton with x_F of the other fast leading proton

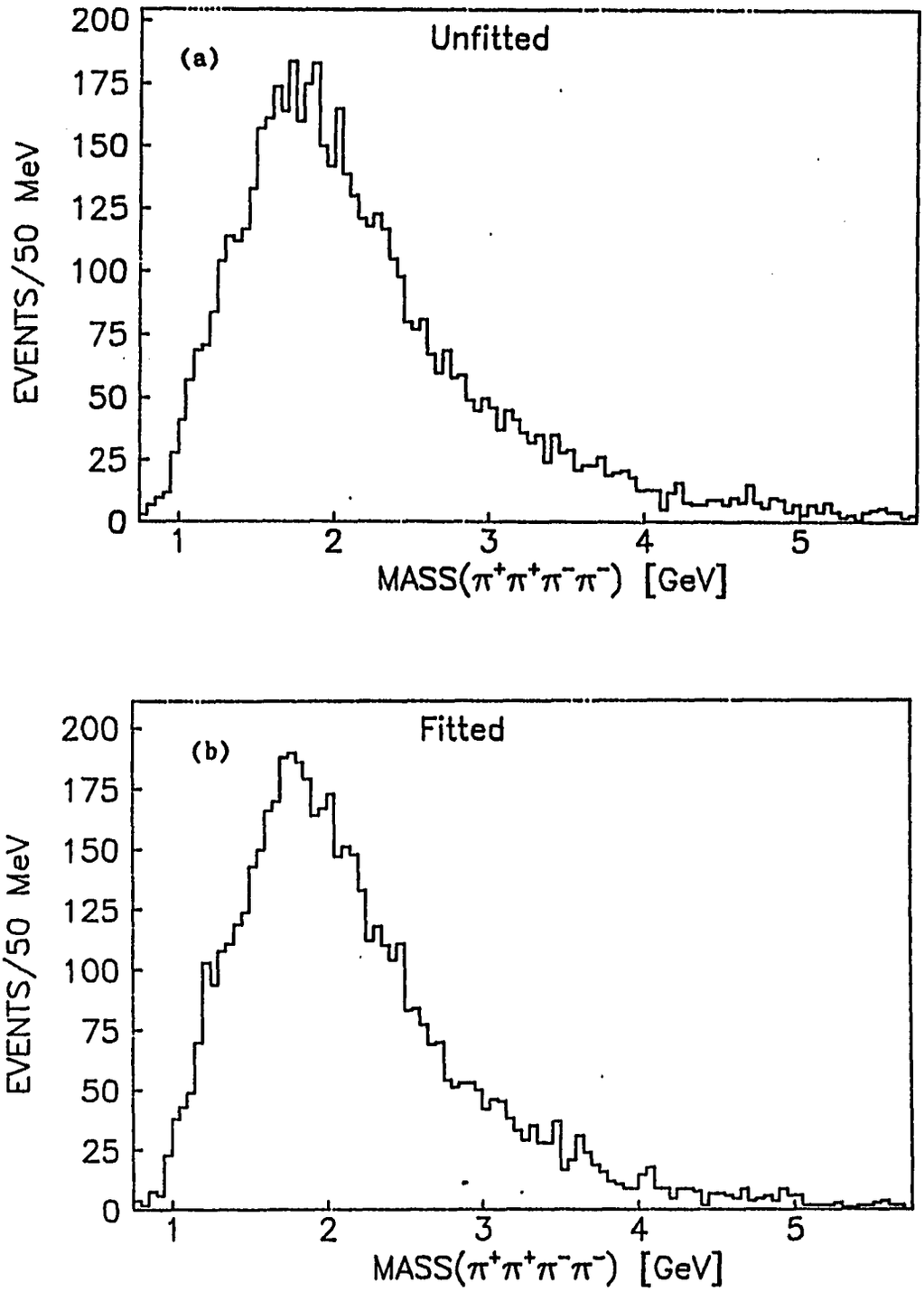

Figure 6.4. Mass distribution for central $\pi^+\pi^+\pi^-\pi^-$ system using (a) measured (unfitted) track parameters and (b) fitted track parameters

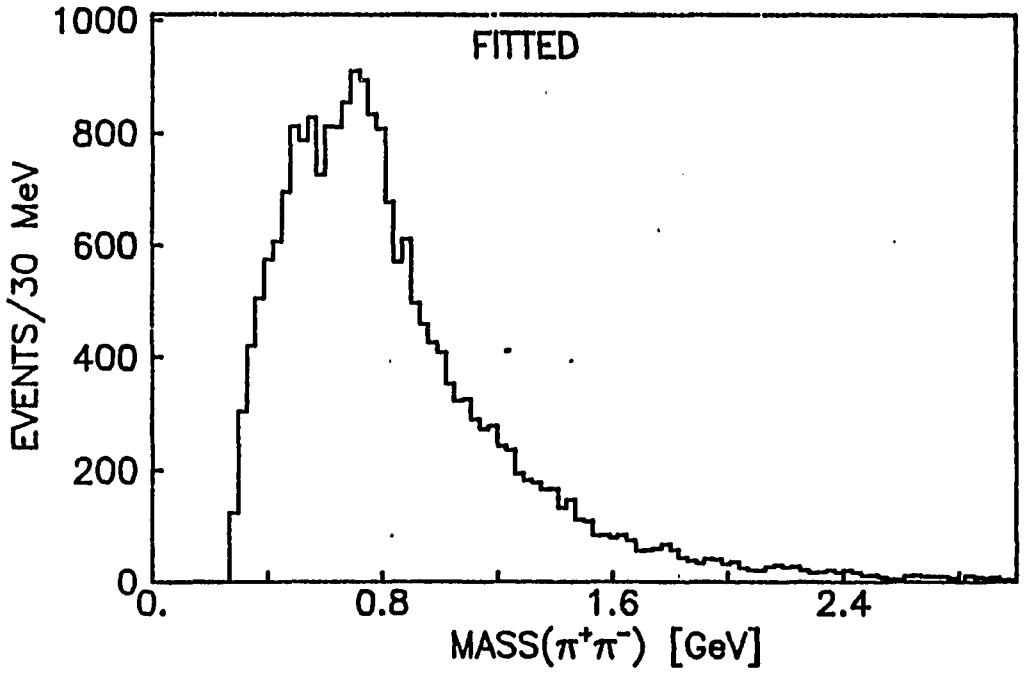

Figure 6.5. Mass distribution for $\pi^+\pi^-$ pairs in the four pion system (four combinations per event)

the four particle central system for DPE events. The total four pion system must still have $J^{PC} = 0^{++},2^{++},4^{++}$,etc., but pion pairs within this system may still combine to form other spin-parity states such as the ρ^0.

The ρ^0 enhancement immediately calls to mind the studies of the interaction of two photons ($\gamma\gamma$) in e^+e^- collisions where a large $\rho^0\rho^0$ enhancement is seen in the four pion system. This process is topologically very similar to the DPE process shown in Figure 1.5(c) except that the incoming and outgoing fast peripheral protons are replaced by an e^+ and an e^- and the pomerons are replaced by photons. Since the photon is a spin one object, spin-parity states with odd L (and thus negative parity) are allowed in the central system formed by the $\gamma\gamma$

interaction that are not allowed in DPE; however, no J=1 states are allowed and the C-parity must be even. To examine the data for a $\rho^0\rho^0$ enhancement, the mass of one $\pi^+\pi^-$ pair is plotted versus the mass of the other $\pi^+\pi^-$ pair in Figures 6.6-7 for different ranges of the four pion mass (two entries per event). The wrong charge combinations are plotted in Figures 6.8-9 for comparison (i.e., the mass of the $\pi^+\pi^+$ pair versus the mass of the $\pi^-\pi^-$ pair, one entry per event). In each case, the pair with the higher mass is plotted along the x-axis, and the pair with the lower mass is plotted along the y-axis. The mass distributions of the $\pi^+\pi^-$ pairs for these same ranges of the four pion mass are shown in Figures 6.10-11.

From Figures 6.6-7 one can see that the data do not show a strong $\rho^0\rho^0$ enhancement as seen in $\gamma\gamma$ data [Althoff et al. 1982, Behrend et al. 1984]. The four pion mass distribution is shown in Figure 6.12 for events that were consistent with a $\rho^0\rho^0$ pair in the central region (i.e., $pp \rightarrow ppX$, $X \rightarrow \rho^0\rho^0 \rightarrow (\pi^+\pi^-)(\pi^+\pi^-)$). A $\pi^+\pi^-$ pair was considered consistent with a ρ^0 if $0.620 < M(\pi^+\pi^-) < 0.920$ GeV. There are 1,268 events contained in this plot (23.8% of the total number of events).

In Figure 6.13 the four pion mass distribution is shown for events which were consistent with at least one ρ^0 in the central region (i.e., $pp \rightarrow ppX$, $X \rightarrow \rho^0\pi^+\pi^- \rightarrow (\pi^+\pi^-)\pi^+\pi^-$). Note that Figure 6.12 is a subset of this plot. No clear enhancement is seen in Figure 6.13, but the shoulder around 1.3 GeV remains evident in the mass spectrum. This plot contains 4,304 events (80.9% of the total number of events). Without a careful analysis, these plots by themselves do not allow us to determine how much of the central system consists of $\rho^0\rho^0$ decay, how much consists of $\rho^0\pi^+\pi^-$

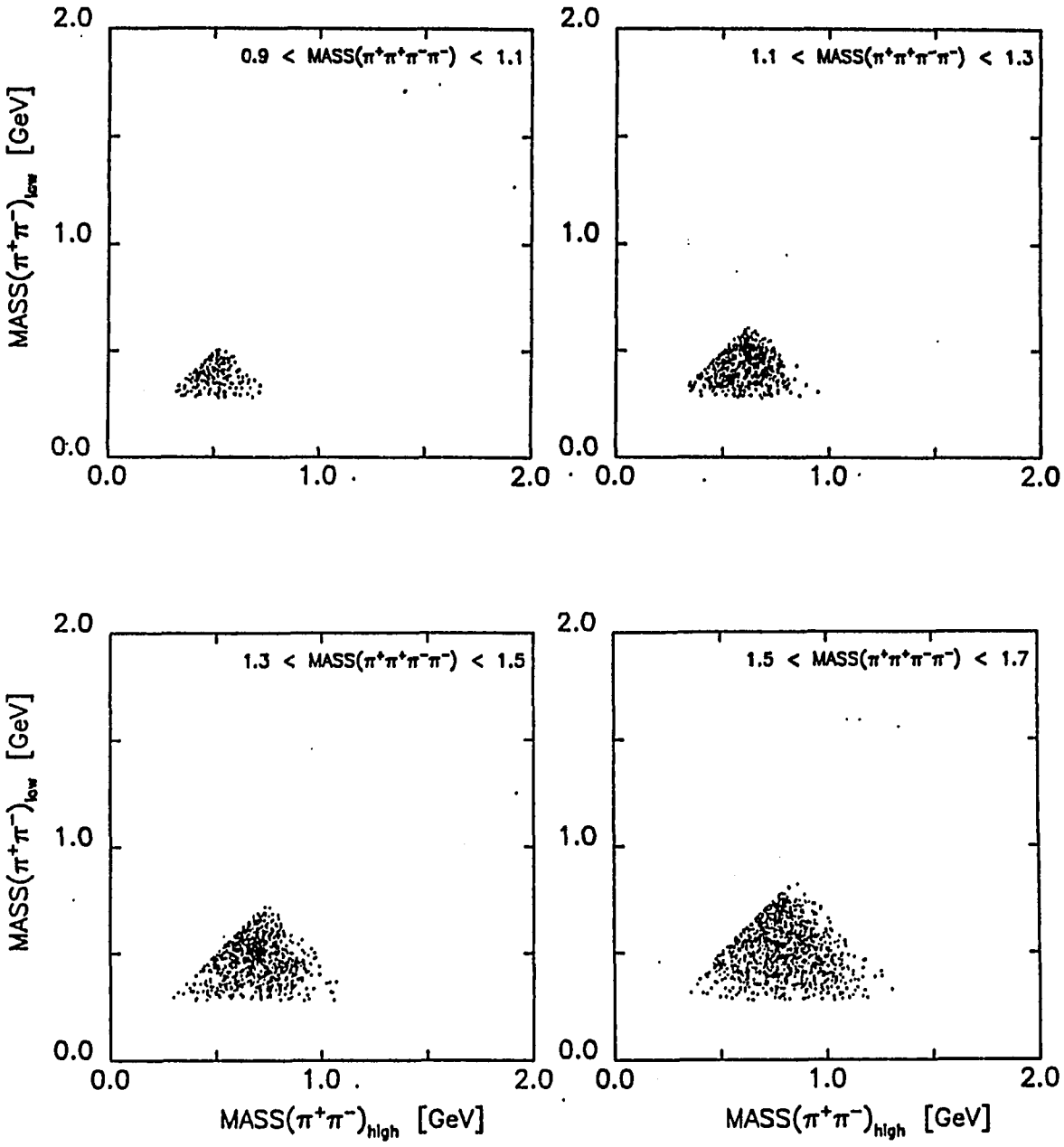

Figure 6.6. Scatterplots of the mass of $\pi^+\pi^-$ pairs for different ranges of the four pion mass where the higher mass is plotted along the x-axis and the lower mass is plotted along the y-axis

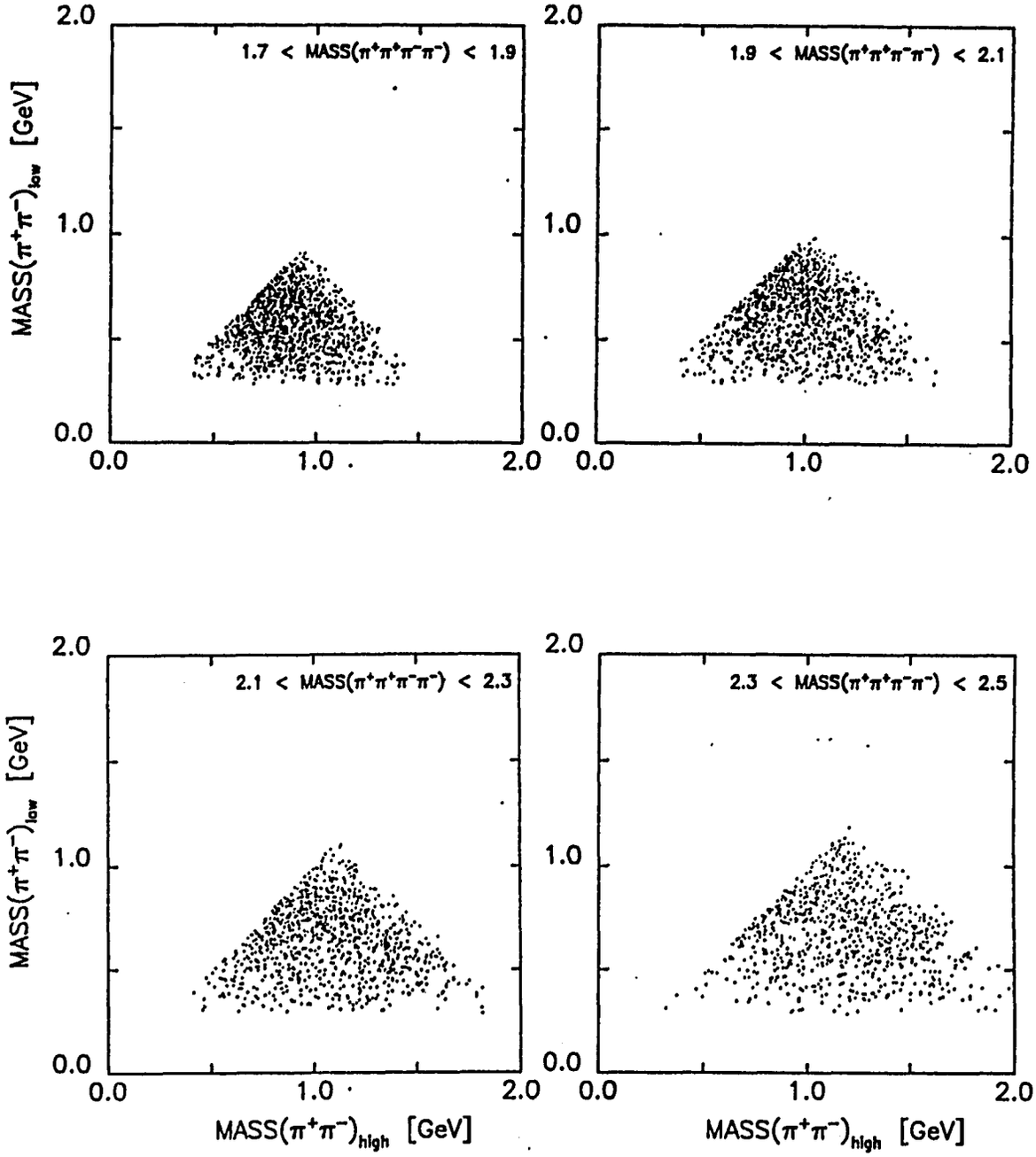

Figure 6.7. Scatterplots of the mass of $\pi^+\pi^-$ pairs for different ranges of the four pion mass where the higher mass is plotted along the x-axis and the lower mass is plotted along the y-axis

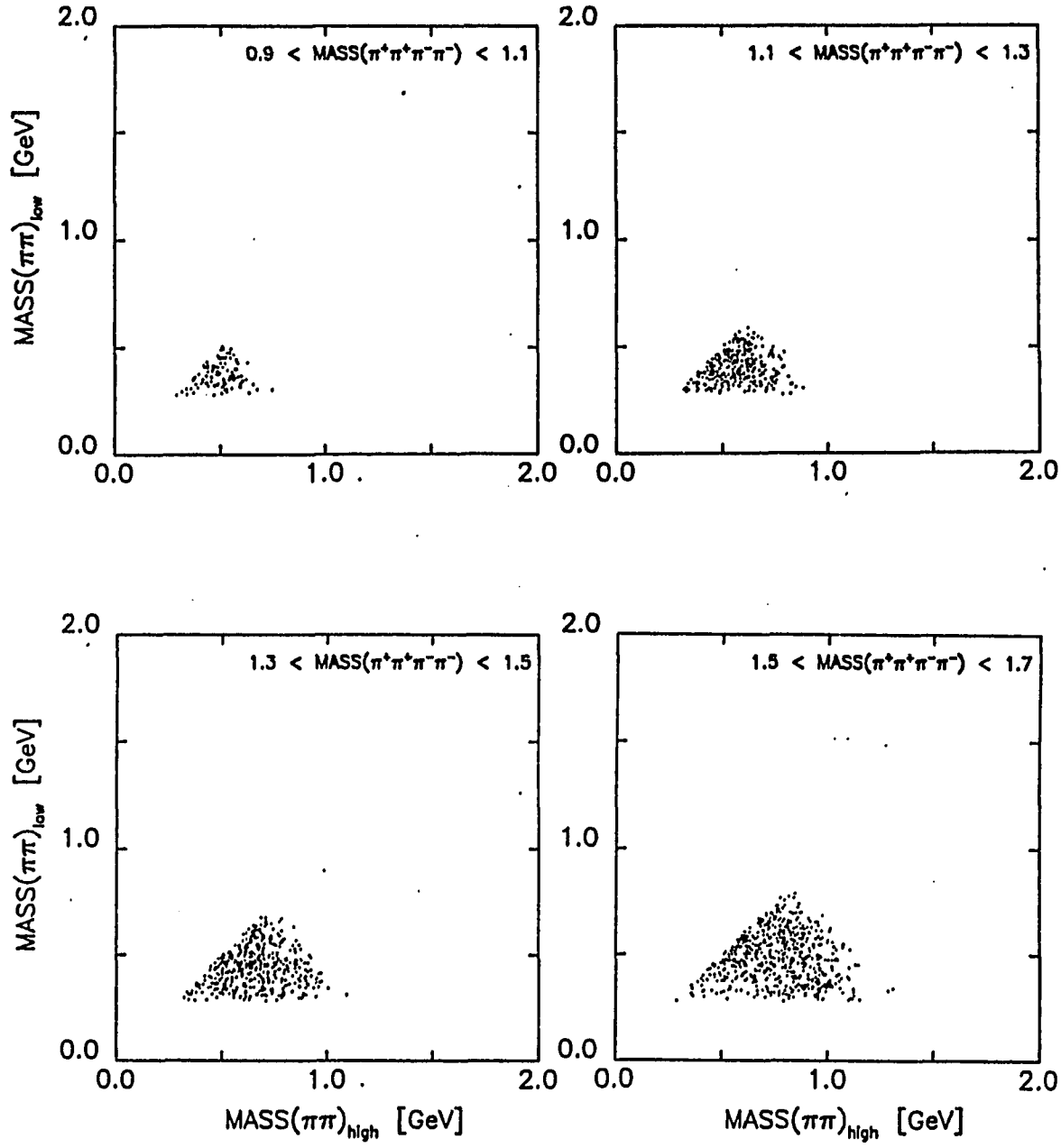

Figure 6.8. Scatterplots of the mass of exotic ππ (charge=2) pairs for different ranges of the four pion mass where the higher mass is plotted along the x-axis and the lower mass is plotted along the y-axis

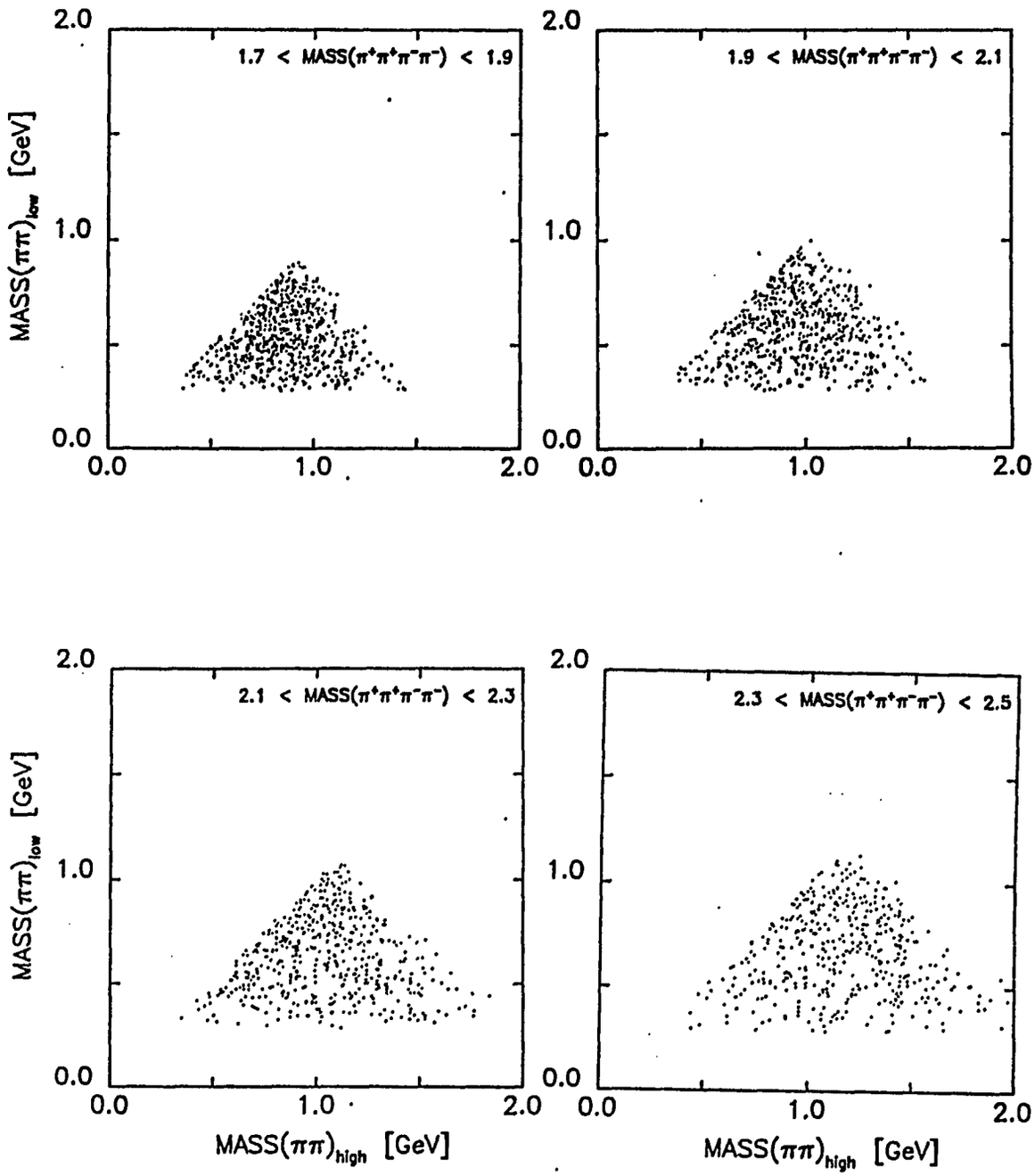

Figure 6.9. Scatterplots of the mass of exotic ππ (charge=2) pairs for different ranges of the four pion mass where the higher mass is plotted along the x-axis and the lower mass is plotted along the y-axis

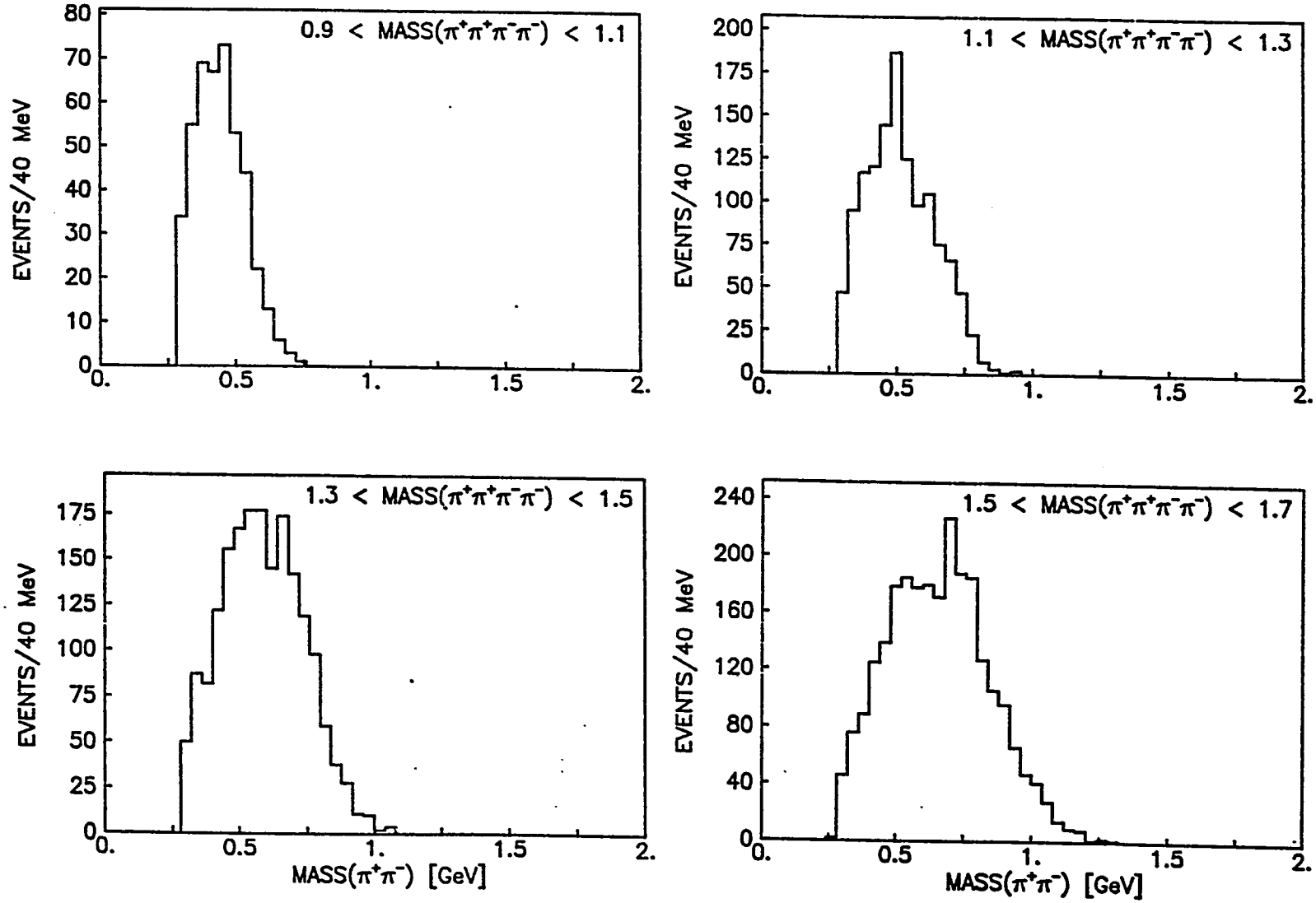

Figure 6.10. Mass of $\pi^+\pi^-$ pairs for the same four pion mass ranges as in Fig. 6.6 (i.e. sum of projections of plots in Figure 6.6)

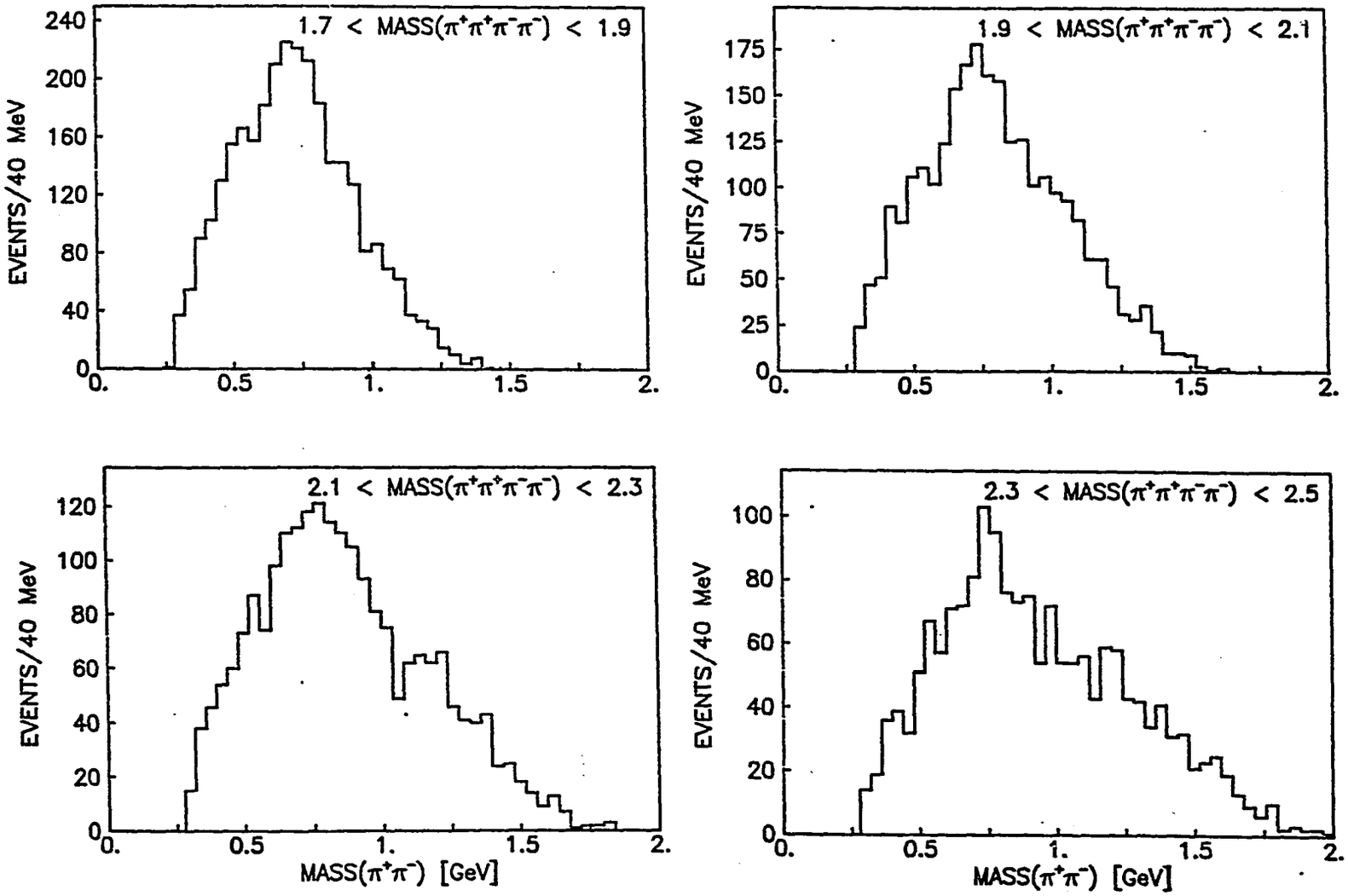

Figure 6.11. Mass of $\pi^+\pi^-$ pairs for the same four pion mass ranges as in Fig. 6.7 (i.e. sum of projections of plots in Figure 6.7)

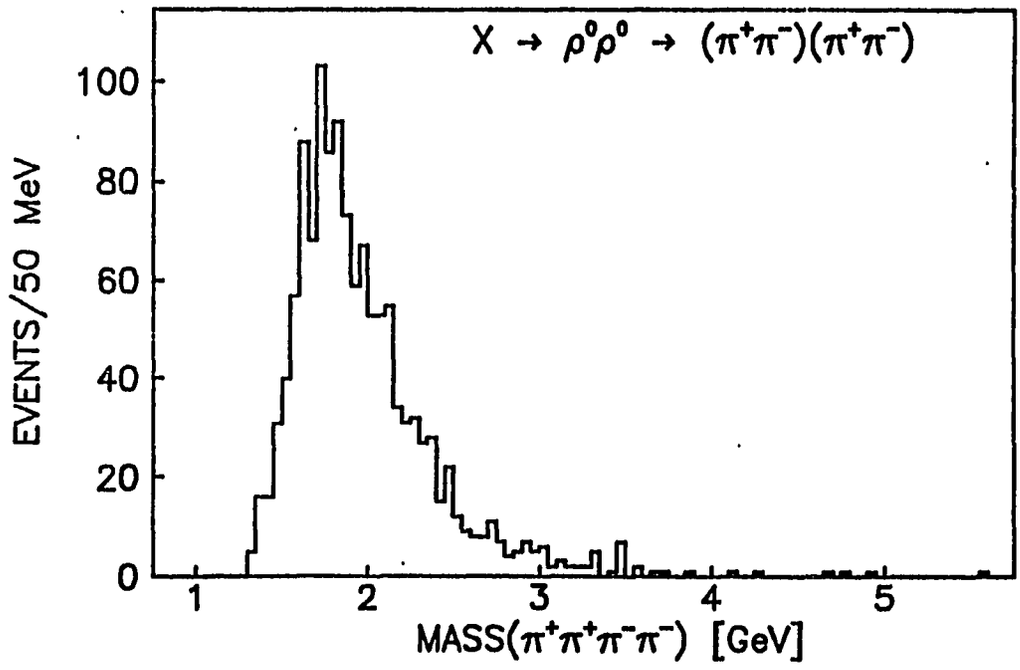

Figure 6.12. Four pion mass for events consistent with central system coming from the decay of two neutral rho mesons

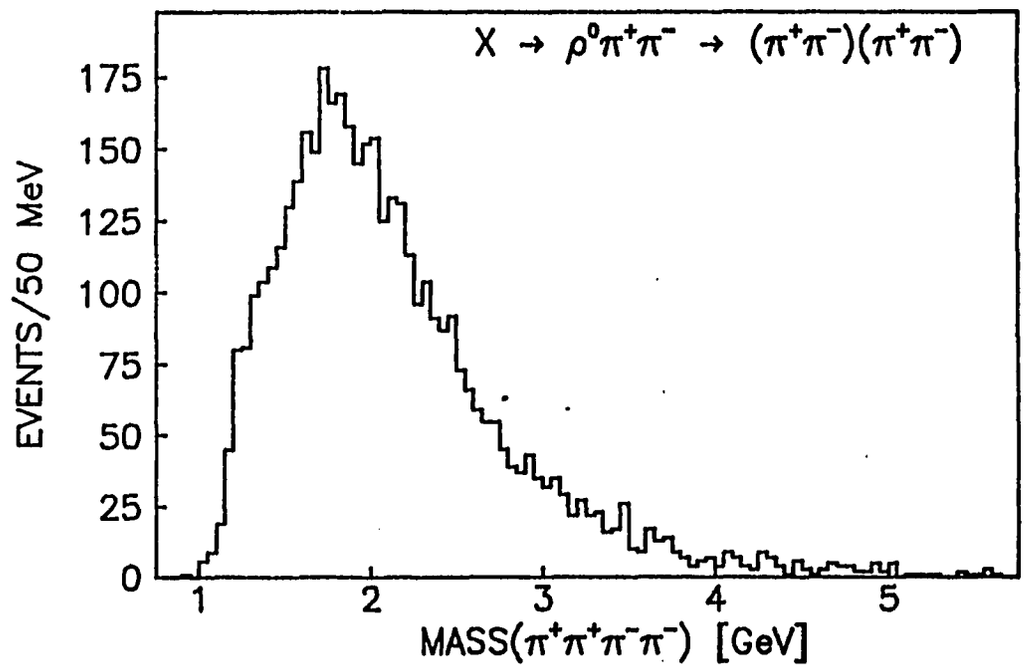

Figure 6.13. Four pion mass for events consistent with central system coming from the decay of one neutral rho meson accompanied by a $\pi^+\pi^-$ pair

decay and how much consists of $\pi^+\pi^+\pi^-\pi^-$ decay, where the pions are described by phase space.

Before any fitting could be done for how much each of these subprocesses are needed to describe the data, it was necessary to calculate the acceptance of the SFM for the six prong OR trigger. The procedure to calculate the SFM acceptance has been described in Chapter 4 for the four prong events. The only difference for six prong events is that there are four particles to generate in the central system, rather than just two.

Also, it was decided that the additional corrections which used the correlations of the projected angles in the x-z plane for the leading protons described in Section 4.2 would not be performed for the six prong data. The introduction of this correction would reduce the statistical power of the events generated by Monte Carlo enough such that the gains made in fitting the data would be lost by the fluctuations caused by this correction. The simulated events were generated for the central four pion masses of 0.9 to 1.6 GeV in 100 MeV intervals and from 1.8 to 5.0 GeV in 200 MeV intervals. Only these mass values were generated due to the large amount of processing necessary on a computer to accomplish this task (i.e., each mass value takes roughly 20 hrs on a VAX 11/785 computer).

In order to fit the two-dimensional distributions of the two pion mass combinations, it was decided to bin the scatterplots so that a chi-square minimization approach could be used. The Monte Carlo generated events were used to generate three separate two-dimensional histograms for the three different hypotheses given above. This was done by generating one histogram with just the four pion phase space, a second one with the

event weight multiplied by the square of a Breit-Wigner amplitude for a single ρ^o, and a third one with the event weight multiplied by the ρ^o Breit-Wigner intensity applied twice, once for each $\pi^+\pi^-$ pair. Specifically the weights were:

$$W_{4\pi} = W_{ps}$$
$$W_{\rho\pi\pi} = W_{ps}\, W_{BW}$$
$$W_{\rho\rho} = W_{ps}\, W_{BW}\, W_{BW}$$

where in terms of the mass m of the $\pi^+\pi^-$ pair making up the ρ^o:

$$W_{BW} = |BW(m)|^2 = \frac{M_\rho \Gamma}{(M_\rho^2 + m^2) + M_\rho^2 \Gamma^2}$$

with

$$\Gamma = \Gamma_\rho \left(\frac{p^*}{p_o^*} \right)^3 \frac{2p_o^{*2}}{p_o^{*2} + p^{*2}}, \quad p^{*2} = \frac{1}{4}(m^2 - 4M_\pi^2), \quad p_o^{*2} = \frac{1}{4}(M_\rho^2 - 4M_\pi^2)$$

and m_ρ = 776 MeV, m_π = 139.57 MeV, Γ_ρ = 154 MeV [Wohl et al. 1984]. It should be recalled from Chapter 4, that the W_{ps} term includes the corrections for the SFM's limited geometrical acceptance.

Once these three histograms were formed using the Monte Carlo data, one could then minimize the chi-square distribution given by:

$$\chi^2 = \sum_{i=1}^{N} (n_i - a n_i^{4\pi} - b n_i^{\rho\pi\pi} - c n_i^{\rho\rho})^2 / \sigma_i^2$$

where the sum is over the number of bins populated by the data with n being the number of events occurring in each bin of the respective two-dimensional histograms, a, b, c are the relative fractions of the four pions in the central system produced by 4π phase space, ρ^o plus 2π phase space, and $\rho^o\rho^o$, respectively. The error used was the statistical error on the data.

This chi-square was calculated for different fractions a, b, and c in 200 MeV bins for the mass of the four pion central system between 0.9 and 2.5 GeV (i.e., the same mass ranges as shown in Figures 6.6-7). Before fitting, the data were subjected to the same cuts as in the Monte Carlo data used to calculate the acceptance of the SFM. This reduced the number of events to 4,921. The value of the chi-square was plotted and the minimum value was found by eye. The error was calculated for a change in the χ^2 value by one unit. The results are given in Table 6.1.

A note is in order here about the high values for the $\rho^o\rho^o$ term at low masses. It appears to come about due to the discrete nature of the Monte Carlo data and the fact that at low mass the four pion mass spectrum is rapidly increasing. At the lower four pion masses one is far enough

Table 6.1. Fractions of $\rho^o\rho^o$, $\rho^o\pi^+\pi^-$, and $\pi^+\pi^-\pi^+\pi^-$ phase space for the process $pp \rightarrow pp\pi^+\pi^-\pi^+\pi^-$

Mass(4π) [GeV]	4π ps (a)	$\rho\pi\pi$ (b)	$\rho\rho$ (c)	χ^2/d.f.
0.9<M<1.1	0.72 ±0.30	0.00 ±0.17	0.28 ±0.25	0.8
1.1<M<1.3	0.68 ±0.13	0.03 ±0.10	0.29 ±0.09	1.3
1.3<M<1.5	0.43 ±0.11	0.23 ±0.10	0.34 ±0.05	1.6
1.5<M<1.7	0.45 ±0.09	0.55 ±0.07	0.00 ±0.03	1.5
1.7<M<1.9	0.44 ±0.08	0.51 ±0.06	0.05 ±0.03	1.4
1.9<M<2.1	0.49 ±0.06	0.51 ±0.06	0.00 ±0.02	0.9
2.1<M<2.3	0.60 ±0.11	0.36 ±0.10	0.04 ±0.04	0.8
2.3<M<2.5	0.75 ±0.12	0.17 ±0.11	0.08 ±0.04	0.6

from the minimum energy needed to produce this pair, so that even with the large width of the ρ^0, the $\rho^0\rho^0$ channel should not give such a large contribution to the data. This hypothesis was confirmed by generating Monte Carlo events in small mass intervals between 1.1 and 1.3 GeV and refitting the data. The result of this was that a value near zero would be more in line with what the data will support. Another reason for this conclusion was the study of the projections of the high and low mass $\pi^+\pi^-$ pairs from Figures 6.6-7 separately. The ρ^0 signal that appears in the $\pi^+\pi^-$ spectrum first appears in the high $\pi^+\pi^-$ mass spectrum and then shifts over to the low $\pi^+\pi^-$ mass spectrum, never appearing in both projections very strongly. From the Monte Carlo model, a $\rho^0\rho^0$ signal would appear in both projections very strongly at the same time. In the region of the four pion mass below 1500 MeV, the data clearly cannot support the presence of a ρ^0 signal in the low $\pi^+\pi^-$ mass spectrum.

6.3. Simple Spin-Parity Analysis

A simple spin-parity analysis for a four particle decay is to study the distribution of the angle between the plane formed by the $\pi^+\pi^+$ pair and the plane formed by the $\pi^-\pi^-$ pair. The advantage of this angle is that it can be defined unambiguously for the six prong events. Specifically, the cosine of this angle is defined by:

$$\cos\psi = n_1 \cdot n_2 / |n_1||n_2|$$

where:

$$n_1 = p_{\pi^+} \times p_{\pi^+}$$

$$n_2 = p_{\pi^-} \times p_{\pi^-}$$

Due to various symmetry requirements, the distribution of this angle will have different forms for different spin-parity states [Nyborg and Skjeggestad 1968]. This analysis was performed for the same values of the four pion mass as the various mass plots discussed in Section 6.2. Since pions of the same charge are indistinguishable bosons, one has the ambiguity of which way to point the normal to the plane formed by the pion pairs. Thus, any angular distributions can not depend on which way one chooses, and therefore $|\cos\psi|$ is the interesting quantity to study. Table 6.2 gives the expected dependence of the cross sections, with respect to the angle ψ, for different J^{PC} states [Nyborg and Skjeggestad 1968]. In the case of $J^P = 2^-$ the sign of the $\cos^2\psi$ term cannot be found, so it remains ambiguous with the 2^+ state and the 1^+ and 3^- states.

The dependence of the data on ψ is plotted in Figures 6.14-15 for the same 200 MeV mass intervals studied in the previous section. Also shown

Table 6.2. Cross section angular dependence on ψ

J^{PC}	$f(\cos\psi)$
$0^+,1^-$	constant
0^-	$a^2(1-\cos^2\psi)$
$1^+,3^-$	$a^2-b^2\cos^2\psi$
2^+	$a^2+b^2\cos^2\psi$
2^-	$a^2+b\ \cos^2\psi$

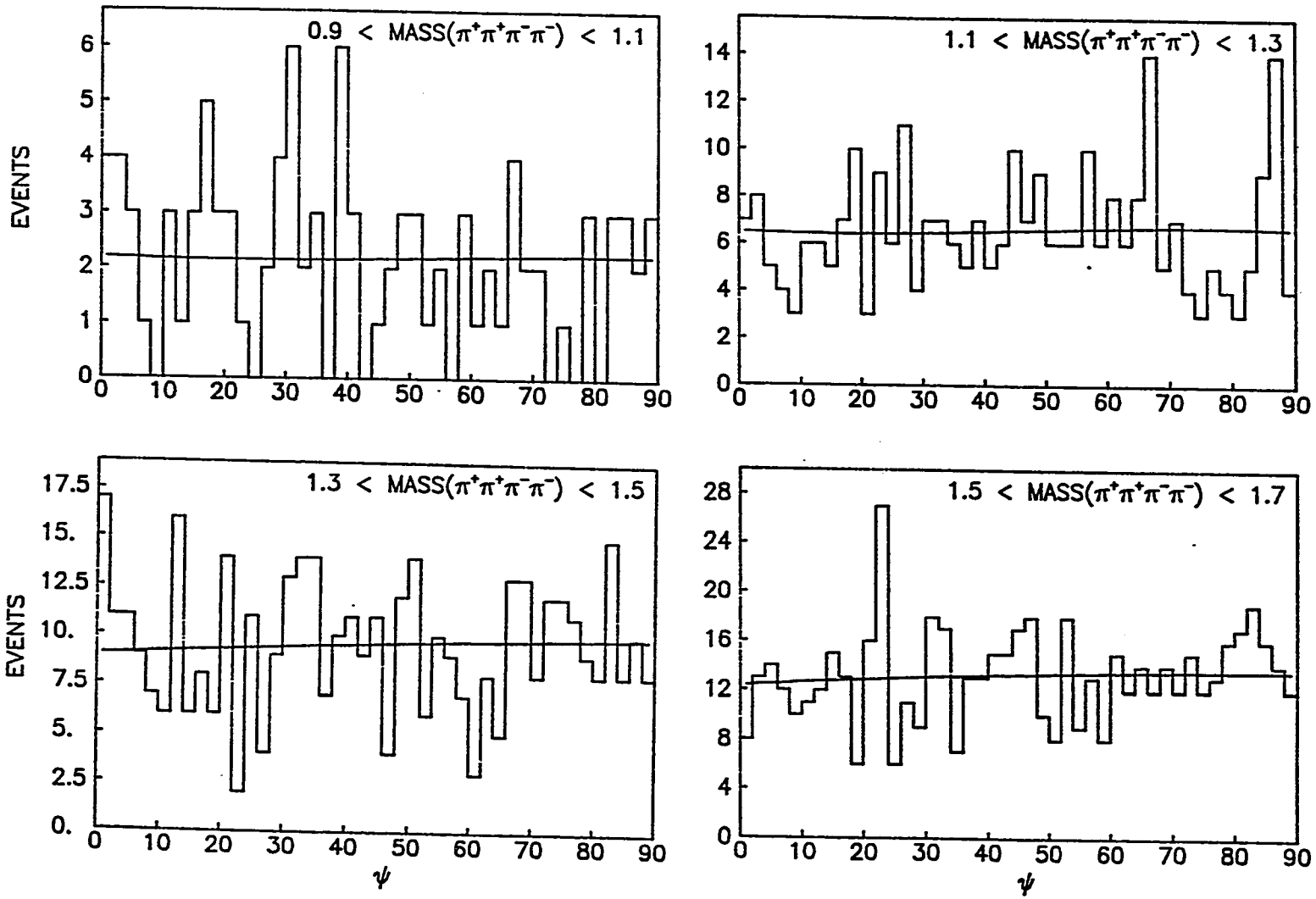

Figure 6.14. Distribution of the angle between the two planes formed by like charge pions (solid line is Monte Carlo prediction calculated for the geometrical acceptance of the SFM)

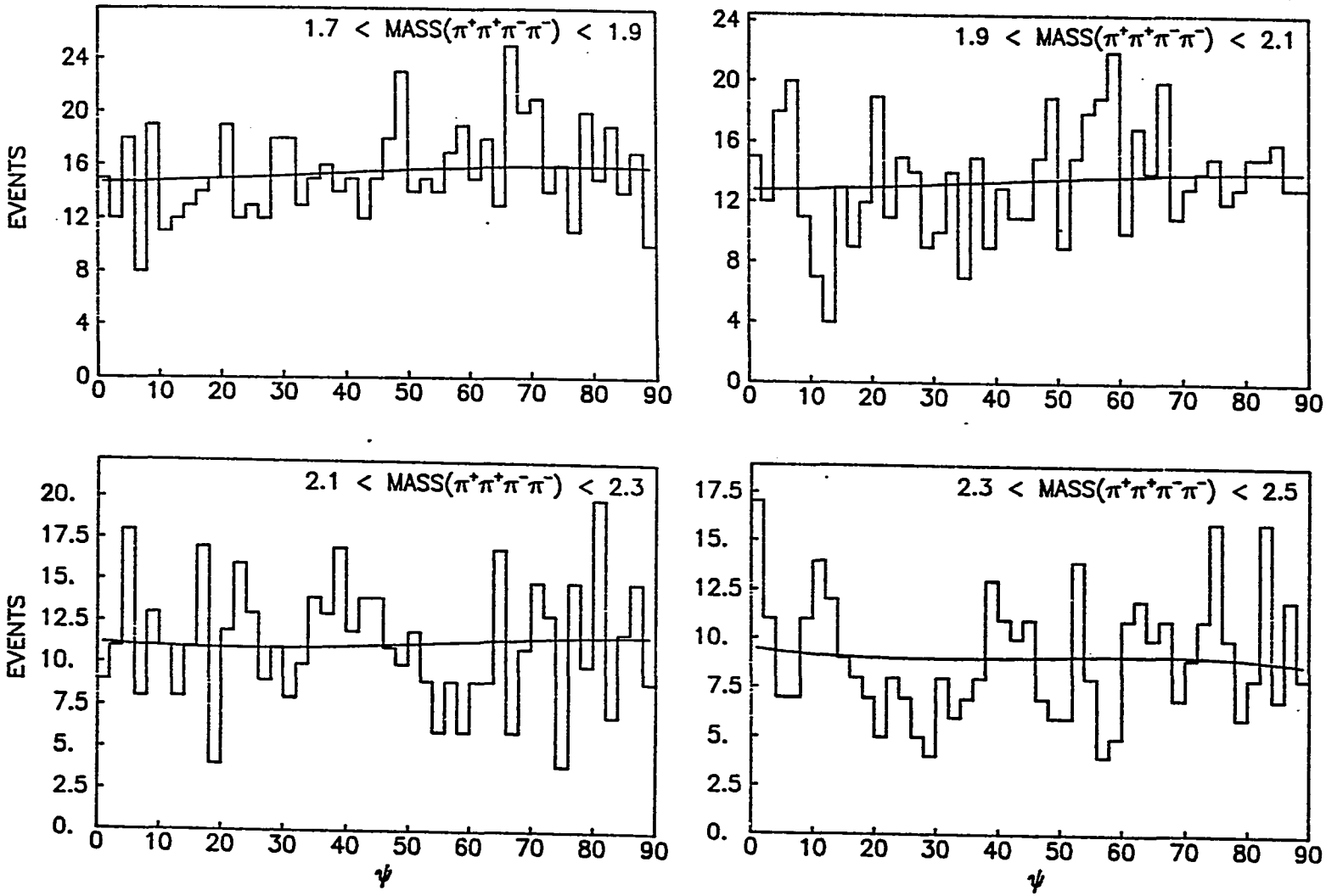

Figure 6.15. Distribution of the angle between the two planes formed by by like charge pions (solid line is Monte Carlo prediction calculated for the geometrical acceptance of the SFM)

on the plots, is the expected distribution of the angle calculated using the same Monte Carlo events used in the previous section. The angle is folded since the cross sections only depend on $|\cos\psi|$. The data show no structure with repect to this angle. Thus, either all of the data were created in a S-wave state (note that the Monte Carlo predictions are consistent with the data), or the SFM detector is not sensitive to the cross sectional dependence on this angle.

6.4. Conclusions

The six prong OR data show some evidence of structure around the central four pion mass value of 1.3 GeV; however, this enhancement is not strong enough to lend itself to an analysis to determine its source or even if it is a real effect. There is a clear signal for the central system containing a single ρ^o above the central four pion mass value of 1.3 GeV, but little or no convincing evidence of any $\rho^o\rho^o$. This result is markedly different than in the case of $\gamma\gamma$ experiments in e^+e^- collisions. The importance of this result is that the photons in the $\gamma\gamma$ experiments interact only through quarks and the Pomerons in DPE are expected to interact primarily through the interaction of gluons.

A simple spin-parity analysis elucidates little on the central system as to what states are being created. The angle selected to study shows little structure as a function of the four pion mass.

7. SIX PRONG "AND" DATA ANALYSIS

7.1. Final Cuts on Data

The six prong events recorded with the AND trigger are essentially a subset of the six prong OR data as explained in Section 2.3. The similarities of these two data samples are much greater than in the four prong case. This is true because the AND trigger has a higher average charge multiplity, so the higher the multiplicity of the OR data, the more likely it would be to satisfy the AND trigger. However, there is still too great of a difference in the events to combine the data samples. Here, as in Chapter 5, redundant explanations will be kept to a minimum, so Chapter 6 should be referenced for the details of the analysis.

Of the 406,356 events taken with the AND trigger which were successfully processed and stored on a DST, 48,180 of them consisted of six outgoing tracks which were found to come from a common vertex. After the same cuts as described in Chapter 4, i.e., charge balance, and $0.55 < x_F < 1.8$ for the outgoing fast leading protons, 32,429 six prong events remained to be subjected to the 4C-fit procedure described in Chapter 3.

The probability-of-fit value cut for this data was set at 0.20, as in the six prong OR data, since the probability-of-fit distribution does not fall as rapidly for low probability values in this case as it does in the four-prong case. The probability-of-fit distribution is shown in Figure 7.1. For this cut on the probability-of-fit value, the data were studied to be sure that the probability distribution was a reasonable representation of the amount of background being included by the chosen

cut placed on this quantity and to be sure that such a stringent cut on this value was necessary. By studying the mass distribution of the four pion central system with cuts in intervals of 0.02 for the probability-of-fit around the 0.20 cut, it was decided that by cutting below 0.20 one would be allowing an unacceptable amount of background (i.e., events that were not consistent with energy and momentum conservation).

A cut was placed on the value of x_F calculated from the fitted track parameters for the two fast leading protons, requiring them to have $x_p > 0.8$, as in the six prong OR data. Also, as in the six pring OR data, the majority of the events in the six prong AND data have all four of their central particles consisting of pions. Thus, any events that have TOF information inconsistent with this hypothesis are rejected. After these

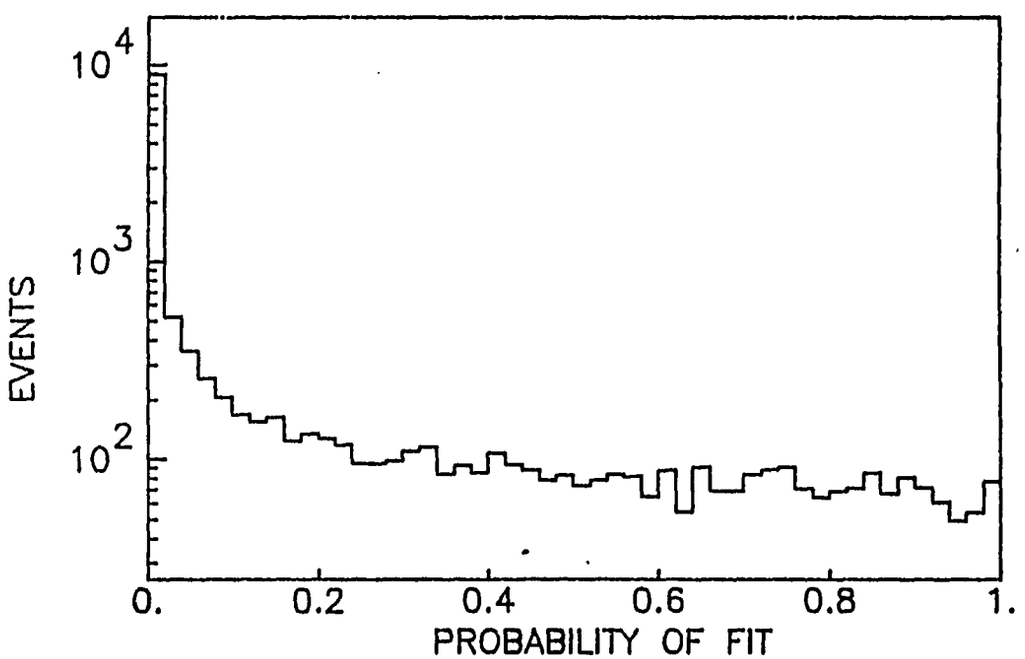

Figure 7.1. Probability-of-fit distribution for the 4C-fit

two cuts and the cut on the probability-of-fit value, the number of events was reduced to 3,267.

For these data, the plot of x_F of one fast leading proton versus x_F of the other proton is very similar to Figure 6.3, so it is not shown here. The data also clearly show the double-pole structure expected for DPE events. The plots of the correlation of the azimuthal angles and momentum transfer of one fast leading proton with the other are very similar to the four prong data and are not shown here. Figure 7.2 shows the invariant mass distributions of the four particle central system for the six prong AND data using the unfitted (Figure 7.2(a)) and fitted (Figure 7.2(b)) track parameters. No unambiguous structure is apparent in the fitted mass distribution. As in the case of the OR data, there is some evidence for structure around 1.3 GeV because of the possible shoulder in the plot; however, due to the lower statistics, this claim is uncertain.

7.2. Study of the Four Pion Central State

With no clear structure in the mass distribution of the four pion central system, the same subprocesses as in Section 6.2 will be examined to search for enhancements in the data. The mass distribution of $\pi^+\pi^-$ pairs in the four pion central system is shown in Figure 7.3 (four combinations per event). There is a clear enhancement in the region of the ρ^0 meson (m = 770 MeV, Γ = 156 MeV, $J^{PC} = 1^{--}$), just as in the six prong OR data. There is also a possible slight enhancement in the region of the f^0 meson (m = 1274 MeV).

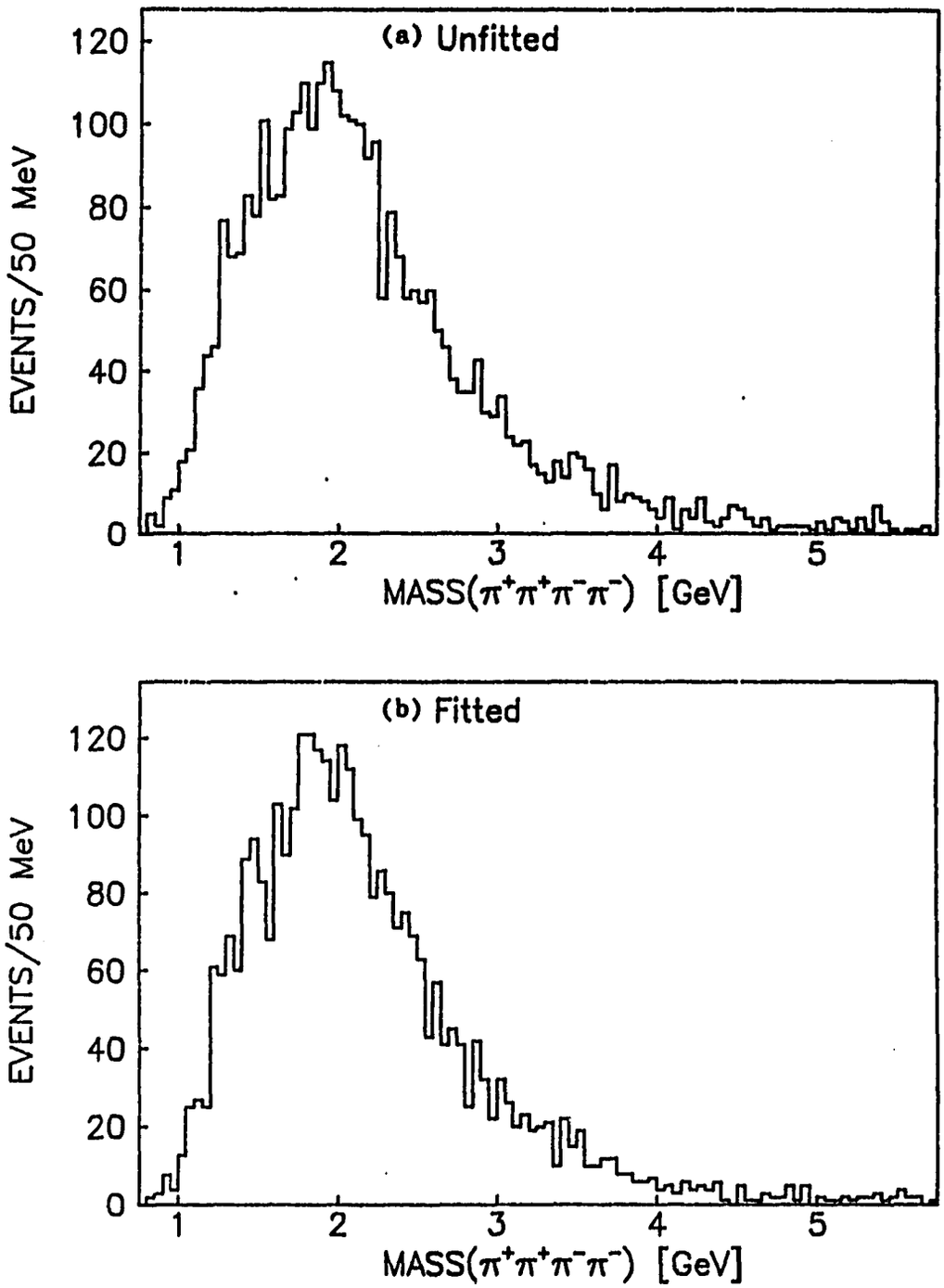

Figure 7.2. Mass distribution for central $\pi^+\pi^+\pi^-\pi^-$ system using (a) measured (unfitted) track parameters and (b) fitted track parameters

As in the case of the six prong OR data, the ρ^0 enhancement immediately calls to mind the studies of the interaction of two photons ($\gamma\gamma$) in e^+e^- collisions where a large $\rho^0\rho^0$ enhancement is seen in the four pion system. Thus, the study explained in Section 6.2 is repeated here for the AND data.

To examine the data for such an enhancement, the mass of one $\pi^+\pi^-$ pair is plotted versus the mass of the other $\pi^+\pi^-$ pair in Figures 7.4-5 for different ranges of the four pion mass (two entries per event). The pair with the higher mass is plotted along the x-axis, and the pair with the lower mass is plotted along the y-axis. The masses of the $\pi^+\pi^-$ pairs are shown in Figures 7.6-7 for each of the same mass ranges as in Figures

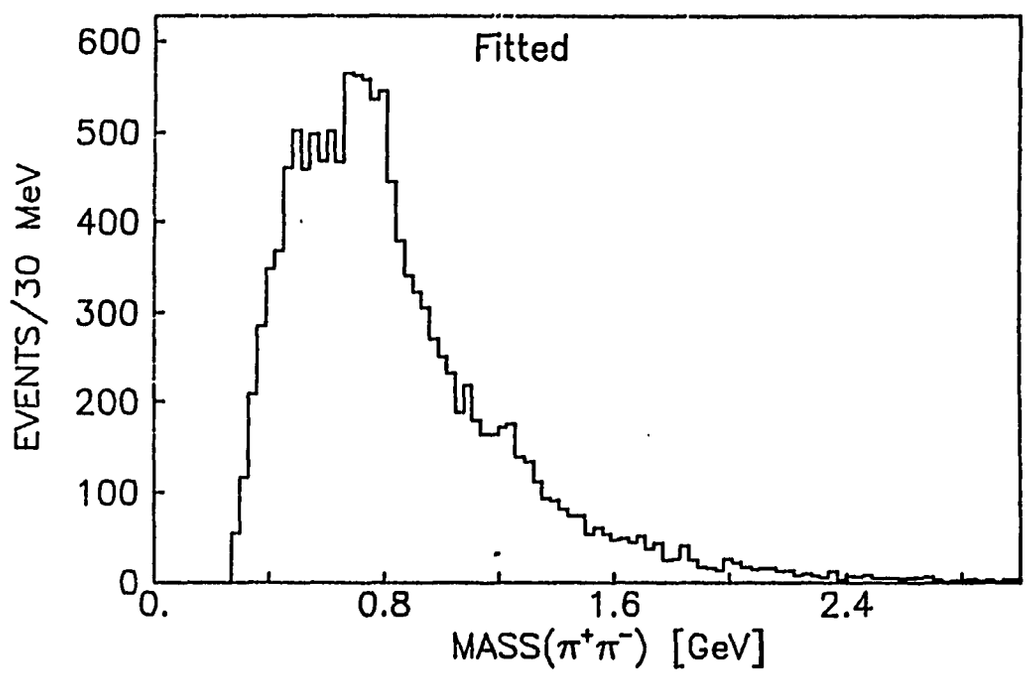

Figure 7.3. Mass distribution for $\pi^+\pi^-$ pairs in the four pion system (four combinations per event)

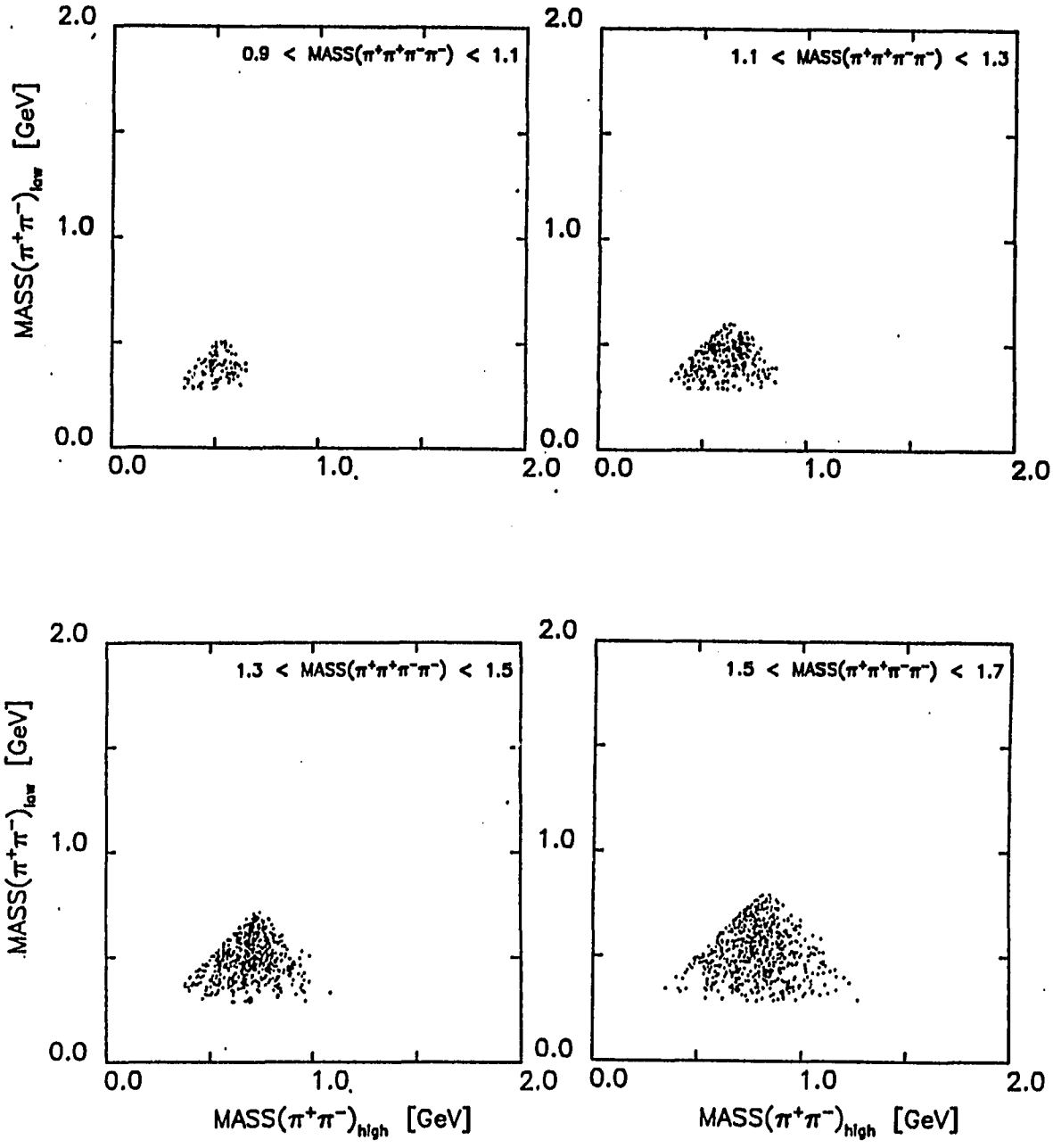

Figure 7.4. Scatterplots of the mass of $\pi^+\pi^-$ pairs for different ranges of the four pion mass where the higher mass is plotted along the x-axis and the lower mass is plotted along the y-axis

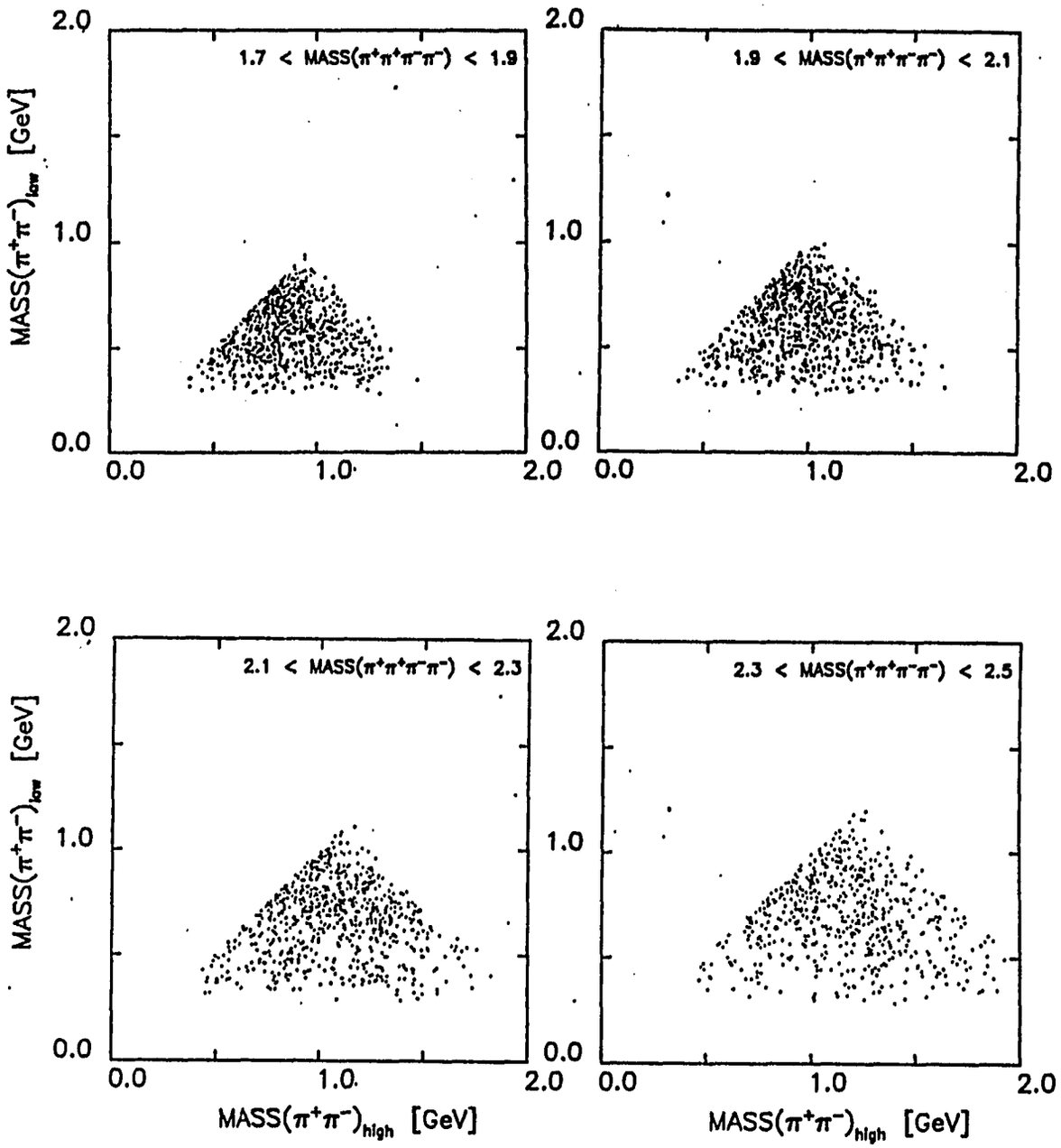

Figure 7.5. Scatterplots of the mass of $\pi^+\pi^-$ pairs for different ranges of the four pion mass where the higher mass is plotted along the x-axis and the lower mass is plotted along the y-axis

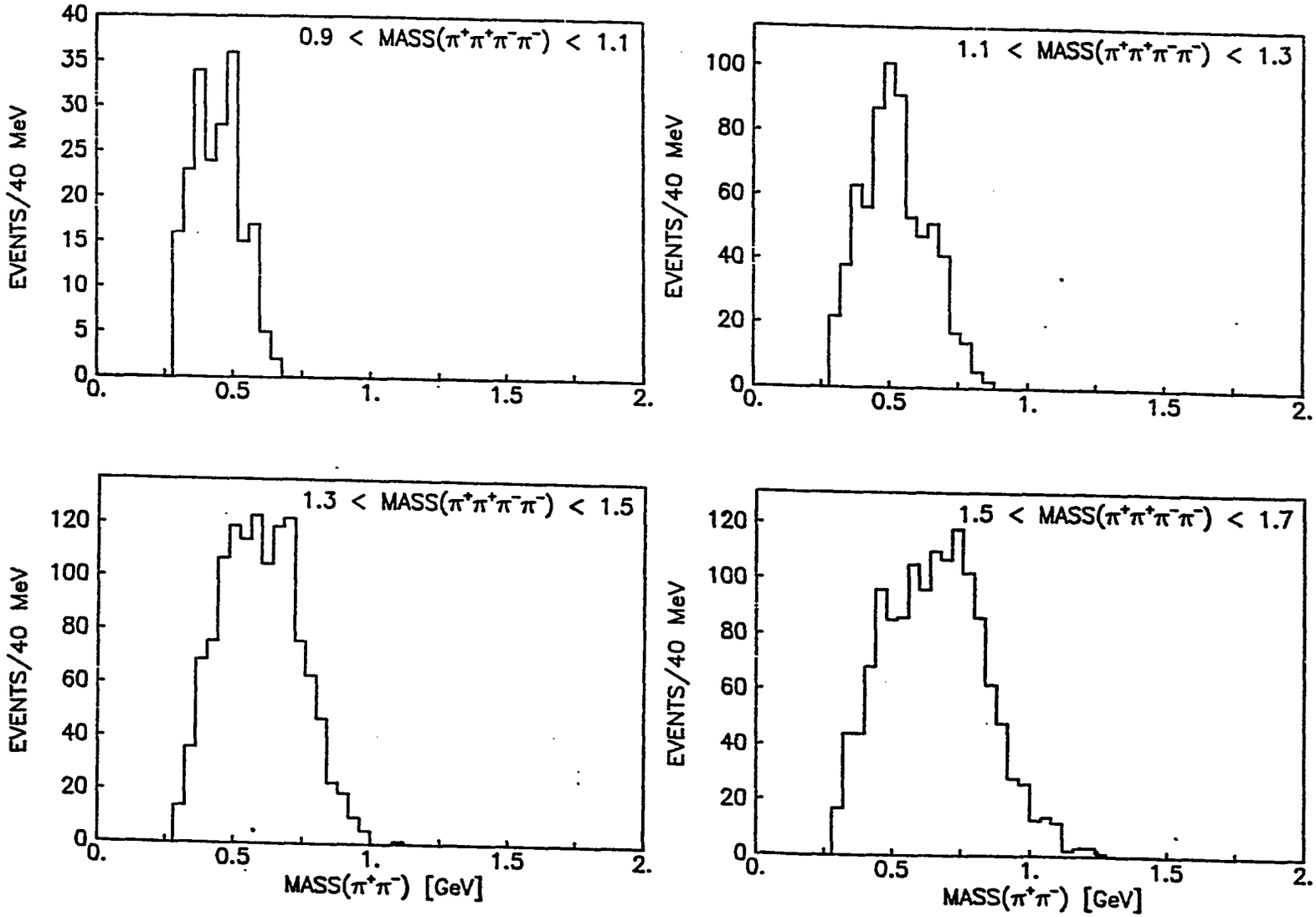

Figure 7.6. Mass of $\pi^+\pi^-$ pairs for the same four pion mass ranges as in Fig. 7.4 (i.e. sum of projections of plots in Figure 7.4)

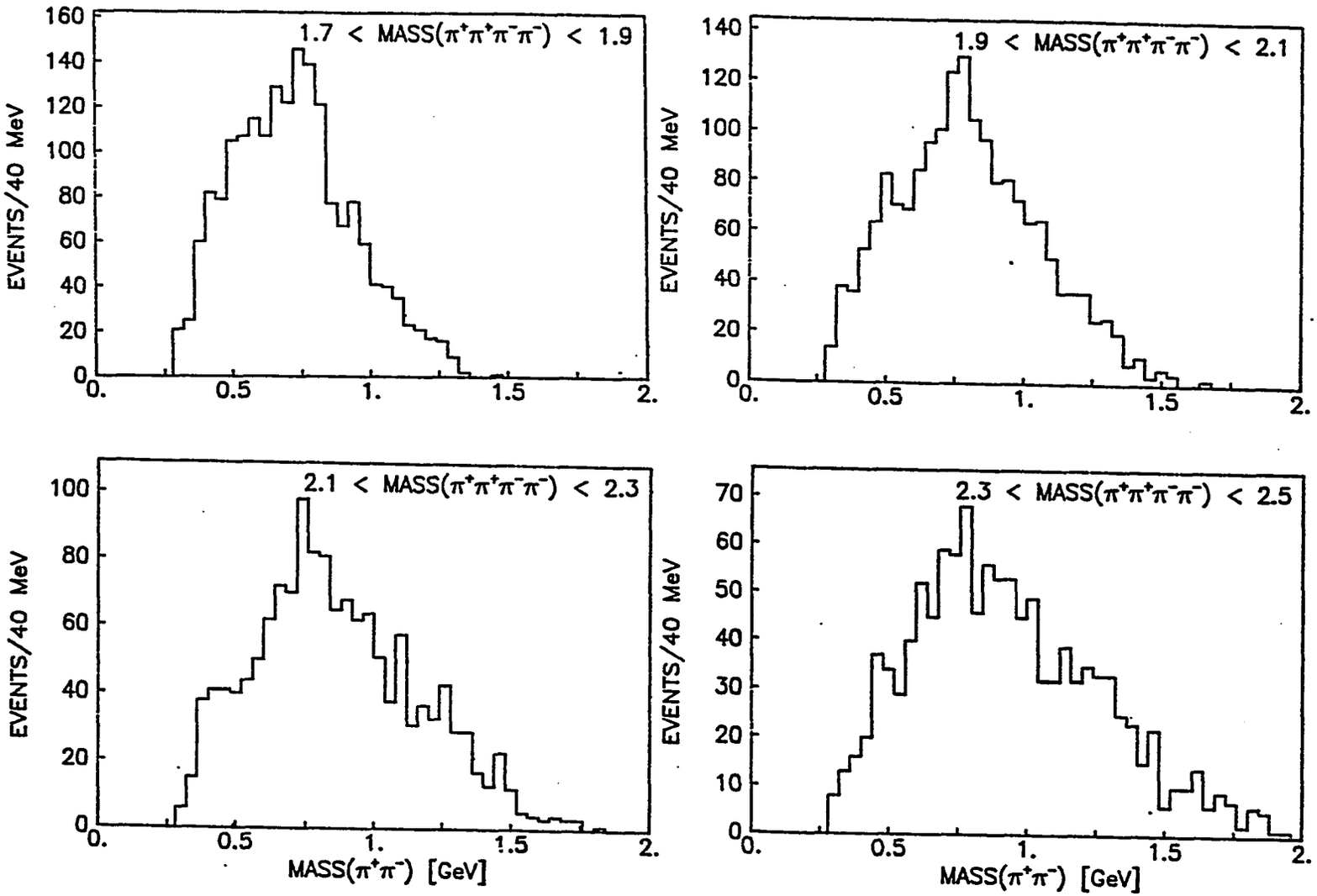

Figure 7.7. Mass of $\pi^+\pi^-$ pairs for the same four pion mass ranges as in Fig. 7.5 (i.e. sum of projections of plots in Figure 7.5)

7.4-5. The four pion mass ranges are the same as those used for the OR data.

From Figures 7.4-5, one can see that the data do not show a strong $\rho^o\rho^o$ enhancement as seen in $\gamma\gamma$ data [Althoff et al. 1982, Behrend et al. 1984]. This is the same as in the six prong OR data. The four pion mass distribution is shown in Figure 7.8 for events that were consistent with a $\rho^o\rho^o$ pair in the central region (i.e., $pp \rightarrow ppX$, $X \rightarrow \rho^o\rho^o \rightarrow (\pi^+\pi^-)(\pi^+\pi^-)$). This plot contains 830 events (25.4% of the total number of events). A $\pi^+\pi^-$ pair was considered consistent with a ρ^o if $0.620 < M(\pi^+\pi^-) < 0.920$ GeV. In Figure 7.9, the four pion mass distribution is shown for events which were consistent with at least one ρ^o in the central region (i.e., $pp \rightarrow ppX$, $X \rightarrow \rho^o\pi^+\pi^- \rightarrow \pi^+\pi^-\pi^+\pi^-$). This plot contains 2680 events (80.2% of the total number of events). Note that Figure 7.8 is a subset of this plot. No clear enhancement is seen in these plots. Without a careful analysis, these plots by themselves do not allow us to determine how much of the central system consists of $\rho^o\rho^o$ decay, how much consists of $\rho^o\pi^+\pi^-$ decay and how much consists of $\pi^+\pi^+\pi^-\pi^-$ decay, where the pions are described by phase space.

Before any fitting could be done for how much each of these subprocesses are needed to describe the data, it was necessary to calculate the acceptance of the SFM for the six prong AND trigger. The procedure to calculate the SFM acceptance was the same as the six prong OR data, except that the central region was required to have at least one track on each side of the detector as explained in Chapter 2. As in the OR data, it was decided that the additional corrections which used the correlations of the projected angles in the x-z plane for the leading

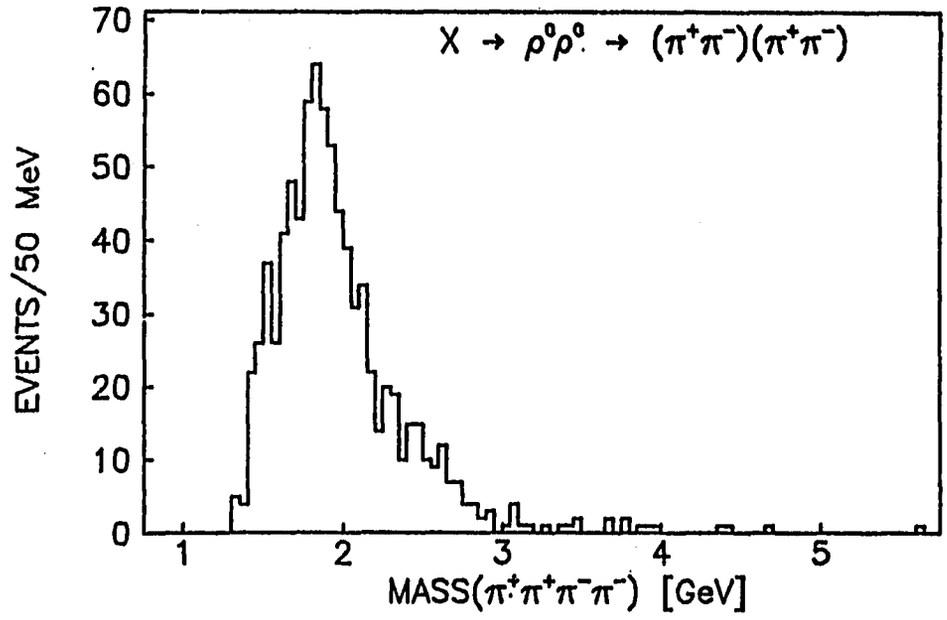

Figure 7.8. Four pion mass for events consistent with central system coming from the decay of two neutral rho mesons

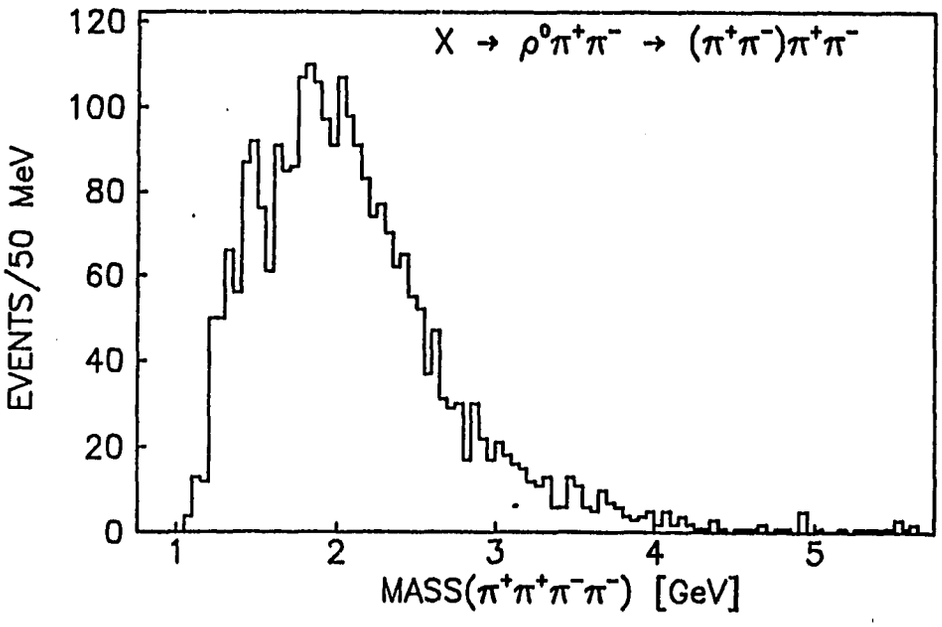

Figure 7.9. Four pion mass for events consistent with central system coming from the decay of one neutral rho meson accompanied by a $\pi^+\pi^-$ pair

protons described in Section 4.2 would not be performed for the six prong AND data. The Monte Carlo events were generated for the central four pion masses of 0.9 to 1.6 GeV in 100 MeV intervals and from 1.8 to 5.0 GeV in 200 MeV intervals.

In order to fit the two dimensional distributions of the two pion mass combinations, the same approach as described in Section 6.2 was used. The Monte Carlo generated events were used to generate three separate two dimensional histograms for the three different hypotheses given above, using the proper weights on the events for each process. Recall that this was done by generating one histogram with just the four pion phase space, a second one with the event weight multiplied by the square of a Breit-Wigner amplitude for a single ρ^o, and a third one with the event weight multiplied by the ρ^o Breit-Wigner intensity applied twice, once for each $\pi^+\pi^-$ pair.

Once these three histograms using the Monte Carlo data were formed, one could then minimize the chi-square distribution given by:

$$\chi^2 = \sum_{i=1}^{N} (n_i - a n_i^{4\pi} - b n_i^{\rho\pi\pi} - c n_i^{\rho\rho})^2 / \sigma_i^2$$

just as in the OR data.

This chi-square was calculated for different fractions a, b, and c in 200 MeV bins for the mass of the four pion central system between 0.9 and 2.5 GeV (i.e., the same mass ranges as shown in Figures 7.4-5). Before fitting, the data were subjected to the same cuts as in the Monte Carlo data used to calculate the acceptance of the SFM. This reduced the number of events to 2,667. The value of the chi-square was plotted and the minimum value was found. The error was calculated for a change in the χ^2

value by one unit. The results are given in Table 7.1.

In this case the values at low mass are worse than the OR data in that the values are too high for the $\rho^0\rho^0$ term. This comes about due to the discrete nature of the Monte Carlo data and the fact that at low mass the four pion mass spectrum is rapidly increasing, just as in the OR data. The data at lower four pion masses cannot support the claim of such a large percentage of $\rho^0\rho^0$ production. As in the OR data case, we have come to the conclusion that a value near zero would be more in line with what the data will support by studying the effects of producing Monte Carlo data in finer mass bins for the mass interval between 1.1 and 1.3 GeV.

Table 7.1. Fractions of $\rho^0\rho^0$, $\rho^0\pi^+\pi^-$, and $\pi^+\pi^-\pi^+\pi^-$ phase space for the process $pp \rightarrow pp\pi^+\pi^-\pi^+\pi^-$

Mass(4π) [GeV]	4π ps (a)	ρππ (b)	ρρ (c)	χ^2/d.f.
0.9<M<1.1	Insufficient data for fit			
1.1<M<1.3	0.21 ±0.18	0.00 ±0.09	0.79 ±0.16	1.7
1.3<M<1.5	0.45 ±0.15	0.03 ±0.13	0.52 ±0.07	1.5
1.5<M<1.7	0.59 ±0.12	0.20 ±0.11	0.21 ±0.05	1.0
1.7<M<1.9	0.70 ±0.10	0.17 ±0.09	0.13 ±0.05	1.7
1.9<M<2.1	0.46 ±0.12	0.51 ±0.11	0.03 ±0.05	0.8
2.1<M<2.3	0.59 ±0.14	0.40 ±0.13	0.01 ±0.05	0.8
2.3<M<2.5	0.52 ±0.21	0.44 ±0.20	0.04 ±0.06	1.3

7.3. Simple Spin-Parity Analysis

The same simple spin-parity analysis used for the six prong OR data was repeated for the six prong AND data. The dependence of the data on ψ was plotted and found to give the same featurless structure, so the figures are not shown. The only conclusion from this analysis was that the distribution of this decay angular distribution can be explained by S-wave decay for the range of four pion masses examined.

7.4. Conclusions

The six prong AND data show some evidence of structure around the central four pion mass value of 1.3 GeV; however, this structure is not as evident as in the OR data. There is a clear signal for the central system containing a single ρ^0 above the central four pion mass value of 1.3 GeV, but little or no convincing evidence of any $\rho^0\rho^0$ production. This behavior is identical to that of the six prong OR data. As in the OR data, the absence of this subprocess marks an important difference between this process and the topologically similar process of the $\gamma\gamma$ interaction in e^+e^- collisions.

A simple spin-parity analysis of the four pion system does no more than in the OR data case to show any features of the central system relating to the angular momentum of any states being produced. The only conclusion possible from this spin-parity study would be that the four pion system seems to be produced with the same angular momentum at all masses.

8. FOUR PRONG "TOF" DATA ANALYSIS

8.1. Final Cuts on Data

Due to the small size of the four prong TOF data sample, it was necessary to combine the data taken with the three different time delays described in Chapter 2. The events recorded without the veto on the intermediate angles are not included in this data sample. Of the 398,460 events in this sample which were successfully processed and written out to a DST, only 27,586 of them had exactly four tracks associated to a common vertex. After the same cuts on x_F of the fast leading protons ($0.55 < x_F < 1.8$) and the requirement of charge balance, 20,013 of these events were left to submit to the kinematical fit described in Chapter 3.

These data are quite different from the four prong OR and AND data because of the greatly enhanced kaon and proton sample. Figure 8.1 shows the measured TOF M^2 distribution (a) without any cuts on the momenta of the tracks, and (b) with the requirement that the momenta of each track be less than 1.0 GeV. From Figure 8.1(a), we estimate that the fraction of pions in the central system is 0.5, the fraction of kaons is 0.3 and the fraction of protons is 0.2. Thus, roughly half the events consist of pions in the central system. Because of this, the data were separated into these three groups to set further cuts and for studying the mass distributions.

Figures 8.2-4 show the probability-of-fit value distributions for each mass hypothesis. On the basis of previous experience, and on studies of the behavior of the invariant mass distributions for each mass

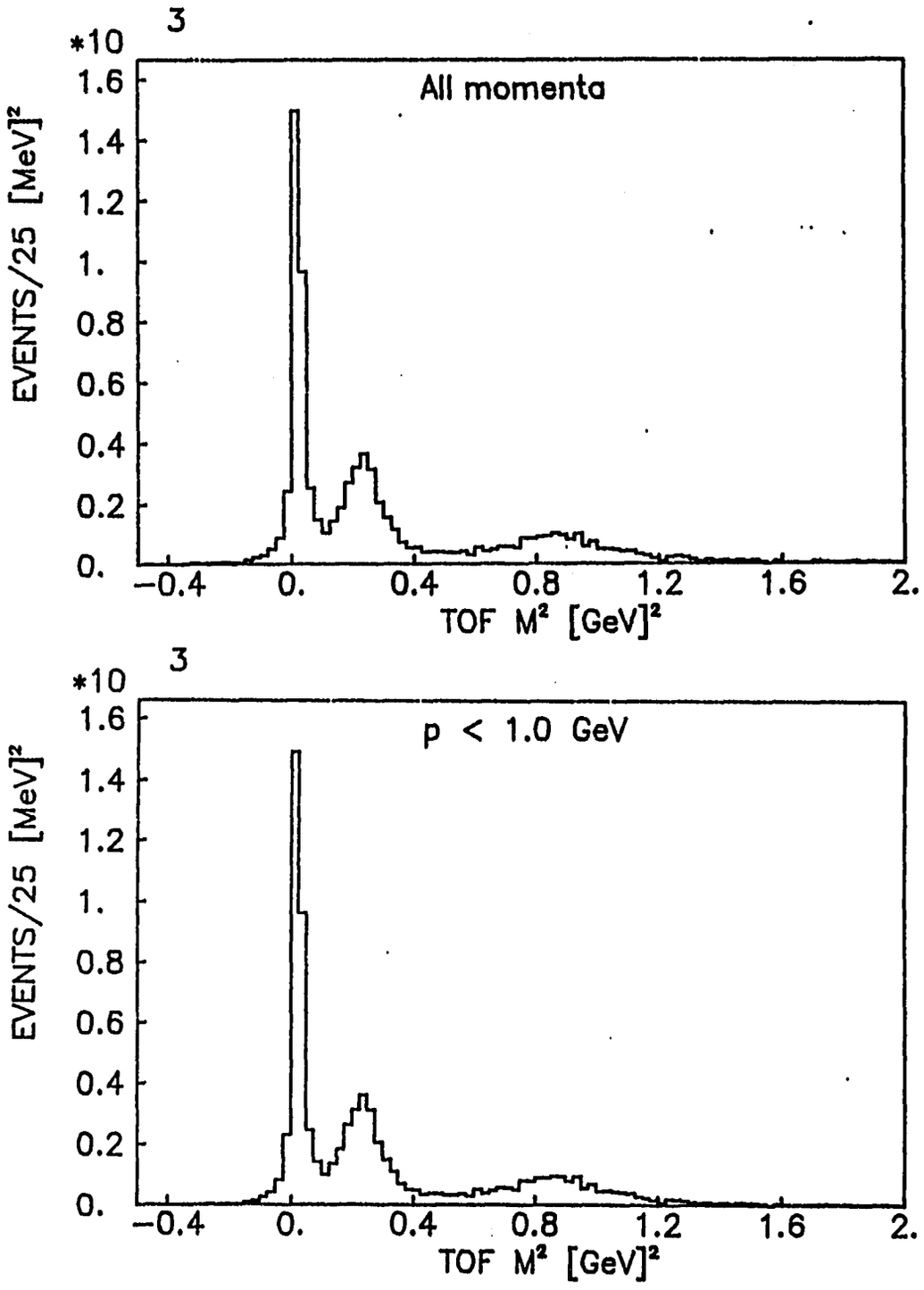

Figure 8.1. Measured TOF M^2 distribution for (a) central tracks with no momenta cut and (b) for central tracks with p<1.0 GeV

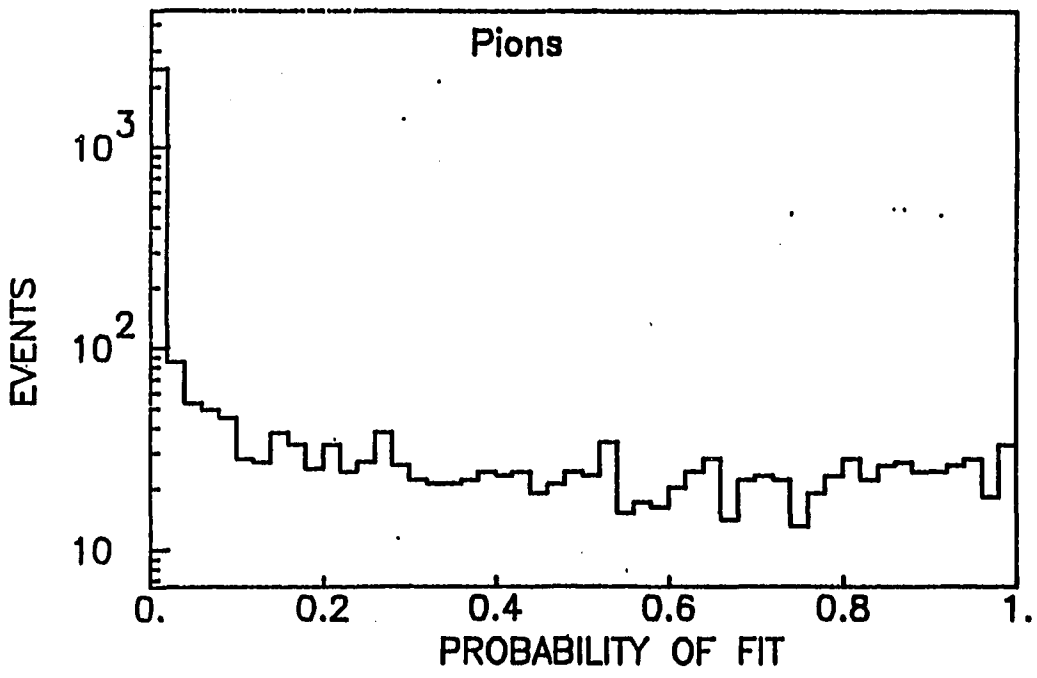

Figure 8.2. Probability-of-fit for events with central system assumed to consist of pions

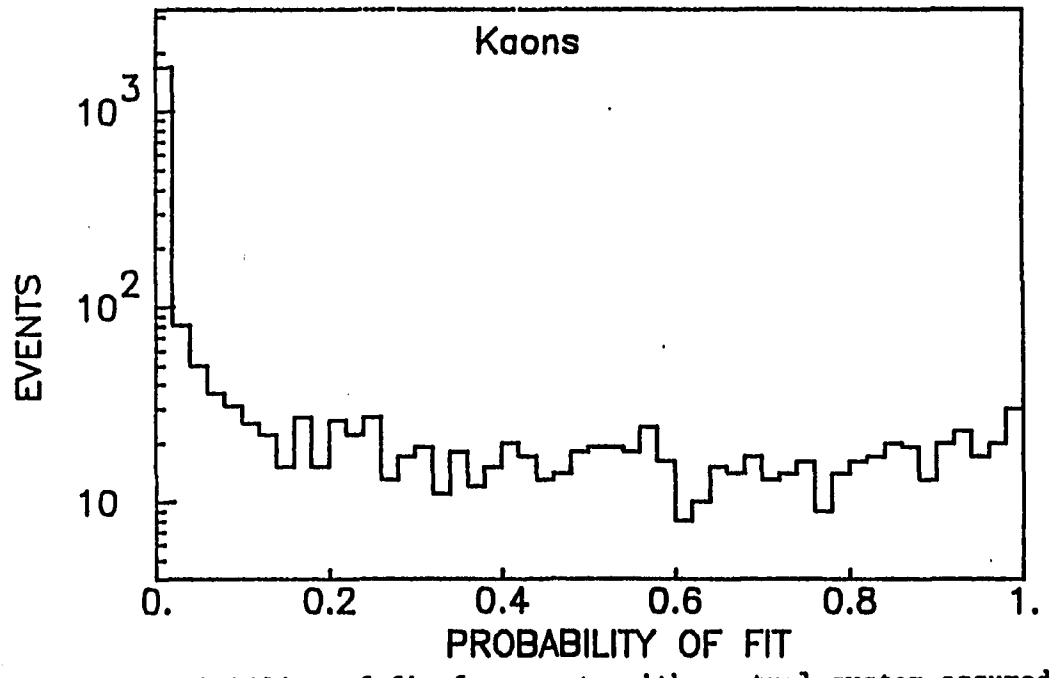

Figure 8.3. Probability-of-fit for events with central system assumed to consist of kaons

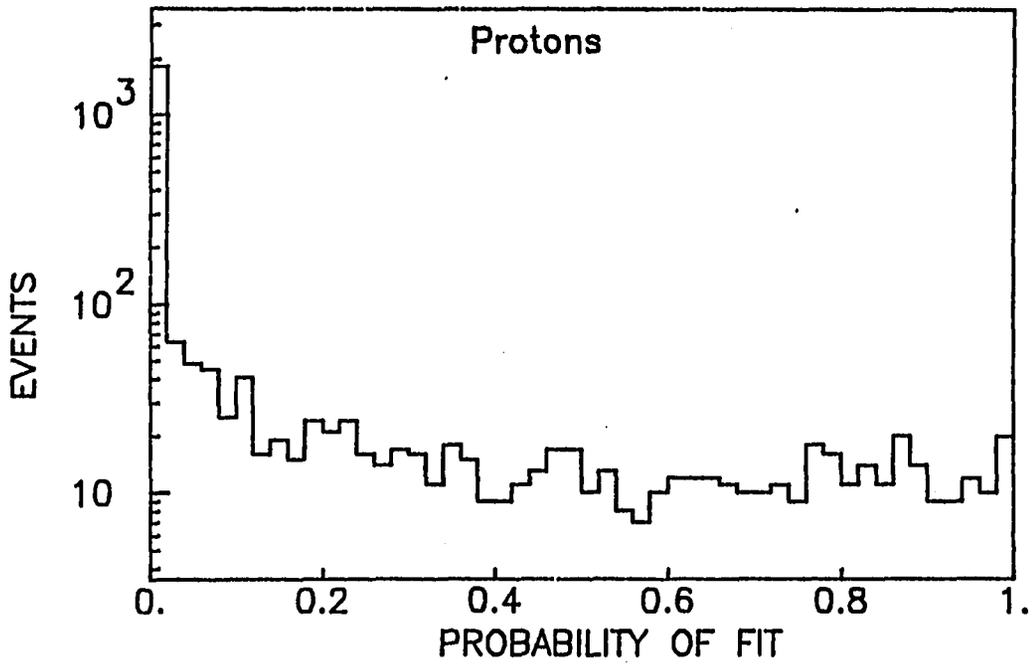

Figure 8.4. Probability-of-fit for events with central system assumed to consist of protons

hypothesis, the cut on the probability-of-fit value was set at 0.05. A higher cut could be justified, but due to the small size of each data sample it was decided that the loss in statistics would outweigh the reduction of background gained by using a higher cut. In addition, each data sample was submitted to the same cut on the x_F value for the outgoing leading protons as in Chapters 4-7, i.e., $x_F > 0.8$.

Roughly one-third of the events have no valid TOF M^2 value for either of the two central particles. Initially, it was decided to use the probability-of-fit value to decide which mass hypothesis should be used for these events, i.e., which mass hypothesis gave the best fit. After the cuts on the probability-of-fit and x_F values, there remained 1197 events with the central system assumed to be pions, 875 events with the

central system assumed to be kaons, and 722 events with the central system assumed to be a proton-antiproton pair. Further cuts on these event samples will be discussed below.

8.2. Study of Mass Distributions

Figures 8.5-7 show the invariant mass distributions for the central pairs for each mass hypothesis, selected as indicated in Section 8.1. After studying these events, it was discovered that we must require that one of the two central tracks be identified by the TOF system. This was because the events without the TOF information actually were events that did not satisfy the trigger setup.

As explained in Chapter 2, the TOF trigger involved a DC road system for positively charged central tracks to ensure that the tracks which satisfied the central track requirement and the tracks which satisfied the TOF delay were the same tracks. At the DST level, the information in what is termed a "pattern unit" can be checked to determine which central track triggered the TOF part of the trigger for the event. When this was done, it was discovered that the events where the TOF M^2 could not be found did not have the pattern unit set for either of the central tracks. This is not surprising since the DC road system was much cruder than the track reconstruction process, so the reconstructed tracks will not always extrapolate to the same TOF counter as used in the DC roads. On the basis of this information, it was decided to discard these events. Also, when the central system consists of pions the events are not interesting since the purpose of the TOF trigger was to isolate kaons and protons in the

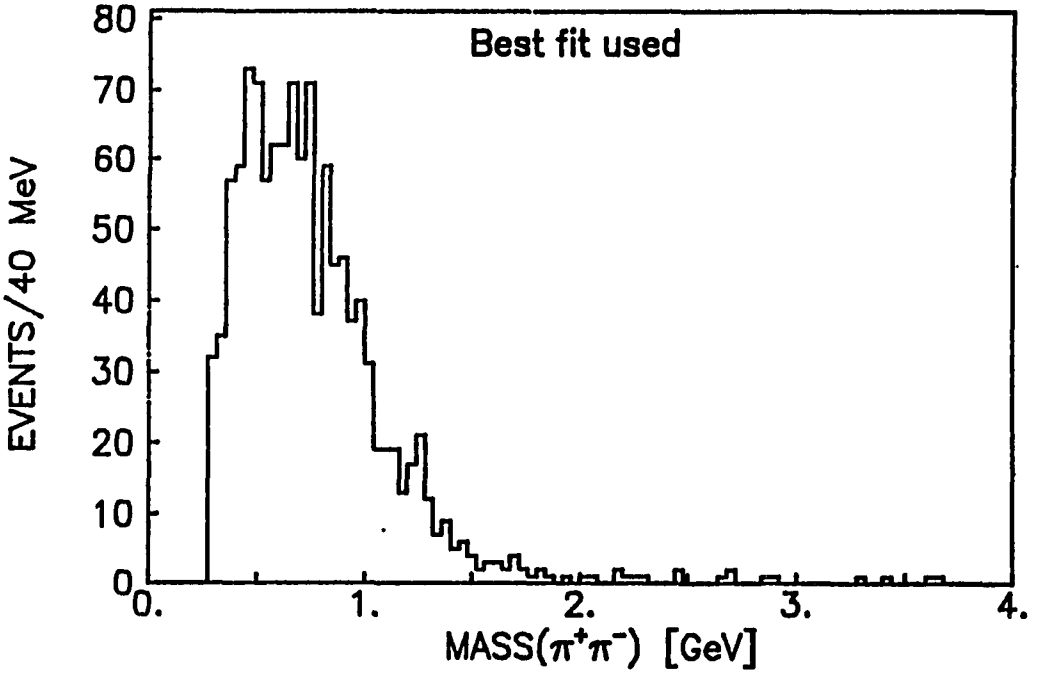

Figure 8.5. Invariant mass distribution for events with central system consisting of pions determined by TOF and the 4C-fit

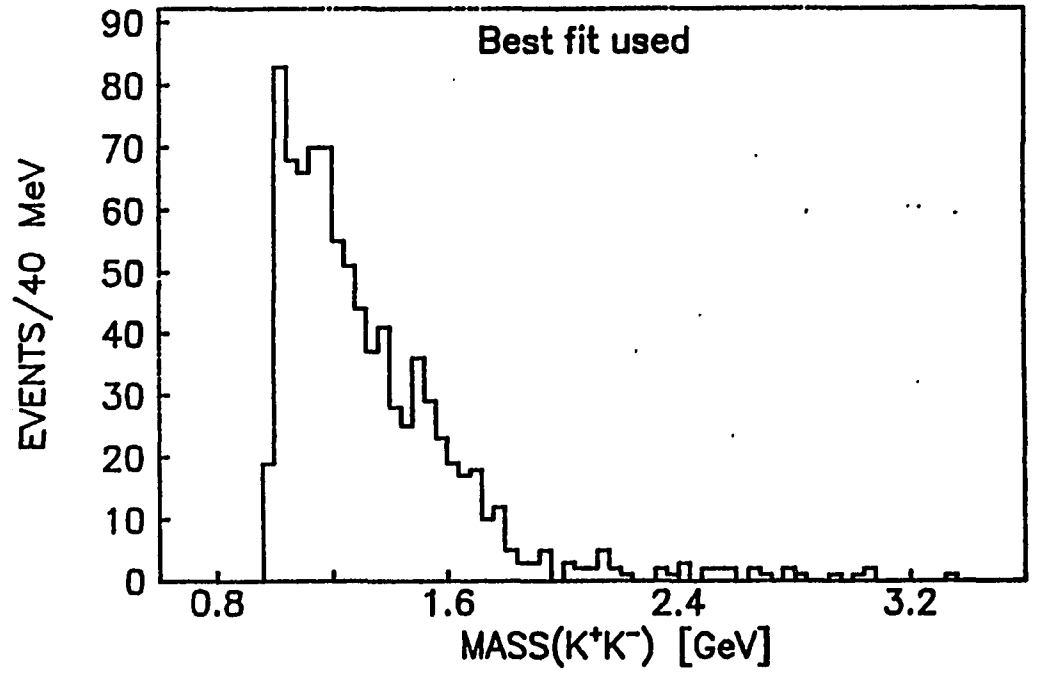

Figure 8.6. Invariant mass distribution for events with central system consisting of kaons determined by TOF and the 4C-fit

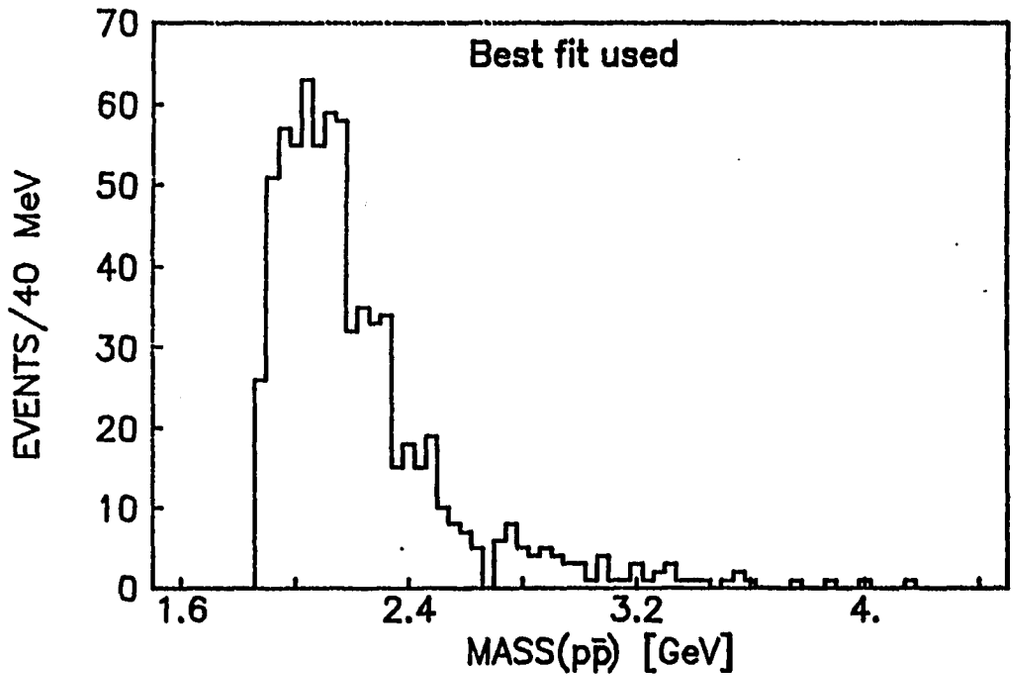

Figure 8.7. Invariant mass distribution for events with central system consisting of protons determined by TOF and the 4C-fit

central system. Thus, these events are ignored for the rest of this analysis.

While studying events with and without the pattern unit set, it was found that requiring a kaon or proton identification was nearly equivalent to requiring the pattern unit to be set. Thus, there was no need to make use of the pattern unit information once the requirement of the identification of a kaon or proton by the TOF system was made. After this cut there remained 699 K^+K^- events and 396 $p\bar{p}$ events. The mass distributions for these events are shown in Figures 8.8 and 8.9.

The K^+K^- distribution changes only slightly after this cut. Notice that the small peak at 1160 MeV and the spike near threshold become more pronounced, but are still not significant enough to claim the existence of

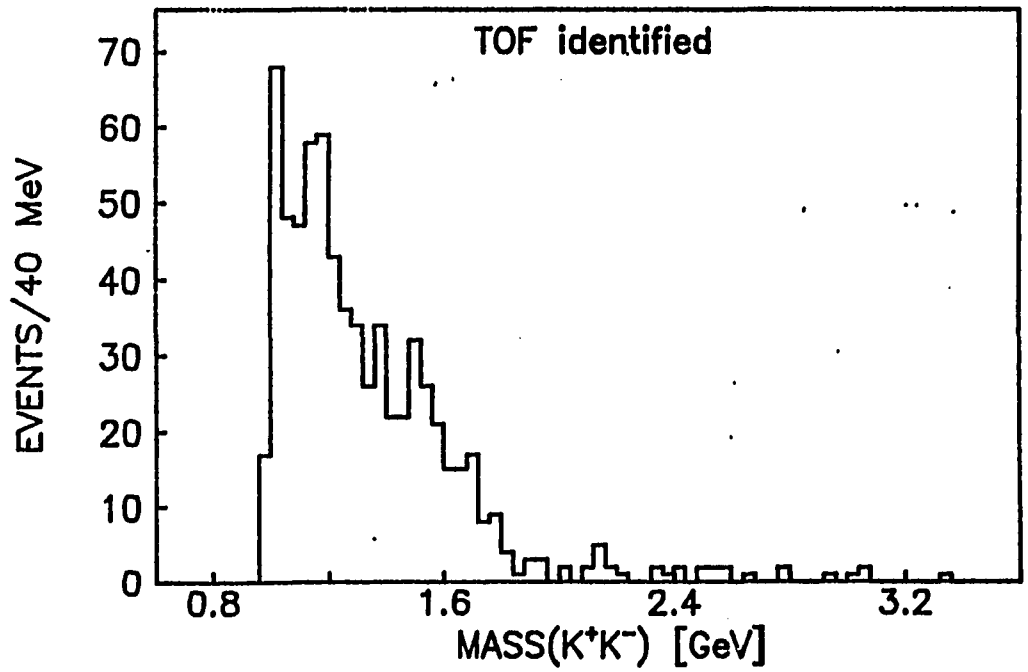

Figure 8.8. Invariant mass distribution for events with central system consisting of kaons determined by TOF

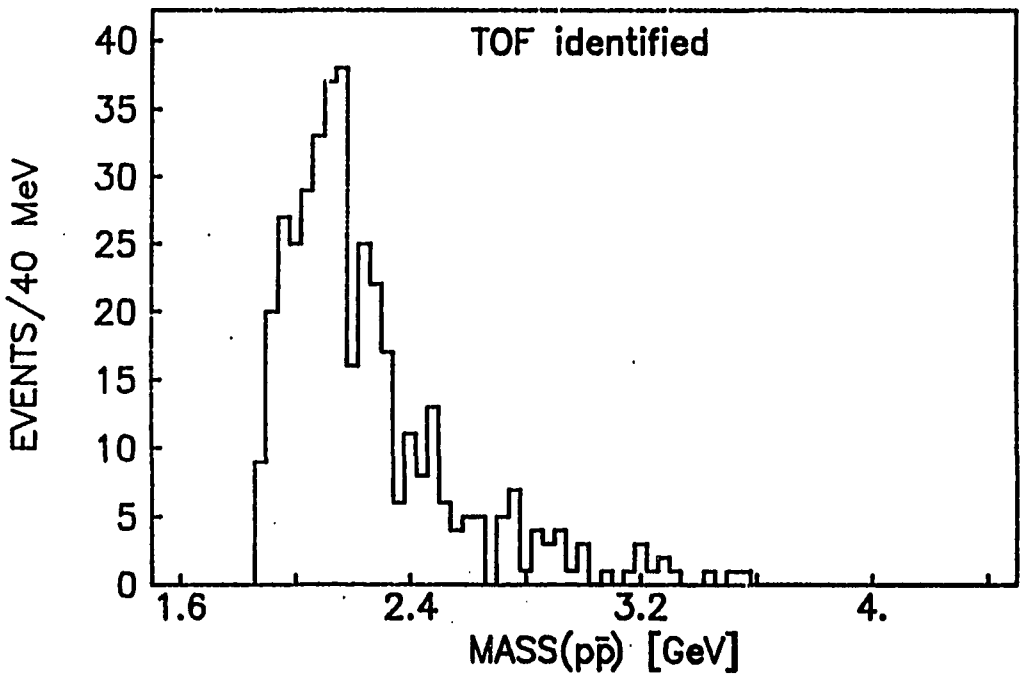

Figure 8.9. Invariant mass distribution for events with central system consisting of protons determined by TOF

resonances due to the low statistics involved.

The $p\bar{p}$ distribution appears quite different below 2100 MeV. There now appears the potential of a signal in the region of 2100 MeV. There are two known resonances in this region that couple to $p\bar{p}$. One is the $h^o(2030)$ with $J^{PC}=4^{++}$, the other is the $\varepsilon(2150)$ with $J^{PC}=2^{++}$. The h^o has been seen to decay directly into a $p\bar{p}$ pair in the reaction $\pi^+n \rightarrow \bar{p}pp$ at 10 GeV/c [Lamsa et al. 1982]. However, the h^o mass is really too low to be identified with the peak in Figure 8.9. The ε has been seen in the partial wave amplitudes for $p\bar{p}$ annihilation but is not a well established resonance [Wohl et al. 1984].

An attempt was made to examine the moments for the $p\bar{p}$ system; however, due to the very limited statistics, this analysis was of little value since the statistical fluctuations are much larger than any structure seen in the plots. This remains true even when the data are put in 100 MeV bins. Thus, any further investigations into deciding whether this enhancement is real or is some sort of threshold effect, possibly due to the acceptance of the SFM detector, run directly into the problem of very low statistics. The investigation of this mass distribution and in particular the nature of this enhancement is not pursued further in this thesis.

9. SIX PRONG "TOF" DATA ANALYSIS

9.1. Final Cuts on Data

Due to the small size of the six prong TOF data sample, it was necessary to combine the data taken with the three different time delays described in Chapter 2. The events recorded without the veto on the intermediate angles are not included in this data sample. Of the 398,460 events in this sample that were successfully processed and written out to a DST, only 35,004 of them had exactly six tracks associated to a common vertex. After the same cuts on x_F of the fast leading protons ($0.55 < x_F < 1.8$) and the requirement of charge balance, 21,828 of these events were left to be submitted to the kinematical fit described in Chapter 3.

These data are quite different from the six prong OR and AND data because of the greatly enhanced kaon and proton sample. The measured TOF M^2 distribution is very similar to Figure 8.1, so it is not shown here. The same problem as discussed in Chapter 8 exists for these data in respect to the TOF information on the central tracks. Specifically, the pattern unit for the TOF trigger was not always set for one of the reconstructed central tracks. This basically meant that the trigger was not really satisfied, but was "faked" by spurious hits in the 700 TOF stand. Thus, in each case discussed below, the pattern unit was required to be set for one of the central tracks in order to delete these data from each sample.

Each subprocess discussed in Section 9.2 has identical cuts on the probability-of-fit value for the 4C-fit and on the x_F values of the

outgoing fast protons. On the basis of the probability-of-fit distributions, it was required that the probability-of-fit be greater than 0.10. The same cut on x_F as was used in all other data samples was used here, i.e., $x_F > 0.8$. The number of events left after these cuts will be given below as each mass combination is discussed.

The x_F distributions of the outgoing leading protons show the same double-pole structure as seen in all other data discussed in this paper and are not shown here. Also, the momentum transfers of the two beam protons show no obvious correlation with each other. The similarity of these plots with the same plots for the four prong OR data in Chapter 4 indicates that we have succeeded in selecting a set of events consistent with DPE being the primary production process for the events.

9.2. Study of Mass Distributions

For comparison with the OR and AND data the case where all central tracks are consistent with being pions was studied. After the cuts discussed in Section 9.1, 674 events remained in this data sample. This case is the least interesting one for the TOF data since the whole idea of this trigger was to enhance the production of kaons and protons in the central system. The mass distribution for the four pion central system is shown in Figure 9.1. This mass distribution is shifted to slightly lower mass than the OR and AND data. This is due to the fact that the TOF trigger would only accept slow pions. The mass distribution for the $\pi^+\pi^-$ pairs is shown in Figure 9.2. There is little or no evidence for the ρ^0 as seen in the OR and AND data, but in the region of 500 MeV one does see

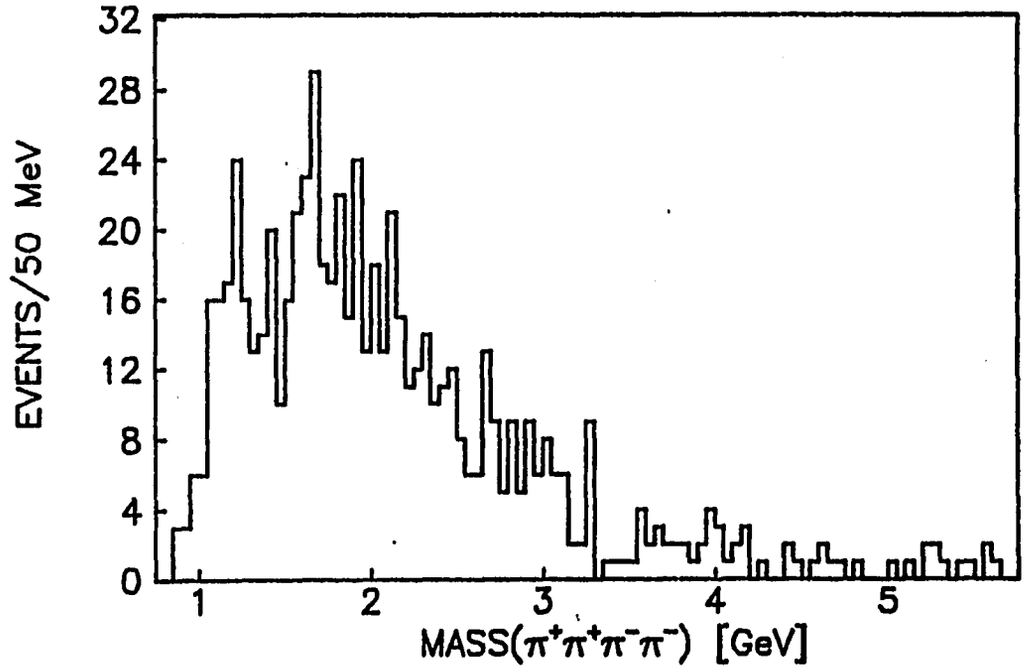

Figure 9.1. Mass distribution for the $\pi^+\pi^+\pi^-\pi^-$ central system

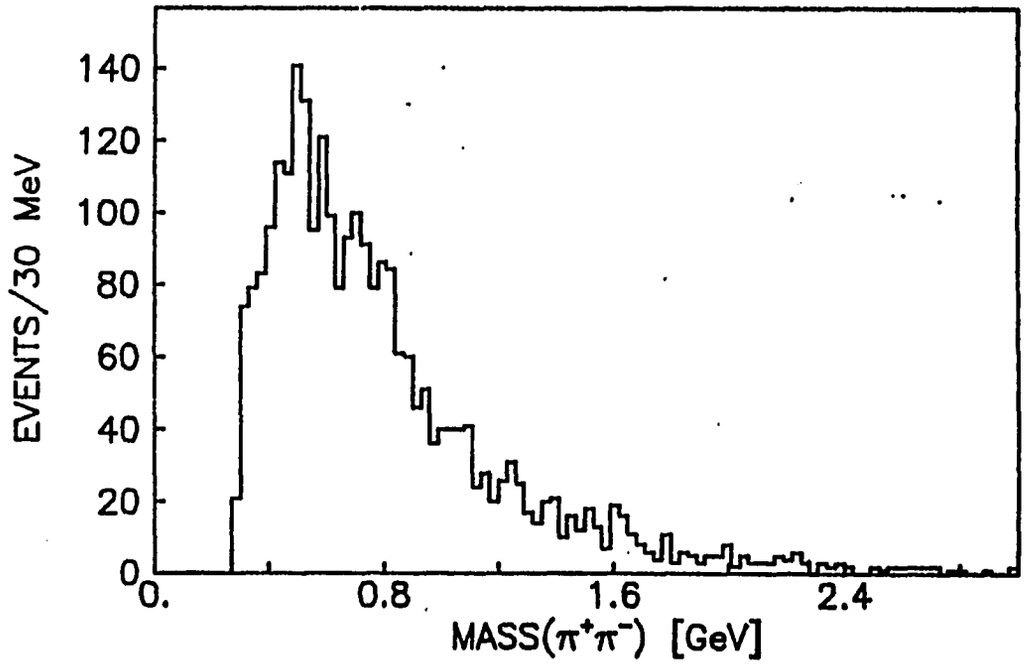

Figure 9.2. Mass distribution for $\pi^+\pi^-$ pairs in the $\pi^+\pi^+\pi^-\pi^-$ system

evidence for the decay of a K^0_S. This aspect of the six prong data will be addressed in Chapter 10.

The case where the central system consists of $\pi^+\pi^-K^+K^-$ consisted of 472 events after the cuts discussed in Section 9.1. Included in these cuts was the requirement that the pattern unit be set by one of the kaons. The mass of the four particle central system is shown in Figure 9.3. Since there is usually only one central particle which has TOF information, each event will usually enter into the plot twice. The probability-of-fit value for these two hypotheses was not found to be very helpful in removing this ambiguity, so no attempt was made to use the fit results to select one mass hypothesis rather the other. Thus, this plot contains 825 entries. Note that there are four possible ways to label the four central particles in order to get $\pi^+\pi^-K^+K^-$, but when one of them is identified by the TOF there can only be two combinations allowed. The mass of the $\pi^+\pi^-$ pair in these events is shown in Figure 9.4, and the mass of the K^+K^- pair is shown in Figure 9.5. The mass of the π^+K^- and π^-K^+ pairs are shown in Figure 9.6. The only indisputable enhancement in these plots appears in Figure 9.6, which is a clear signal for the $K^*(890)$ meson. The $\pi^+\pi^-$ distribution does show a possible signal for the $\rho^0(770)$ meson, but the enhancement is also consistent with a statistical fluctuation. To break these events down in further categories (e.g., to look at events with the K^* present) is of little use due to the very low statistics.

The case where the central system consists of $\pi^+\pi^-p\bar{p}$ consisted of 428 events after the cuts discussed in Section 9.1. Included in this cut was the requirement of the pattern unit to be set by either the proton or

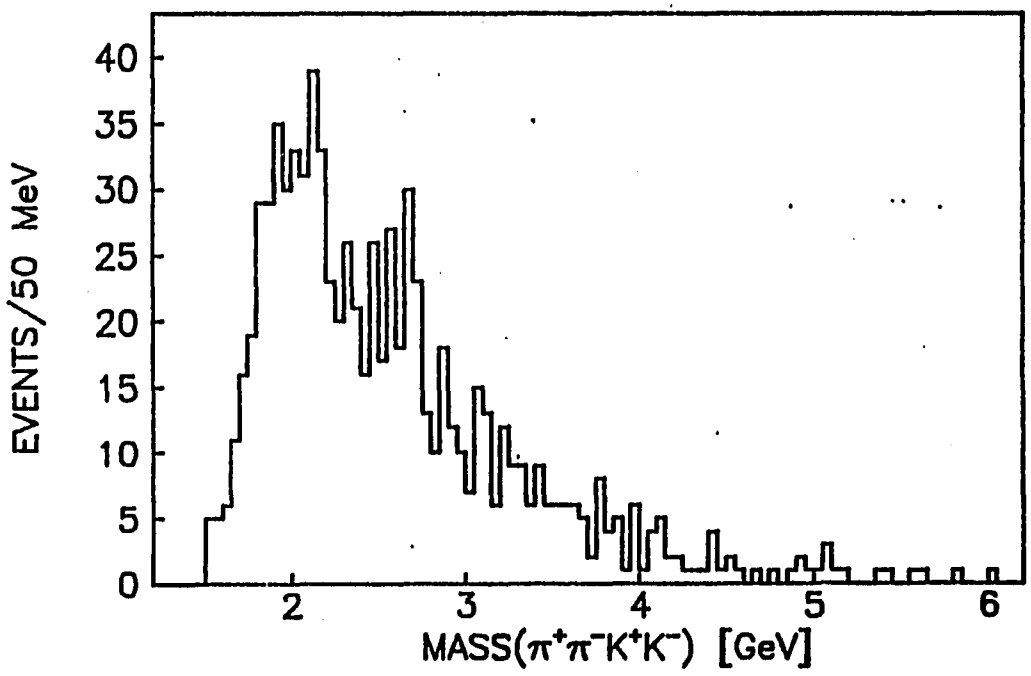

Figure 9.3. Mass distribution for the $\pi^+\pi^+K^-K^-$ central system

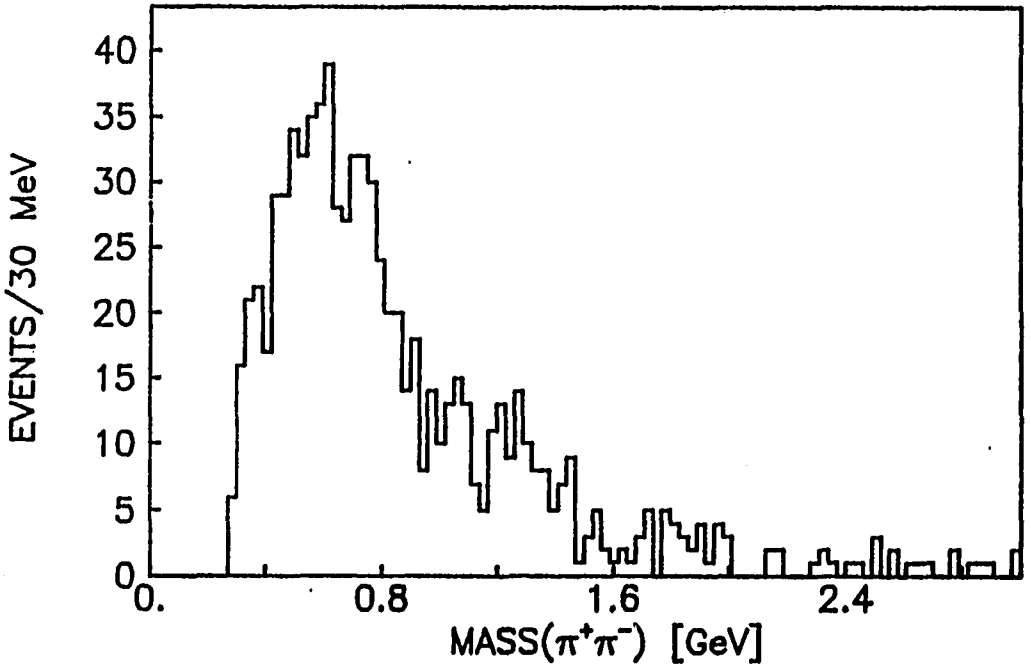

Figure 9.4. Mass distribution for $\pi^+\pi^-$ pairs in the $\pi^+\pi^+K^-K^-$ system

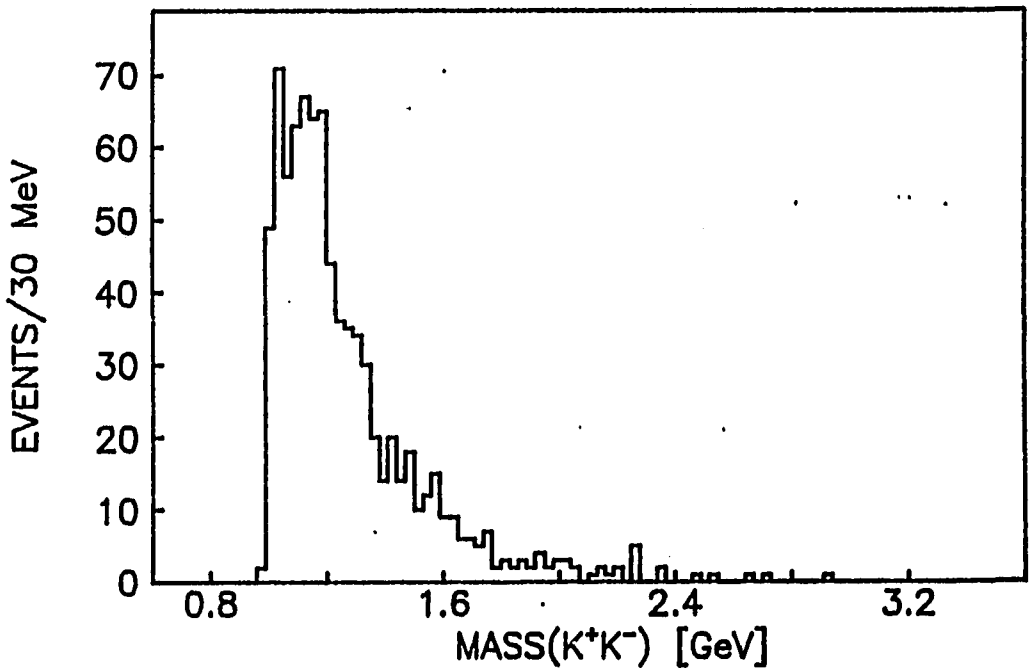

Figure 9.5. Mass distribution for K^+K^- pairs in the $\pi^+\pi^+K^-K^-$ system

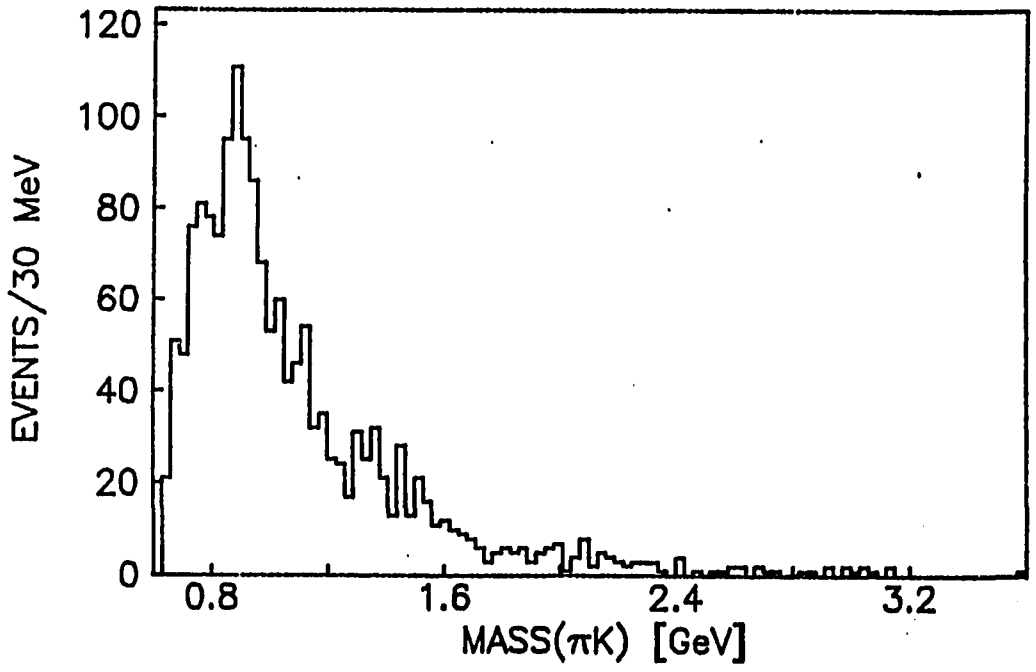

Figure 9.6. Mass distribution for π^+K^- and π^-K^+ pairs in the $\pi^+\pi^+K^-K^-$ system

the antiproton. The mass of this system is shown in Figure 9.7 which contains 718 entries. The mass of the $\pi^+\pi^-$ pairs is shown in Figure 9.8, and the mass of the $p\bar{p}$ pairs is shown in Figure 9.9. The mass of the $\pi^+\bar{p}$ and π^-p pairs is shown in Figure 9.10, which could form the $\Delta^0(1232)$ resonance. The mass of the π^+p and $\pi^-\bar{p}$ pairs is shown in Figure 9.11, which could form the $\Delta^{++}(1232)$ or $\bar{\Delta}^{++}(1232)$ resonances. Neither of the plots for πp and $\pi\bar{p}$ combinations show convincing evidence for the production of the Δ resonances. The small spike in Figure 9.11 is at the right mass, but is only 60 MeV wide, whereas the Δ has a width of 115 MeV. The absence of this resonance is not surprising in DPE since the total J^{PC} of the system must be equal to $0^{++},2^{++},\ldots,$etc. Thus, one must produce two spin 3/2 objects rather than just one, as in the usual case of pion-nucleon scattering.

The cases where the central system consists of only kaons and protons were studied but no plots are shown here. There is a clear problem with pion contamination with the data due to the limited solid angle over which the SFM has the ability to identify particles. Thus, the cases discussed above are the dominant reactions for our TOF trigger, and little can be done to study other exclusive reactions in the six prong TOF data sample.

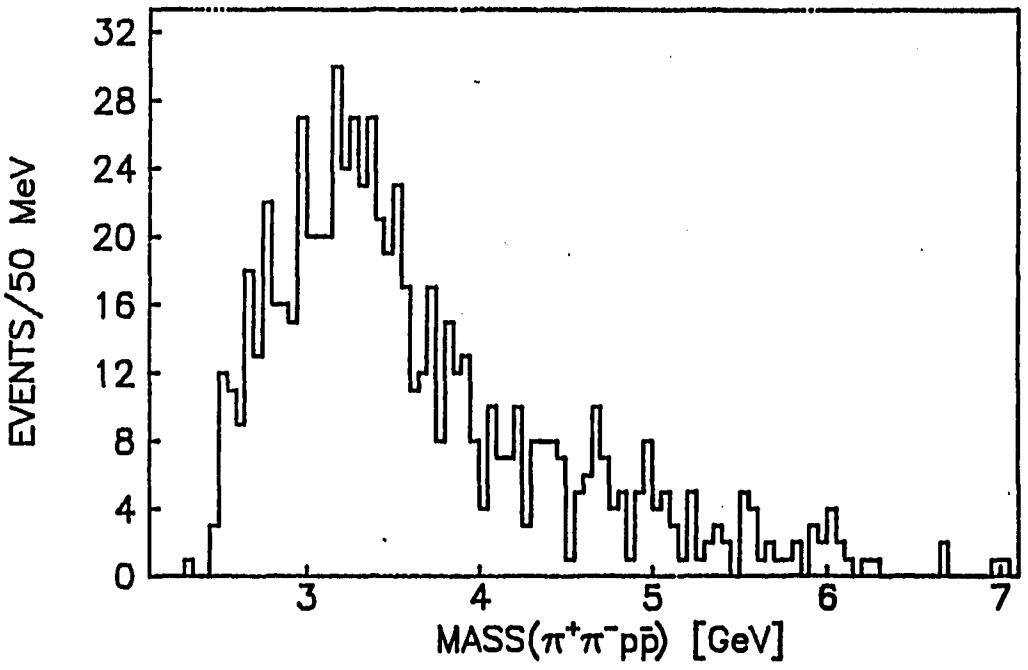

Figure 9.7. Mass distribution for the $\pi^+\pi^+p\bar{p}$ central system

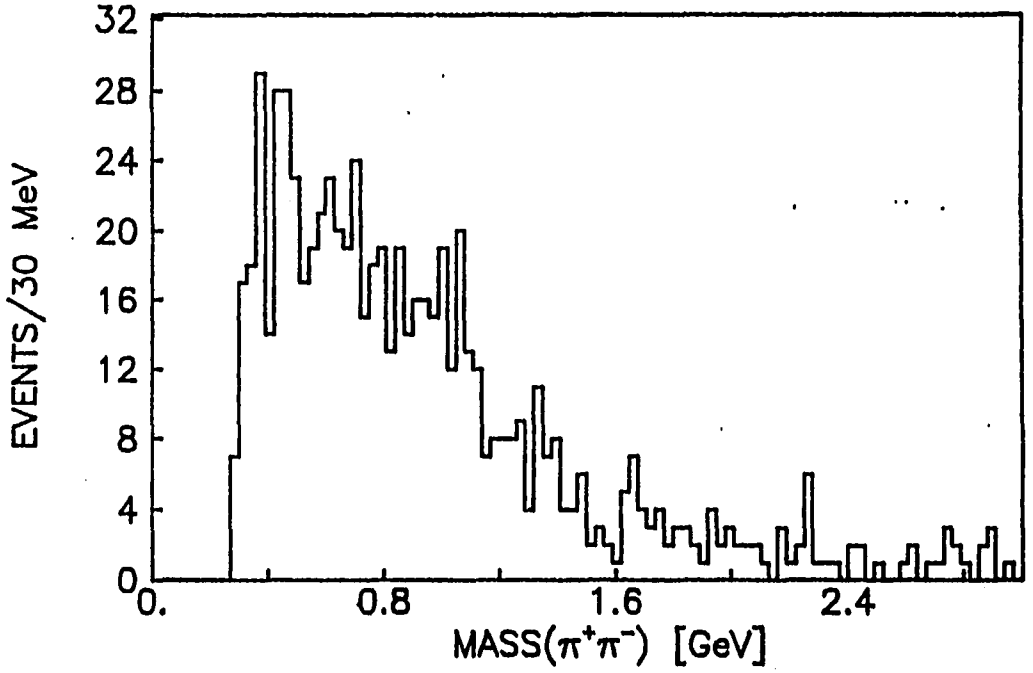

Figure 9.8. Mass distribution for $\pi^+\pi^-$ pairs in the $\pi^+\pi^+p\bar{p}$ system

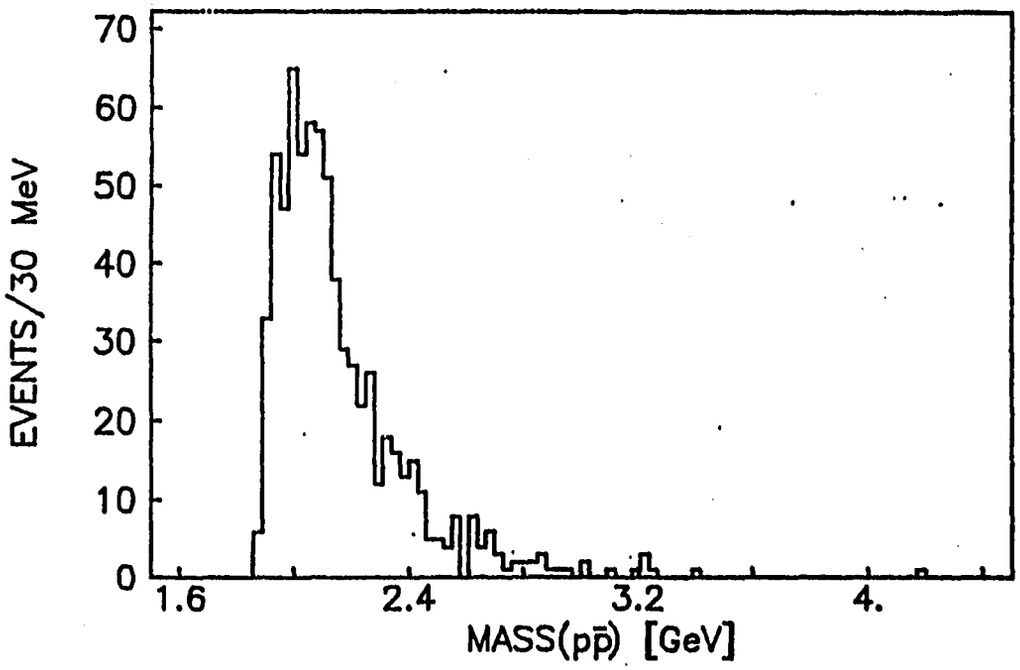

Figure 9.9. Mass distribution for $p\bar{p}$ pairs in the $\pi^+\pi^+p\bar{p}$ system

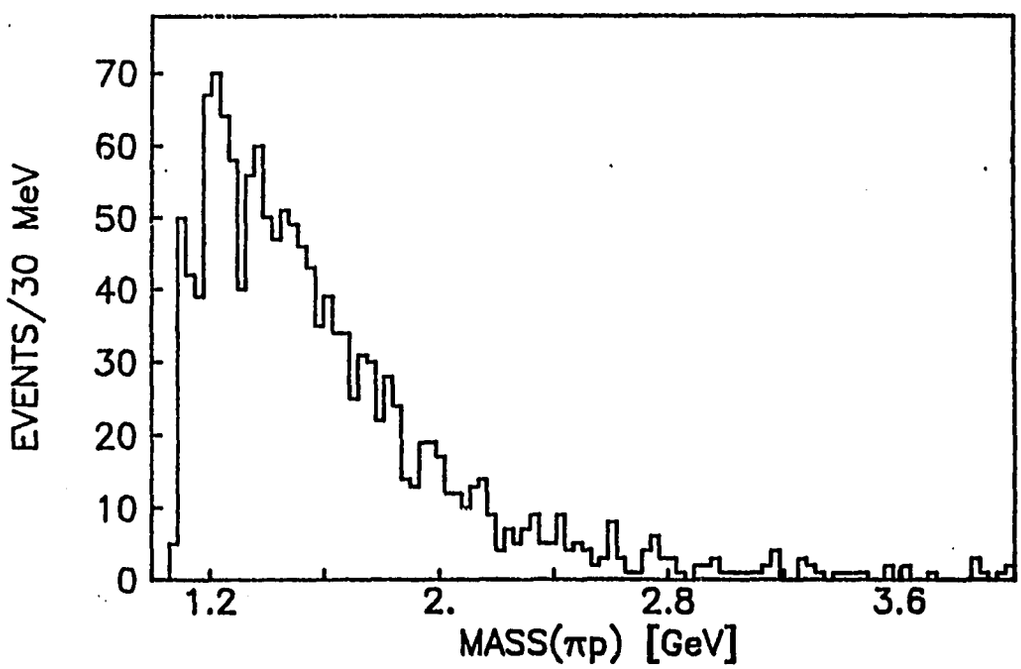

Figure 9.10. Mass distribution for $\pi^+\bar{p}$ and π^-p pairs in the $\pi^+\pi^+p\bar{p}$ system

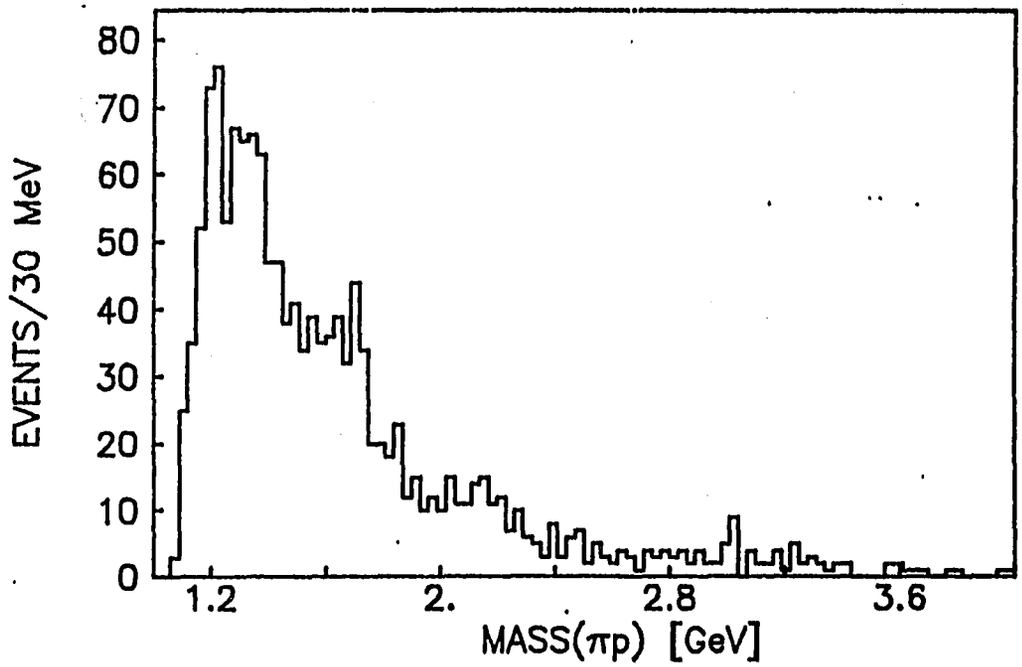

Figure 9.11. Mass distribution for $\pi^-\bar{p}$ and π^+p pairs in the $\pi^+\pi^+p\bar{p}$ system

10. STRANGENESS VIOLATING DECAYS

Another final state of interest in the DPE reaction occurs when the central system is the result of a single strangeness violating decay. One example of this is the process $pp \rightarrow ppK^0K^+\pi^-$ (or $ppK^0K^-\pi^+$), $K^0 \rightarrow \pi^+\pi^-$. Thus, one looks for events with a neutral decay of a K^0_S, since only neutral particles that decay quickly into charged particles can be measured in the SFM detector. One of the shortcomings of the SFM detector is that it does not have very good capability for detecting secondary decays. In order to find a K^0_S, one looks for an outgoing $\pi^+\pi^-$ pair which comes from a secondary vertex. The problem is simply that the SFM does not have a vertex detector. All vertices are found by extrapolating the charged tracks through the magnetic field to their point of closest approach to each other so that a common point may be fitted as the vertex. Thus, when the secondary vertex for the decay of a neutral particle is close (i.e., less than ~ 1 cm) to the primary vertex it is impossible to isolate it. Also, there are large losses from decay tracks which do not extrapolate back into the vertex diamond.

The SFM reconstruction code attempts to find neutral particles that decay into two charged particles at a secondary vertex far enough away from the primary vertex that the two can be distinguished. The methods used in this computer code are described in a paper by K. Rauschnabel and are only outlined here [Rauschnabel 1981]. The basic approach was to select $\pi^+\pi^-$ pairs that had an invariant mass near the mass of the K^0 ($\pm$100 MeV for tracks associated to the vertex and $\pm$150 MeV for tracks not associated to the vertex) and then extrapolate these tracks back through

the magnetic field of the SFM to see if a secondary vertex could be found. This secondary vertex is required to be at least 1 cm away from the primary vertex, and the sum of the momenta of the $\pi^+\pi^-$ pair is required to point back to the primary vertex. Once these requirements are satisfied, the track parameters for the K^0 are calculated just as for all of the charged tracks at the primary vertex. Thus, the results of this process are a list of K^0 particles found, the position of the secondary vertex, the decay length of the K^0, the errors on the track parameters, and the chi-square value of the fit to the K^0 hypothesis.

This code is known to find too many neutrals when applied to Minimum Bias data. The main cause of this is believed to be that events with large charge multiplicity allow random $\pi^+\pi^-$ pairs to fake K^0 decays, i.e., combinatorial backgrounds are large. For the purposes of this analysis, it was assumed that by limiting oneself to six-prong DPE events in which only four charged particles were in the central region, that this problem would be minimized and that the V^0 reconstruction results could be trusted. The resulting analysis will allow one to make a decision whether or not this exclusive channel has enough potential to warrant a more careful analysis of the V^0 reconstruction code behavior when applied to the DPE data. The importance of this is that our collaborators have refined the V^0 reconstruction code for Minimum Bias data, but a careful study must be done before this new code could be applied to our DPE data.

By studying the mass distributions of the $\pi^+\pi^-$ pairs in the six prong data, one can get a rough estimate of the number of true K^0s present. This was done for each data sample and was found to agree with the V^0 reconstruction results. This crude study allowed some confidence that the

assumption of the V^0 reconstruction being valid was reasonable.

The analysis performed here is to assume initially that the V^0 reconstruction results are valid and correct. Next one performs the 4C-fit described in Chapter 3 on the events to eliminate events that do not satisfy energy and momentum conservation. Thus, six-prong events with a K^0 are separated off from the DST and fit as five-prong events with the K^0 replacing the $\pi^+\pi^-$ pair which was found to come from a secondary vertex. The track parameters used are the ones calculated by the V^0 reconstruction program with the mass set to that of the K^0. An immediate problem is that the full error matrix for the K^0 is not available on the DST, so the error matrix used in the fit was just a sum of the errors for the two pions. This is strictly an overestimate of the real errors, but the widths of the pull values for the K^0 particles were consistent with the width of the pull values from the other tracks, so this approximation is sufficient.

This 4C-fit was performed on all three data samples (OR, AND, and TOF) which are discussed together in this chapter. The probability-of-fit distribution for each of these fits is shown in Figure 10.1. One can see that they look very similar to the probability-of-fit value distributions for the other six prong data. The probability-of-fit value was required to be greater than 0.10 in order to eliminate events which did not meet the criteria of energy and momentum conservation. Also, the measured TOF M^2 values were required to be consistent with the above event topology, and a cut of $x_F > 0.8$ was placed on the data. After these cuts there were 438 OR data events, 292 AND data events, and 158 TOF data events with the final state $K^0K\pi$ in the central system.

The plots of the $K^0\pi^\pm$, $K^0K^\pm$, and $K^\pm\pi^\mp$ mass distributions are shown in Figures 10.2-4 for each data sample. The plots of the $K^0\pi^\pm$ masses show

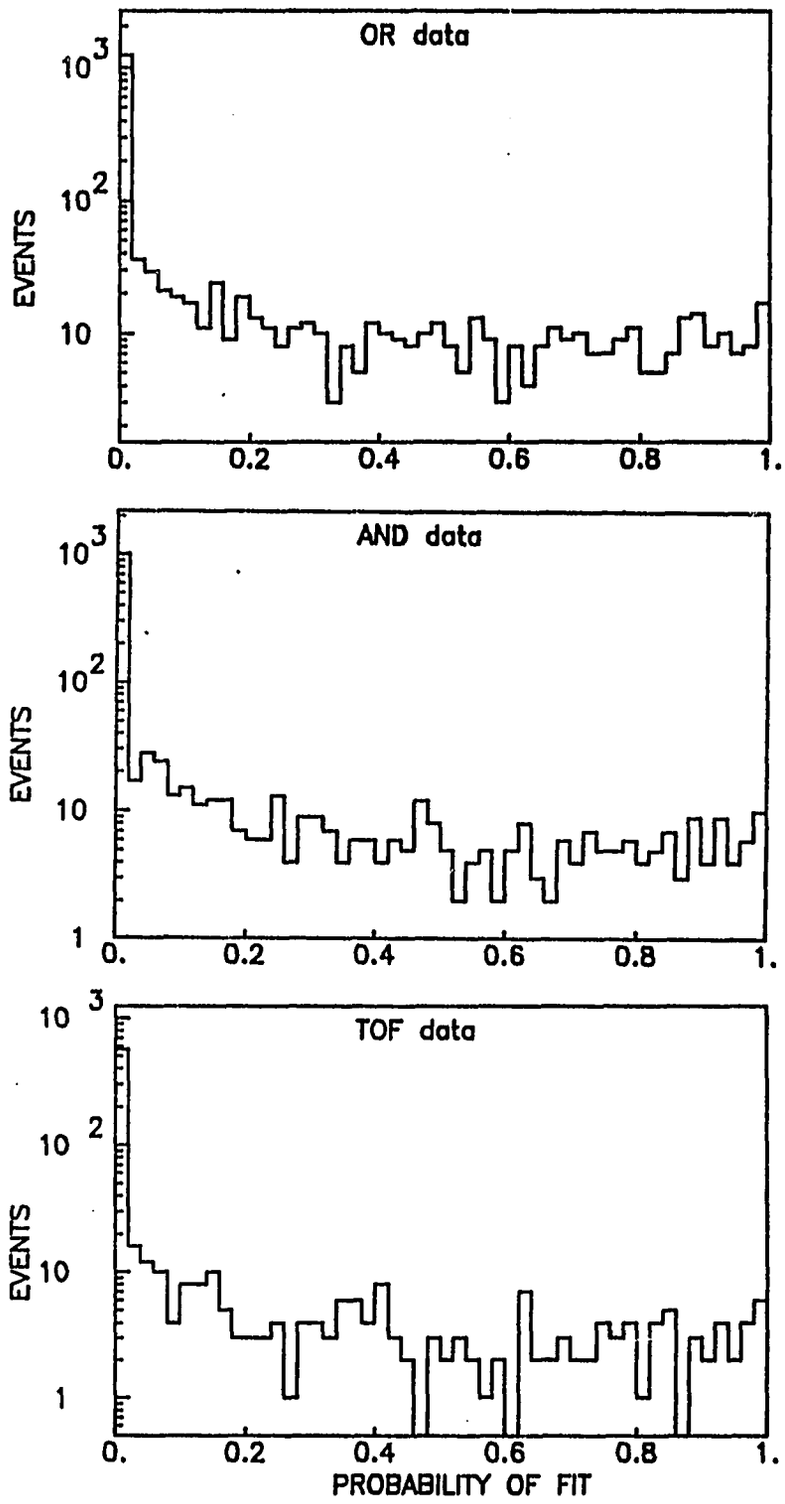

Figure 10.1. Probability-of-fit values for 4C-fit for OR, AND, and TOF data

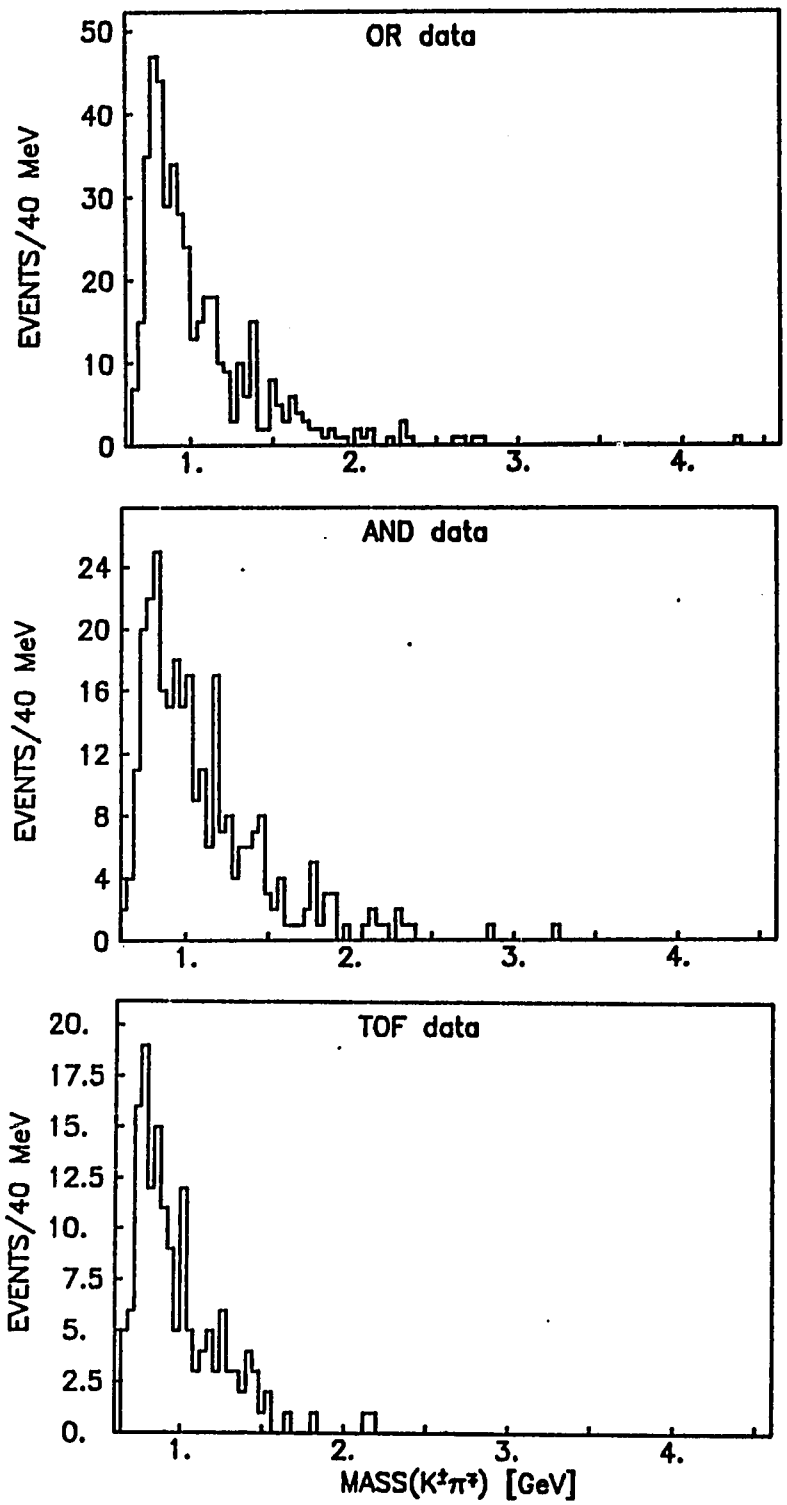

Figure 10.2. Mass distributions for $K^{\pm}\pi^{\mp}$ pairs for OR, AND, and TOF data

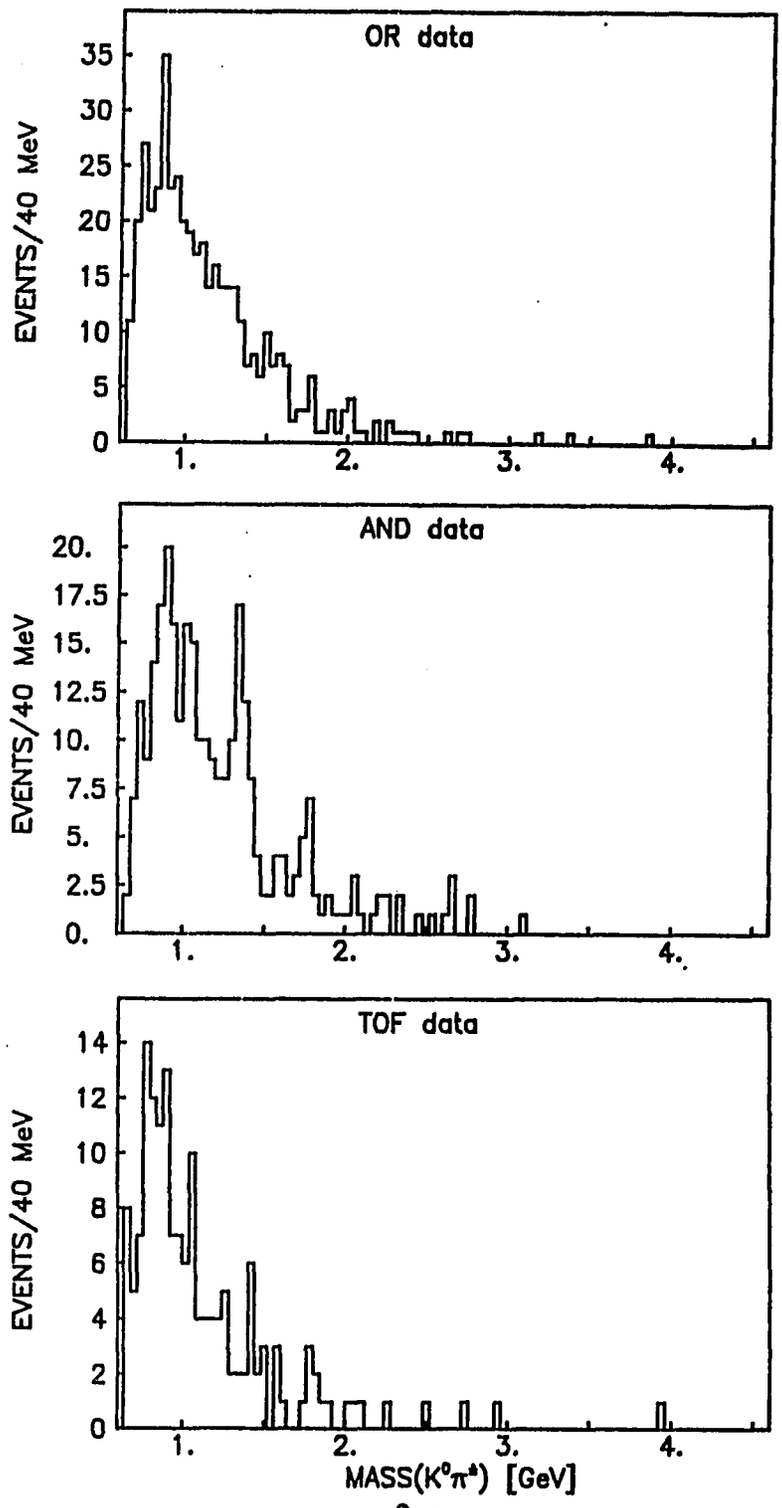

Figure 10.3. Mass distributions for $K^0\pi^{\pm}$ pairs for OR, AND, and TOF data

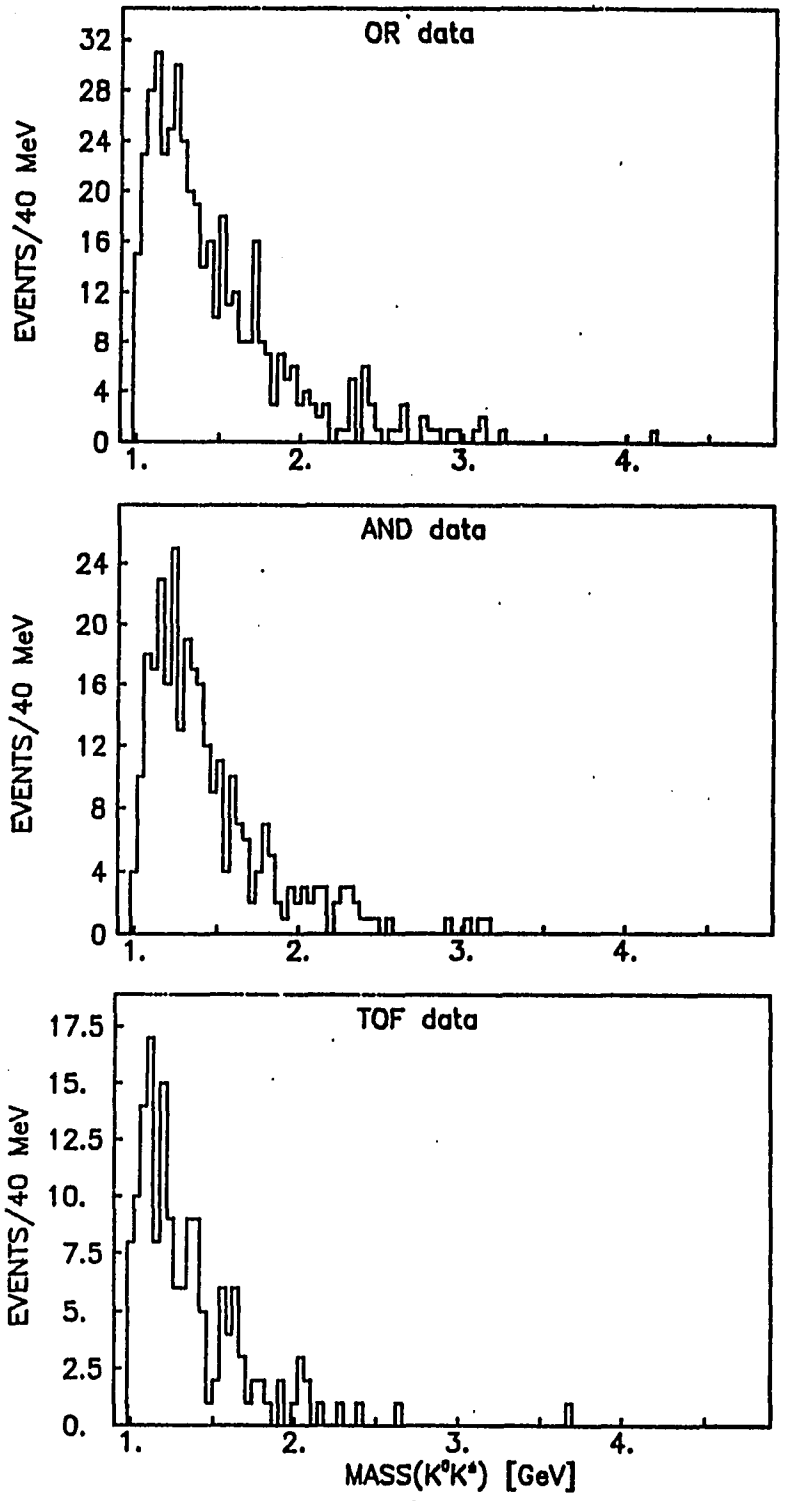

Figure 10.4. Mass distributions for $K^0K^{\pm}$ pairs for OR, AND, and TOF data

possible enhancements in the region of the $K^*(890)$ meson. There identification of a K^* signal in the $K^{\pm}\pi^{\mp}$ plots does not appear likely since the peaks of the distributions are at ~ 800 MeV which is too low to be identified with the K^*. The AND data show what appears to be a peak at 1350 MeV which could be identified with the $\kappa(1350)$ meson ($\Gamma \simeq 250$ MeV, $J^P=0^+$); however, the structure seen in this experiment is much too narrow to be the κ. No significant structure is seen in the $K^oK^{\pm}$ mass distributions.

The mass of the $K^oK\pi$ central system is plotted in Figure 10.5 for each data sample. The AND data show no enhancement, but the OR and TOF data both show a possible enhancement in the region of 1500 MeV. We next attempted to study this enhancement to see if it could be explained as something other than the result of the decay of a resonance.

One test performed on the data to investigate this possible signal was to look at the mass distribution for different probability-of-fit cuts. Figure 10.6 shows the mass of the $KK\pi$ central system for a probability-of-fit value of cut of greater than 0.01 for the TOF data. In this plot the peak at 1500 MeV has become much more significant. Figure 10.7 shows the mass distribution for a probability-of-fit cut of greater than 0.20. In this plot the peak has become less significant. Thus, this peak appears to be coming from events with lower probability-of-fit values and is therefore probably not a real resonance because the probability-of-fit distribution indicates that this region is dominated by events that do not satisfy energy and momentum conservation. There are no indications from the fit results which indicate that anything could be wrong with the fitting process. In fact, when one studies events that clearly fail to

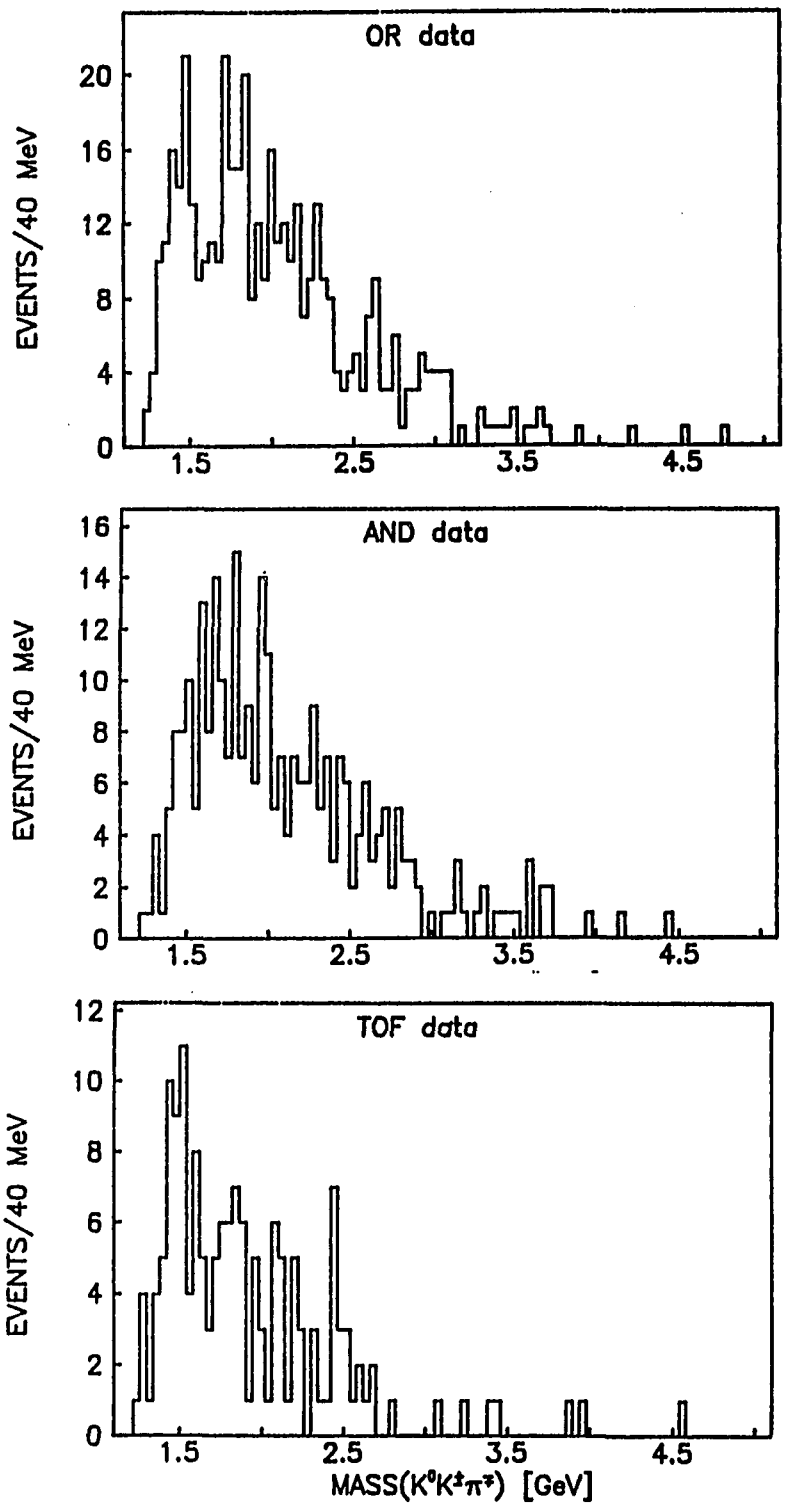

Figure 10.5. Mass distribution for KKπ system for OR, AND and TOF data

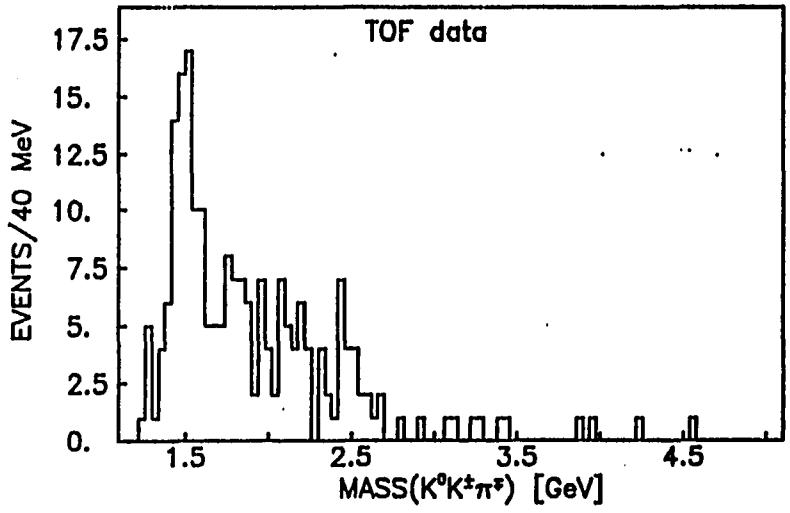

Figure 10.6. Mass distribution for the KKπ system for TOF data with prob. > 0.01

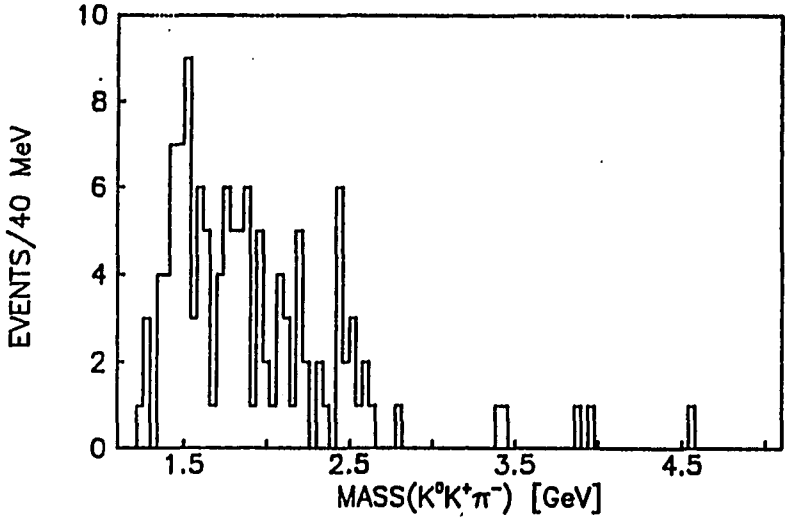

Figure 10.7. Mass distribution for the KKπ system for TOF data with prob. > 0.20

meet energy and momentum conservation, they exhibit a peak at 1500 MeV. This behavior is just like that seen in the four-prong OR and AND data for events that did not meet the requirements of energy and momentum conservation (see Figures 4.2 and 5.2).

Using the TOF data we were able to show that the observed peak does correspond to events containing a charged kaon. Thus, the most likely explanation of the peak at 1500 MeV is that it is from events which do not meet energy and momentum conservation rather than events where the identity of the tracks was incorrectly determined.

11. SUMMARY AND CONCLUSIONS

As far as the hope of locating and characterizing a gluonic bound state in a high energy proton-proton interaction, this experiment has not been successful. No new resonant states have been produced at a large enough rate to be detected in any of the analysis performed for this thesis. While this is disappointing (positive results are always more fun than negative results), it is important to be able to show that no unexplained resonances appear in the central system produced by Double Pomeron Exchange. This will provide a guide for future efforts in looking for glueballs, although there is no present accelerator in the world capable of repeating a similar experiment with the demise of the ISR.

We have succeeded in isolating a sample of DPE events which have been useful in exploring this interaction. The copious production of the f^o meson in DPE will need to be accounted for in any future model of the Pomeron-Pomeron interaction. These data contain a large sample of DPE events that decay into four central particles. All other DPE experiments reported before this experiment either have not reported such events or they have many fewer events than this experiment provides.

We have confirmed that the enhancement previously reported in the four prong OR and AND data is a spin two object and is almost certain to be the f^o meson. We have also shown that the six prong OR and AND data do not have a large $\rho^o\rho^o$ enhancement as in $\gamma\gamma$ interactions. This should have important consequences for theoretical comparisons of DPE interactions to $\gamma\gamma$ interactions.

The TOF data did succeed in increasing the fraction of kaons and protons in the central system produced by DPE, but unfortunately this was

at the cost of increasing the average event multiplicity. The approach taken in this thesis of only looking at exclusive reactions will have to be changed in order to attempt to take advantage of these events. Inclusive studies of the data may reveal properties of DPE not seen previously.

The upper limits on the cross section for the production of any new resonances will be set in subsequent publications of these data after the results of this thesis are used to help refine the Monte Carlo calculations of the acceptance of the SFM detector. To give one an estimate of the cross sections this experiment is sensitive to we can consider the published results on the analysis of the f^0. For the OR data sample the calculated cross section was $8 \pm 1 \pm 3$ μb, where the first quoted error represents the combined statistical error and the error in determining the background and the second quoted error represents an additional systematic uncertainty in the acceptance of the SFM [Breakstone et al. 1986]. From Figure 4.2(a) one can see that this resonance was easily detected, so the cross section that would be detectable in this experiment is on the order of a microbarn.

12. REFERENCES

M. Althoff et al., Z. Phys. C 16, 13 (1982).

B. Alper et al., Nucl. Phys. B100, 237 (1975).

U. Amaldi, M. Jacob, and G. Matthiae, Ann. Rev. Nucl. Sci. 26, 385 (1976).

J. J. Aubert and C. Broll, Nucl. Instr. Methods 120, 137 (1974).

H. J. Behrend et al., Z. Phys. C 21, 205 (1984).

W. Bell et al., Nucl. Instr. Methods 156, 111 (1978).

W. Bell et al., Nucl. Instr. Methods 124, 437 (1975).

B. Berg, A. Billoire, and C. Vohwinkel, Florida State University Preprint, FSU-SCRI-86-06, 1986.

J. P. Berge, F. T. Solmitz, and H. D. Taft, Rev. Sci. Instr. 32, 538 (1961).

A. Billoire, Florida State University Preprint, FSU-SCRI 86-02 (1986).

J. D. Bjorken, SLAC Summer Institute on Particle Physics, July (1979).

R. Bouclier et al., Nucl. Instr. Methods 115, 235 (1974).

R. Bouclier et al., Nucl. Instr. Methods 125, 19 (1975).

A. Brandt et al., Nucl. Instr. Methods 126, 519 (1975).

A. Breakstone et al., preprint CERN-EP/86-11 (1986).

A. Breakstone, "Results of Recent Glueball Tests", SFM Internal Note 8/12/82.

A. Breakstone, "Analysis of pp and $\bar{p}p$ Elastic Data", SFM Internal Note, 24/9/84.

P. Bryant, "Beam Crossing Angles at the SFM", SFM Internal Note, 13/8/73.

P. Bryant, IEEE Trans. on Nucl. Sci., NS-26, 3499 (1979).

P. Bryant, private communication, CERN, Geneva, Switzerland (1985).

C. E. Carlson and T. H. Hansson, Nucl. Phys. B199, 441 (1982).

M. S. Chanowitz, SLAC Summer Institute on Particle Physics, July (1981).

J. J. Coyne, P. M. Fishbane, and S. Meshkov, Phys. Lett. 91B, 259 (1980).

J. F. Donoghue and H. Gomm, Phys. Lett. 112B, 409 (1982).

D. Drijard, "Momentum Analysis by Using a Quintic Spline Model for the Track", SFM Internal Note (1976).

D. Drijard et al., Nucl. Phys. B143, 61 (1978).

C. Fischer et al., IEEE Trans. on Nucl. Sci. NS-26, 3155 (1979).

A. G. Frodesen, O. Skjeggestad, and H. Tofte, Probability and Statistics in Particle Physics (Universitetsforlaget, Bergen, 1979).

G. J. Gounaris and J. E. Paschalis, preprint Thessaloniki-TP 1/85, BI-TP 85/32 (1985).

M. Heiden, dissertation CERN EP Internal Report 82-05 (1982).

K. N. Henrichsen et al., in Proc. IXth Intern. Conf. on High Energy Accel., 390 (1974).

C. A. Heusch, Lecture delivered at the Yukon Advanced Study Institute, Aug. 11-26, (1984), SLAC-PUB-3556 (1985).

K. Huang, Quarks, Leptons, and Gauge Fields (World Scientific, Singapore, 1982).

K. Hubner, "ISR Performance for Pedestrians", CERN 77-15 (1977).

F. James, MINUIT, CERN Program Library (1983).

F. James, FOWL, CERN Program Library (1967).

R. J. Jaffe, Phys. Rev. D 15, 267 and 281 (1977).

E. Keil, "Intersecting Storage Rings", CERN 72-14, 21 July 1972.

J. W. Lamsa et al., Phys. Rev. D 26, 1769 (1982).

H. J. Lipkin, Phys. Lett. 106B, 114 (1981).

H. J. Lipkin, Phys. Lett. 109B, 326 (1982).

F. E. Low, Phys. Rev. D 12, 163 (1975).

S. Meshkov, in Experimental Meson Spectroscopy - 1983, edited by S. J. Lindenbaum, 113, 125 (1984).

R. Messerli, SFMGENER, CERN unpublished.

M. Metcalf, "Analysis of the SFM field", OM Development Note AP-10 9/1/74.

E. G. Michaelis, "Notes on Particle Accelerators", CERN Summer Student Programme Lectures, 1981.

S. Nussinov, Phys. Rev. Lett. 34, 1286 (1975).

P. Nyborg and O. Skjeggestad, in Kinematics and Multiparticle Systems, edited by M. Nicolic (Gordon and Breach, New York, 1968), p. 33.

P. Pascual and R. Tarrach, Phys. Lett. 113B, 495 (1982).

D. H. Perkins, Introduction to High Energy Physics (Addison-Wesley, Reading, Massachusetts, 1982).

J. Pumplin and E. Lehman, Z. Phys. C 9, 25 (1981).

K. Rauschnabel, CERN EP Internal Report 81-1 (1981).

D. G. Richards, Nucl. Phys. B258, 267 (1985).

D. Robson, Nucl. Phys. B130, 328 (1977).

J. L. Rosner, Phys. Rev. D 24 1347 (1981).

H. J. Schnitzer, Nucl. Phys. B207, 131 (1982).

H. Wind, Nucl. Instr. Methods 115, 431 (1974).

H. Wind, Nucl. Instr. Methods 153, 195 (1978).

C. G. Wohl et al., Rev. Mod. Phys. 56, No. 2, Part II, April 1984.

A. Yaouanc et al., Z. Phys. C 28, 309 (1985).